San Jose State University
SJSU ScholarWorks

1997

Thin film deposition of molybdenum microtips for field emission displays

Connie Y. F Wong
San Jose State University

Follow this and additional works at: https://scholarworks.sjsu.edu/etd_theses

INFORMATION TO USERS

This manuscript has been reproduced from the microfilm master. UMI films the text directly from the original or copy submitted. Thus, some thesis and dissertation copies are in typewriter face, while others may be from any type of computer printer.

The quality of this reproduction is dependent upon the quality of the copy submitted. Broken or indistinct print, colored or poor quality illustrations and photographs, print bleedthrough, substandard margins, and improper alignment can adversely affect reproduction.

In the unlikely event that the author did not send UMI a complete manuscript and there are missing pages, these will be noted. Also, if unauthorized copyright material had to be removed, a note will indicate the deletion.

Oversize materials (e.g., maps, drawings, charts) are reproduced by sectioning the original, beginning at the upper left-hand corner and continuing from left to right in equal sections with small overlaps. Each original is also photographed in one exposure and is included in reduced form at the back of the book.

Photographs included in the original manuscript have been reproduced xerographically in this copy. Higher quality 6" x 9" black and white photographic prints are available for any photographs or illustrations appearing in this copy for an additional charge. Contact UMI directly to order.

THIN FILM DEPOSITION OF MOLYBDENUM MICROTIPS FOR FIELD EMISSION DISPLAYS

A Thesis

Presented to

The Faculty of the Department of Materials Engineering

San Jose State University

In Partial Fulfillment

of the Requirements for the Degree

Master of Science

by

Connie Y.F. Wong

UMI Number: 1384731
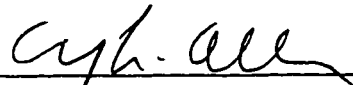
UMI
300 North Zeeb Road
Ann Arbor, MI 48103
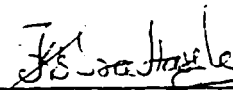
APPROVED FOR THE DEPARTMENT OF
MATERIALS ENGINEERING

Dr. Emily L. Allen

Dr. K. S. Sree Harsha

John O. O' Boyle, National Semiconductor

APPROVED FOR THE UNIVERSITY

ABSTRACT

THIN FILM DEPOSITION OF MOLYBDENUM MICROTIPS FOR FIELD EMISSION DISPLAYS

By Connie Y.F. Wong

Field emission display (FED) is a fast growing technology in the visual display market since it offers many advantages over other types of displays. FED consists of millions of field emitter tips. Deposition and formation of the field emitter tips is a critical step in making field emission displays. The focus of this thesis is the development of a thin film deposition process for Spindt-type molybdenum cones using electron beam evaporation. It was found that a dome-shaped evaporant source is required to obtain a uniform evaporation rate. Initial efforts to form molybdenum cones through a shadow mask were partially successful. It is believed that complete cones can be formed if enough molybdenum is deposited. Use of SIMBAD simulation reveals that the cone shape and cone height can be varied by varying the structure of the cavity, and the growth factors such as the sticking coefficient and the diffusion length.

ACKNOWLEDGMENT

Table of Contents

Chapter 1: Introduction

1. 1 Background

In the visual display market, flat panel displays (FPDs) are alternatives to the conventional cathode ray tubes (CRTs). FPDs have the advantages of being space saving, power saving, and lightweight, which provide portable, efficient, and high-performance displays to communicate with users. Due to the fast growing markets of laptop computers, video cameras, portable video games, digital organizers and big-screen TVs, the future trend in the market is to employ FPDs. The current dominant technology of FPDs is active matrix liquid crystal displays (AMLCDs). On the other hand, field emission displays (FEDs) are the fastest growing technology in the semiconductor industry for flat panel displays. FEDs combine two established techniques: electronic field emission microtips fabrication with advanced microelectronics technology, and low-voltage cathodoluminescent (front luminous) layer coatings in vacuum fluorescent displays. In comparison with AMLCDs, FEDs offer reduced manufacturing complexity and cost, increased brightness, fast response time, improved viewing angle, and reduced power consumption.[1] Moreover, unlike AMLCDs, FEDs produce their own light using colored-phosphors that are inherently faster and more persistent than liquid crystal. Therefore, they do not require complicated, power consuming backlights and filters, and almost all the light generated by an FED is visible to the user. Further power savings result because no power is consumed by pixels in the off state. Besides, FEDs may help US firms to enter the FPD market which is now dominated by Japanese companies.[1]

1. 2 Behind field emission displays

Field emission displays (FEDs) rely on Fowler-Nordheim tunneling[1] to emit electrons. Normally, electrons cannot escape from a metal unless the metal is heated due to the thermionic effect. However, when an electric field is applied to a metal surface, the energy barrier for electrons between the metal and vacuum decreases. At sufficiently high applied fields, electrons tunnel through the barrier and emit from the metal surface, even at 0 °K.

FED is constructed of a baseplate mounted with field emission cathode arrays, a faceplate patterned with three colored phosphors, and matrix address lines. In an FED, each pixel consists of an array of field emission cathodes; each pixel has its own electron source coming from the field emission cathodes. With a negative voltage applied to the emitter tips of the cones with the gate film, field emitted electrons impinge on phosphors on a transparent faceplate and produce the image. Each color element of the display is addressed by a group of a few hundred emitter tips operating in parallel. The large number of emitter tips in the array enables tip-to-tip current fluctuations to be smoothed out. This allows for some redundancy in cases where one or a few emitters are not operating, and leads to a uniform display.[1] The basic design of a pixel and a cross-sectional view of field emission cathodes are shown in Figure 1.1 and Figure 1.2 respectively.

1. 3 Research on field emission tips

Besides field emission displays, field emission cathode technology can be
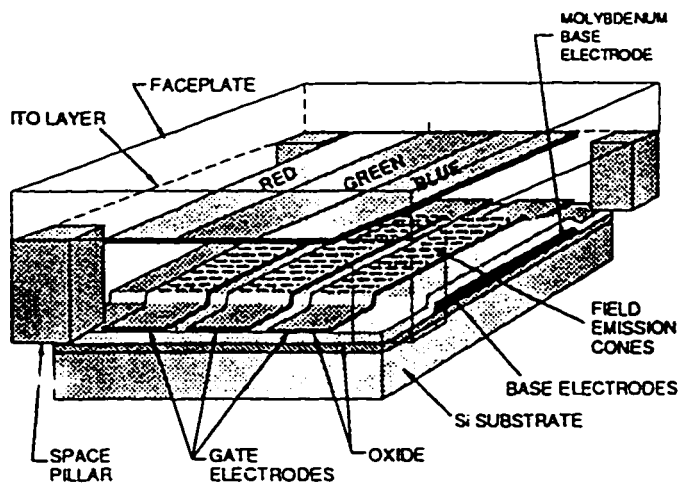
Figure 1.1: Typical pixel cutaway.[2]
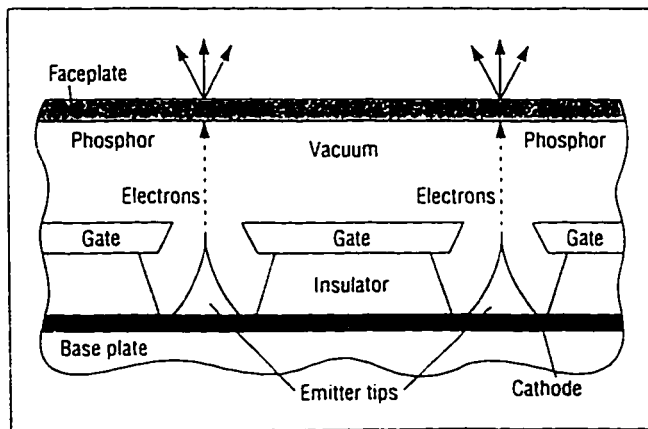
Figure 1.2: Cross-sectional view of field emission cathodes.[1]

applied to a variety of applications, such as microwave amplifiers, and electron optics

devices; different applications have different requirements for the field emitter.

Much research is being done on fabrication of the field emission cathodes.[2] The

basic structures are very similar to each other: a thin-film sandwich comprised of a

3

conductor/insulator/conductor structure. However, the field emitter tips can be made of different materials and/or different geometries, and the fabrication process is different, depending on the geometry and the material used. There are many different geometrical shapes of field emitters such as tower structure, cocktail glass structure, sharpened silicon cone, Spindt-type cone and so on. The SEM micrographs of these various geometrical shapes are shown in Figure 1.3. However, there has been no research reported so far comparing the performance of the tips with different geometries.

There are three major approaches for the field emitters: diamond emitters, silicon microtip emitters, and metal microtip emitters. They all have different fabrication technologies with different emitter materials. Since this thesis focuses on the fabrication of the field emitter tip used in field emission displays, the fabrication process of different types of field emitter tips are of particular interest.

1.3.1 Diamond-like carbon field emitter

Diamond field emitter is the newest FED technology.[1] No published work was found giving the details of the field emitter fabrication process. Generally speaking, laser plasma deposition is used to produce the noncrystalline diamond-like material. A laser beam is directed within a vacuum chamber to impinge upon a pure graphite foil target, and a plume of carbon vapor is ejected and deposited upon the surface of the substrate.[6] Finally, an amorphous diamond-like material is formed on the substrate. The macro-geometry of the point is not a cone, but a four-faceted pyramid, and the micro-geometry is conditioned by micro-irregularities of the component in the form of octahedra, that

4
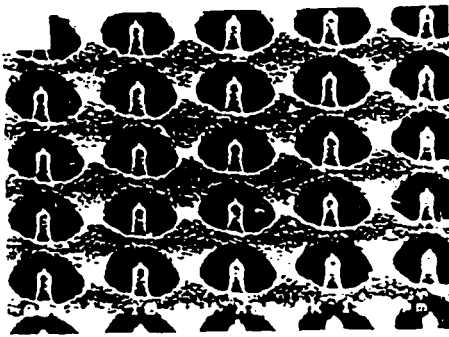
Tower structure

Cocktail glass structure
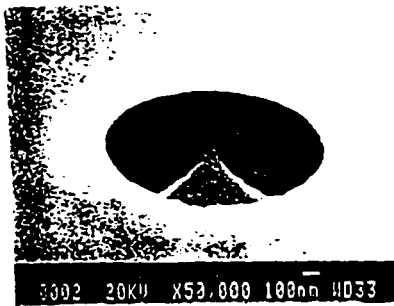
Sharpened silicon cone
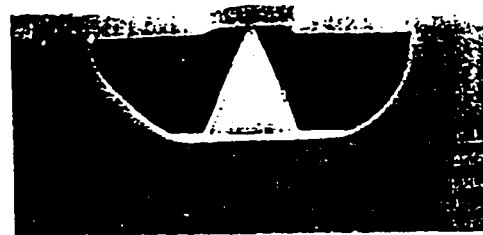
Spindt-type metal cone

Figure 1.3: SEM micrographs of different emitter tip geometry.[3,4,5]

encrusts the pyramid facets and ribs.[7]

1. 3. 2 Self-aligned silicon field emitter

The fabrication of a self-aligned gated silicon emitter tip is shown in Figure 1.4.

A layer of silicon dioxide is thermally grown on a (100) oriented n-type silicon substrate.

SiO_2 discs are patterned on the substrate by masking and etching. The SiO_2 disc pattern

is then used as the mask for reactive ion etching (RIE) of the silicon. The RIE process is

optimized to produce the controlled amount of undercut which defines the diameter of the

silicon tips. The silicon tips are sharpened by a second thermal oxidation. A SiO_2

insulator layer and gate metal layer are then deposited. Finally, the silicon tips are

uncovered by etching in buffered hydrofluoric acid.[4]
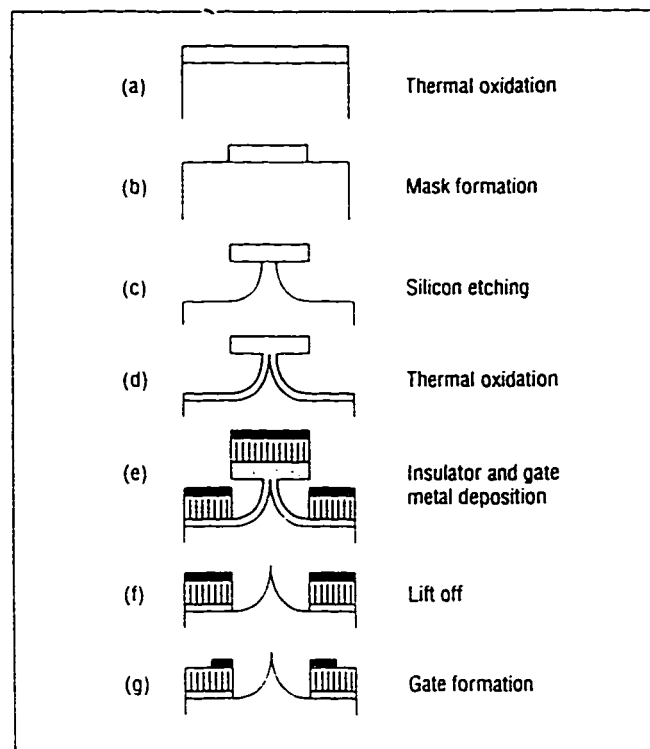
Figure 1.4: The fabrication process of a self-aligned gated silicon emitter.[1]

1. 3. 3 Spindt-type microtip emitter

Spindt-type microtip emitters were the first field emitter tip technology used in

field emission cathode arrays. They were developed by C.A. Spindt and his co-workers at

Stanford Research Institute (SRI) in the early 70's.[10] The first emission cathodes were

comprised of cone-shaped molybdenum (Mo) microtip emitters, and they are still a core

FED technology nowadays.

The fabrication process of the Spindt-type Mo field emission cathode is depicted in Figure 1.5. The silicon substrate is thermally oxidized to grow a thick silicon dioxide (SiO_2) insulating layer. A metallic gate layer is deposited on top of the SiO_2 layer, then an array of holes is patterned. The metal and SiO_2 layers are then etched to form cylindrical shaped holes. Then, the substrate is mounted in an electron beam evaporation system and is rotated about an axis perpendicular to its surface. After a sacrificial layer (parting layer) is shadow deposited at grazing incidence, molybdenum is then deposited through the holes by electron beam evaporation perpendicular to the surface. The size of the holes continues to decrease because of condensation of molybdenum on its periphery. A cone then grows inside the cavity until the hole closes above it. Finally, the sacrificial layer is lifted off, leaving an emitter cone.[8]

No publications were found explaining the phenomenon of deposition of Mo on the periphery of holes. The mechanism may be due to the fact that, at the early stage of deposition, Mo atoms condense on the periphery because the temperature there is lower than the temperature of Mo atoms; at the same time, since the substrate is rotating, the Mo atoms are evenly condensed at all sides of the holes. Then, a layer of Mo atoms is formed at the periphery of the holes. Afterwards, another layer of Mo atoms adheres to the first layer, and the adhesion continues so that layers of Mo atoms are uniformly deposited around the periphery. Thus, the holes are gradually closed, thereby shaping the emitter material being deposited inside the cavity of the substrate. The mechanism of the phenomenon is shown in Figure 1.6.

Oxidation of Si substrate and evaporation of gate layer	← Metal gate ← Oxidized layer (SiO_2: about $1.0\mu m$) ← Si substrate: N (100)
Patterning of photoresist layer	← Photoresist
Hole pattern etched in gate film and oxidized layer	
Deposition of parting layer at grazing incidence	← Axis of rotation ← Parting layer
Formation of emitter cone by closure layer evaporation	← Closure layer (Mo: $1.8\mu m$)
Etching off parting layer	← Gate ← Emitter

Figure 1.5: The fabrication process of the Spindt-type field emission cathode.[9]
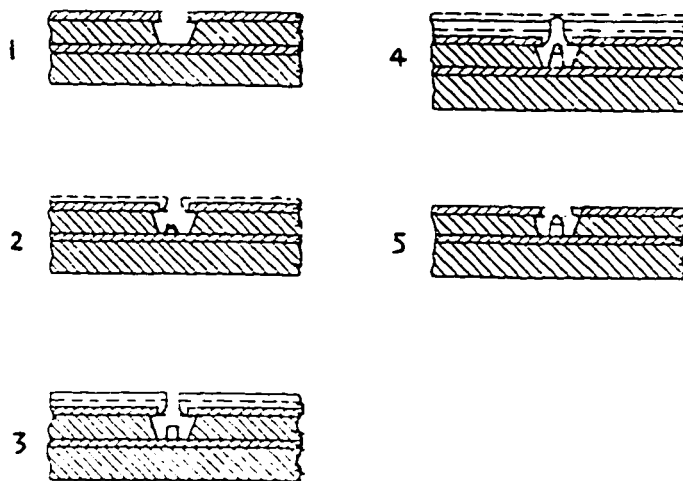
Figure 1.6: The phenomenon of deposition of Mo at the periphery of the holes.[10]

8

1.3.3.1 Factors determining the cone geometry

It is important to understand what factors determine the cone geometry such as the cone height and cone shape, as well as the amount of protrusion. Conceptually, the cone geometry should be directly related to the structure of the hole cavity. This may be explained by first considering a cone shape is directly related to the ratio of vertical growth to lateral growth. If we divide a cone into continuous segments of layers, it is obvious that the cone height and cone shape depend on the successive vertical and lateral growth rate. The vertical growth is mainly determined by the deposition rate. Of course, longer deposition time gives rise to a taller cone. In parallel, there is lateral growth at the periphery of the hole and the size of the hole continues to decrease. When the cone grows vertically, the lateral dimension gets narrower because the hole size continues to decrease. Therefore, all those factors that influence the lateral and vertical growth determine the height and the shape of a cone. The cone formation is terminated when the hole is completely closed. However, the time taken for the deposition of cone depends on the time taken to close the hole, i.e., there is no more lateral growth when the hole is closed. Since the time taken to close the hole is determined by the hole diameter, the cone height is expected to be a function of the hole diameter. The larger the hole diameter, the longer it takes to close the hole, and the higher the resulting cone. Moreover, it is believed that the angle and the shape of the retrograde undercut influence the lateral growth rate. In particular, it is likely that these factors have a big impact on what position and how many atoms growing on the periphery of the hole in the beginning of the deposition, which influences its successive lateral growth. Therefore, the time taken to close the hole varies

due to the shape and the angle of undercut of the parting layers. It is also believed that the retrograde undercut prevents molybdenum from depositing along the sidewall of the cavity and shorting the gate voltage. Photoresist is a good option for obtaining different shapes of the parting layer, since it is a readily available material in the semiconductor industry, and it is possible to make different shapes using the current semiconductor photolithographic technology. In summary, the hole diameter, along with the shape and the angle of undercut, determines the cone height and cone shape.

On the other hand, the amount of protrusion should be dependent on the height of the cavity (i.e., thickness of the oxide plus the gate metal). A thinner layer will give a greater amount of protrusion.

1. 3. 4 Comparison between the three different microtips

The basic requirements of field emitters include low operating voltage, high emission current, emission stability, and long life expectancy. The other factors are dependent on the emitter materials. A good emitter material should have a low work function, which gives rise to high emission current; moreover, it should be stable over time rather than being subject to thermal or chemical degradation.[1]

The effective work function of a diamond-like field emitter can be as low as 0.2-0.3 eV,[1] compared to about 4.5 eV for silicon and 4.37 eV for molybdenum; thus a diamond-like field emitter exhibits greatly enhanced emission current. Besides, diamond features chemical inertness and extremely high mechanical strength; ion sputtering effects from the surrounding gas are reduced, and this increases life time and the ability to

10

operate in a relatively high pressure environment. Therefore, substrate cleaning, and

device evacuation and sealing processes are greatly simplified; the diamond emitter

operates satisfactorily at a vacuum of only 10^{-4} torr without the sputtering effect, while

other field emitters require 10^{-5} to 10^{-7} torr to prevent sputtering. However, diamond

deposition technology is still in its infancy, and a uniform emission area over the entire

display area has not been demonstrated.

Silicon microtips have the advantage of easy fabrication and having their tip

radii easily sharpened with existing semiconductor technology. However, the process has

a significant limitation on the aspect ratio, defined as the ratio of the thickness of the

insulator layer to the gate aperture, which limits the reduction of operating voltage.

Besides, silicon has a lower melting point (1412 °C), poor electrical and thermal

conductivity as compared to molybdenum; the maximum field emission current is limited

by the thermal instability and overheating.

On the contrary, molybdenum has a high melting point (2622 °C), good thermal

conductivity, and low specific heat; the current limit can be about 15% higher than even

heavily-doped silicon due to its good thermal stability.[8] In addition, it has high

resistance to field evaporation and excellent mechanical strength allowing high current

and temperatures without tip failure, which increases its service life. Mo has a very low

sputter yield which is important for high brightness displays. Low sputter yields will

allow operation at high screen potentials where back-bombardment of the tip by ions

(produced by electron-impact ionization of residual gas or electron-stimulated desorption

from the anode) could degrade device performance.[11] Mo has a relatively low work

function of 4.37 eV, and will not form a native oxide at low temperatures. Mo has a very low extraction voltage which is an important parameter for flat panel displays, since low voltage makes it compatible with the CMOS drivers' circuitry used in flat panel displays. Low voltage also helps to increase the burnout resistance. The low voltage operation can be further improved by the field forming process, which will be discussed in more detail in Section 1.4. Moreover, Mo is compatible with standard semiconductor process technology. Although Mo emitter tips have the disadvantage of emission instability, this problem can be solved. Details of the solution will be described in Section 1.4.

Therefore, among these three most promising approaches, Spindt-type Mo microtips are still the most compatible FED technology, since it has been developed for more than 20 years, and the technology is well established. The development progress of the Mo field emitter is discussed in the following section.

1.4 Development of Spindt-type cathode array

According to the papers published by Spindt in the past 20 years, the fabrication technology development continued to improve the performance of the field emission cathode arrays.[8,12,13] The progress of development is summarized in Table 1.1.

The tip packing density is an important consideration since it is directly related to the current density and transconductance (rate of change of emission current with respect to gate voltage), which are the important cathode parameters for the performance of many applications.

Table 1.1: The progress of development of Spindt-type cathode arrays
in the 70's, 80's and 90's.[after 8, 12, 13]

Year	Tip packing density (Tips per cm^2)	Current density (A per cm^2)	Operating voltage (V)
70's	6×10^5	10	100-300
80's	1.2×10^6	50	50-150
90's	1.5×10^7	1000	15-50

According to the paper written by Spindt in 1991,[13] packing density can be improved by reactive ion etching (RIE) technology. In the past, the SiO_2 insulating layer was isotropically etched with wet chemistry to form a cavity, which undercut the gate film significantly. The undercutting limited the packing density to the order of 10^6 tips/cm^2.

When RIE is used, it is capable of etching SiO_2 anisotropically with essentially no undercut of the gate film. Packing density can be further increased by reducing the hole diameter and placing the holes closer together; this can be achieved by using the advanced multiple electron beam exposure system (MEBES) to print the hole patterns.

Another important parameter is the low voltage operation of the cathode arrays; it not only saves energy but also greatly reduces the susceptibility to damage from ion sputtering, and thus increases lifetime and resistance to relatively high pressure environments. Such emission characteristic can be improved by the so-called "field forming process." It is achieved by heating the cathode while the tips are under high electric field stress. The tip is reformed, due to the field forming process, into a

configuration that increases the electric field locally on the tip surface for a given applied voltage.[13] Therefore, the emission current will increase due to the field forming process. or in other words, the voltage required to produce the same emission current will be reduced. According to Spindt's experimental result, the voltage required to produce 20 mA has been reduced from 100 V to 35 V.[13]

Another method to improve the emission performance is to coat the Mo with a very thin layer of electropositive (relative to the substrate) material, such that the work function is reduced. Spindt *et al.* successfully coated a thin layer of cesium onto the molybdenum emitters, and the performance was enhanced significantly. Emission current density as high as $1600A/cm^2$ has been obtained.[14]

In addition to the requirements of low voltage and high current operation, emission stability of the cathode arrays is an important factor to be considered. According to the experimental result by Goodhue *et al.*,[15] proper hydrogen passivation of the Mo field emitter can reduce current instability and increase current density. The hydrogenation process consists of bombarding the surface of the Mo cone with hydrogen ions generated in a hydrogen plasma. The process desorbs the surface oxygen and carbon, which will diffuse to the grain boundaries and cause the grains to shift and deform at elevated temperature. The hydrogenation process, in effect, stabilizes the structure at a variety of current levels since all dangling bonds in the grain boundaries near the tip have been passivated.

Spindt also investigated the effect of geometry on the emission.[8] He found

that the tip emission was strongly dependent on the diameter (D) of the hole in the gate

electrode, and on the position of the tip with respect to the lower plane of the gate

electrode. The experimental results indicated that protruding cones, with D as small as

possible, should be used. The tip protrusion definition of a field emission cathode is

shown in Figure 1.7. This phenomenon was explained by Robert et al.[16] By using the

boundary element method, they found that a protruding cone increases the tip field

strength and thus enhances emission current.
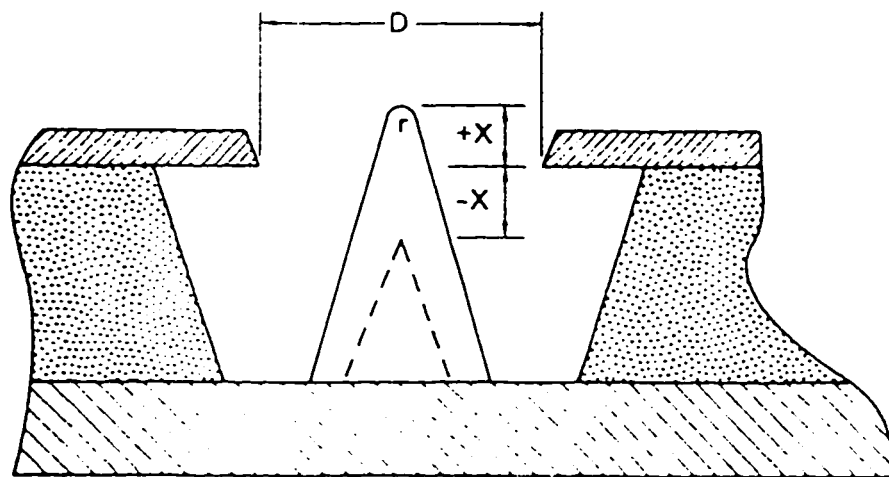
Figure 1.7: A field emission cathode with tip protrusion definition.[8]

As mentioned earlier, the field emission cathode developed by Spindt and his co-

workers used a molybdenum cone-shaped microtip emitter. There was little discussion of

why molybdenum is a good material for making the cone, why a cone-shaped field

emitter is good for field emission, and also why electron beam evaporation is chosen for

the formation of emitter cone among different thin film deposition techniques. This

brings up the following questions:

15

i. Why is molybdenum a good material for making the field emitter? Are there any other alternatives that perform even better?

ii. Is a cone shaped microtip an ideal shape for a field emitter?

iii. Why is electron beam evaporation the best deposition method for the emitter cone?

1.5 Material selection for a Spindt-type field emitter

To find out what is a good material for making the field emitter, the criteria for good emitter materials should be determined first. The criteria include low work function, high mechanical strength, good thermal stability, high sputtering resistance, long service life, easy fabrication, low fabrication cost, high degree of reproducibility, high chemical inertness, high emission current, low voltage operation, and good emission stability. Mo is a good choice because it meets all of the criteria of being a good emitter material. The properties of molybdenum were mentioned in Section 1.3.4. Moreover, there were many studies done to improve the emission performance of Mo emitter, which were discussed in the previous section.

On the other hand, are there any other metals that exhibit even better characteristics than molybdenum? There are some other metals that have even lower work functions,[17] which for example can be as low as 2 eV. Unfortunately, those metals with lower work functions also have extremely low melting points and mechanical strength, which do not satisfy the requirements of being good emitter materials. The only metal with properties comparable to molybdenum is tungsten (W), which is a widely used material in the conventional field emission systems such as field emission SEMs.

However, it is not a commonly used field emitter material in the micro-fabrication technology such as field emission displays. Because of its extremely high melting point of 3410 °C, the deposition rate will be extremely low; in addition, since the Spindt-type field emitters use electron beam evaporation as the deposition method, high deposition temperature is required to deposit tungsten which may cause radiation damage to the substrate. Also, the high heat of vaporization of W makes it difficult to control the evaporation rate. A variation of deposition rate can adversely affect the properties of a thin film, such as the refractive index and the microstructure. These are the reasons why W is not used in field emitter tips.

In summary, Mo has the properties that enable it to meet all the requirements of being a good emitter material, except that it is quite easily oxidized at high temperatures. This is not a critical factor, since field emitters are operated in a vacuum environment; moreover, the oxidizing problem can be solved by the hydrogenation process, which was discussed in Section 1.4.

Further questions arise as to why elemental metals are chosen for study but not alloys. It is because two or more independently controlled evaporation sources are required to deposit an alloy. The individual component evaporation rate should be determined independently under experimental conditions, and the conditions should be adjusted in order to get the desired composition. In other words, the deposition process is not easily maintained and controlled. Although using the sputtering method to deposit alloys may solve the problem, some other problems are created. The disadvantages of using the sputtering method will be discussed in section 1.7.

1.6 What is the ideal emitter shape?

Using computer modeling, Utsumi[18] compared field emission characteristics of

various emitters with different geometrical shapes and found that the ideal shape of the

field emitter should be based on the concept of maximizing the current while minimizing

the voltage and the dimension of the field emitter. He concluded that the rounded

whisker shape, as shown in Figure 1.8, is the closest to the ideal field emitter, since it has

the largest current at the lowest voltage. On the other hand, the rounded whisker-type

emitter has the lowest ultimate limit of the field emission current because of its poor

thermal stability. Therefore, the ideal field emitter shape, which fulfills both thermal

stability and the requirement of maximizing the current will be an Eiffel Tower shape

which is a combination of a rounded whisker emitter tip and a wide emitter base. The

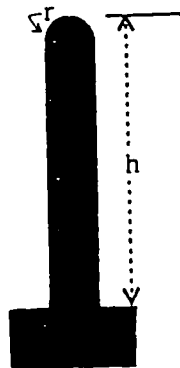Eiffel Tower shape is shown in Figure 1.9.
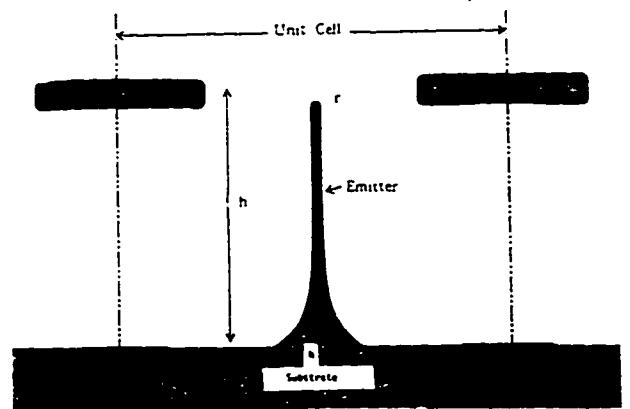

Figure 1.8: A field emitter with
rounded whisker shape.[17]

Figure 1.9: An ideal field emitter
with Eiffel Tower shape.[17]

For the physical dimensions of height (h) and the tip radius (r) of an emitter.

Utsumi reported that the ratio h/r was 50 for an ideal emitter.[18] Moreover, he also mentioned that the smaller the dimensions of the field emitter, the better the thermal stability. On the other hand, in reality, some other factors must be considered for the height (h), like the distance between the tip and the gate, and the aspect ratio of the insulator layer thickness and the gate aperture. Unfortunately, there is still no breakthrough to determine the best material or geometry to be used for an ideal emitter.

1.7 Electron beam evaporation for field emitter formation

To fabricate an emitter cone, evaporant atoms must be deposited at normal incidence to the substrate, such that molybdenum can be deposited gradually and uniformly at the periphery of the hole. As the size of the hole continues to decrease, a cone can be formed when the hole is completely closed. A high directionality or a long mean free path of evaporant atoms is required for the cone formation. Electron beam evaporation meets this requirement since the evaporation operates in a high vacuum. If a sputtering method is chosen, the deposition will be more isotropic due to its short mean free path. The cavity of the hole may be filled up completely instead of forming a cone-shaped emitter. In this case, unless a collimated grating is used to guide the directionality of the evaporant atoms, an emitter cone cannot be obtained. A grating increases the fabrication cost. Sputtering has other disadvantages as well, such as gas entrapment which causes stress problems, and sputtering damage to the target. On the other hand, electron beam evaporation does not have such a problem because the evaporation is carried out at relatively low pressures, it is a low contamination process

and gas entrapment in the film is negligible.

1.8 Overview

In summary, Utsumi pointed out that the ideal emitter shape is an Eiffel Tower which was shown in Figure 1.9. However, it is not easy to fabricate this shape in practice. It only serves as a guideline. Moreover, the principle of optimization for the field emitter performance must also come from other factors, such as service life, ion sputtering resistance, operating pressure, transconductance, and capacitance, depending on different applications of the device.

There are a number of studies being done on the field emitter shape; they all have unique advantages and disadvantages. The main point is how do we utilize the current technology, with the aid of a proper design and treatment of the emitters, so that the best performance can be achieved for a specific use of the devices. There are some trade-offs that need to be considered before a decision can be made. For the time being, among the three most promising approaches, Spindt-type molybdenum cone-shaped field emitter is the most mature FED technology.

1.9 Research hypothesis

This work focused on the development of thin film deposition of Spindt-type molybdenum field emitter cones using electron beam evaporation. The thesis consisted of three phases. The first phase was to perform characterization of molybdenum thin film electron beam deposition. The aim was to develop a controllable process, which required

determining the relationship between deposition rate and the power input. The second phase was to form a molybdenum cone using electron beam evaporation. The characteristics of the molybdenum thin film such as its microstructure and its internal stress were studied. Finally, in the third phase, a simulation program called SIMBAD[19] was utilized to predict how the growth parameters affect the cone shape and cone height. These factors included shadowing effects (i.e., topography such as the structure of the cavity), sticking coefficient, and surface diffusion factor.

1.9.1 Phase one - Characterization of Mo thin film electron beam deposition

The aim of phase one was to become familiar with the use of the electron beam system, and to characterize Mo electron beam evaporation. Deposition parameters and results such as operating power, operating pressure, deposition thickness and time, and the change of the shape of molybdenum source were monitored. The thermodynamic and kinetic foundations of thin film deposition are described in Chapter 2. Apparatus and materials that were used included an Airco Temescal STIH-270-2M electron beam evaporation system, a custom-designed wafer holder, a mechanical pump and a Cyro-Torr 8 cryopump, a Dektak-II profilometer, and bare silicon wafers as substrates. Configuration and operation of the electron beam system are described in Chapter 3. Experimental results are discussed in Chapter 4.

1.9.2 Phase two - Molybdenum cone formation using electron beam evaporation

The aim was to form cones by depositing molybdenum through the holes of a

shadow mask at normal incidence, using electron beam bombardment on a small

molybdenum evaporant source. The shadow mask used was a structure of SiO_2 on top of

silicon (i.e. SiO_2/Si substrate) with many cylindrical holes etched through down to the

silicon substrate. Molybdenum was evaporated through the shadow mask. Afterwards,

the shadow mask was cross-sectioned and polished. SEM was utilized to investigate if

cones were successfully grown inside the cavity of the holes. Experimental results are

presented in Chapter 5.

1.9.3 Phase three - Simulation of thin film deposition

A simulation program called SIMBAD was utilized for the thin film deposition

simulation. The input parameters are the primary factors that determine the film growth.

They include shadowing effect (which is determined by the topography of the substrate),

sticking coefficient, and surface diffusion. A description of how the key growth

parameters affect the thin film growth is discussed in Chapter 6. Different hole

diameters, different shapes and angles of undercut were used as input for the topography

files. A brief description of the SIMBAD program is discussed in Chapter 6. The

simulation results are discussed in Chapter 7.

Chapter 2: Thermodynamic and Kinetic Foundations of Thin Film Deposition by Evaporation

To characterize thin film deposition by evaporation, such as to find out the relationship between the power input, the equilibrium pressure of evaporant vapors and the source temperature, it is important to know the thermodynamic and kinetic aspects of different stages of thin film formation.

2.1 Introduction

In evaporation, atoms are removed from the source by thermal means, whereas in sputtering they are dislodged from solid target surfaces through impact of gaseous ions.

The deposition of thin films by evaporation consists of three distinguishable steps:[20]

i.   Transition of a condensed phase, which may be solid or liquid, into a gaseous state. This step involves the theory of thermodynamics of phase transitions, from which the equilibrium vapor pressure of materials will be derived.

ii.   Vapor traversing the space between the evaporation source and the substrate at reduced gas pressure. This step involves the kinetic theory of gases which provides models of the atomistic processes and the exchange of single molecules between a condensed phase and its vapor. From this basis, the deposition of evaporant atoms on surfaces surrounding a vapor source can be derived.

iii. Condensation of the vapor upon arrival on the substrates. This step involves the

kinetic aspects of condensation processes, which are related to nucleation and growth phenomena.

A more detailed description about each of the three film formation steps is discussed in the following sections.

2.2 Thermodynamics of phase transitions

Thermodynamic equilibrium is a situation where two states, for instance, a condensed phase and its vapor, exist at the same temperature and in contact with each other without undergoing net changes. That means the amounts of evaporating and condensing material are equal at all times as long as equilibrium is maintained. Under such conditions, solids and liquids have characteristic vapor pressures which are unique functions of temperature.

Although evaporation is not an equilibrium process, it involves transfer of material from one state to another. Atomic theory and extensive experiments [20] have shown that evaporation rates cannot exceed an upper limit which is proportional to the equilibrium vapor pressure. Therefore, the saturation pressure of a vapor over its condensed phase at a particular temperature is an important quantity to determine the practical transfer rate. A convenient starting point for expressing the connection between temperatures and vapor pressures is the Clausius-Clapeyron equation, which can be applied to both solid-vapor and liquid-vapor equilibria. The Clausius-Clapeyron equation was found to be useful in correlation, interpolation, and extrapolation of vapor pressure data; and also in estimating latent heats from vapor pressure data. The Clausius-

Clapeyron equation can be written as

$$\left(\frac{dP^*}{dT}\right)_{eq} = \frac{H_g - H_c}{T(V_g - V_c)} \qquad (2.1)$$

where dP^* is the change in equilibrium pressure resulting from the small temperature

change dT, H_c and V_c are the enthalpy and the molar volume of the condensed phase, and

H_g and V_g are the enthalpy and the molar volume of the gaseous phase.

In order to solve Equation 2.1, two approximations are made. The molar volume of

the condensed phase is neglected since it is very small compared with the molar volume

of the vapor. Furthermore, the vapor is assumed to obey the ideal gas law. Therefore,

$$V_g - V_c \cong V_g = \frac{RT}{P} \qquad (2.2)$$

In addition, the difference of the enthalpies in Equation 2.1 is the molar heat of

evaporation

$$H_g - H_c = \Delta_e H \qquad (2.3)$$

With these modifications, Equation 2.1 transforms into

$$\frac{dP^*}{P^*} = \frac{\Delta_e H}{RT^2} dT \qquad (2.4)$$

or $\qquad\qquad dlnP^* = \frac{\Delta_e H}{RT^2} dT \qquad (2.5)$

25

For small temperature intervals, $\Delta_e H$ can be assumed to be independent of temperature. i.e. $\Delta_e H$ is a constant. The integration of Equation 2.5 gives

$$\ln P^* \cong - \frac{\Delta eH}{RT} + \text{constant (I)} \qquad (2.6)$$

Through substitution of the molar heat of evaporation (ΔeH), the boiling point for T, and 1 atm for P, the constant (I) can be calculated. An expression to relate the vapor pressure and the temperature is obtained. Alternatively, if vapor pressure data is available, heat of evaporation (ΔeH) can be estimated by plotting the logarithm of P vs the reciprocal of the absolute temperature according to Equation 2.6.

However, Equation 2.6 is only valid for small temperature intervals. A more accurate vapor pressure function is obtained by considering the temperature dependence of the molar heat of evaporation. It is determined by changes which the molar specific heats in both condensed and gaseous states undergo with temperature:

$$\frac{d(\Delta_e H)}{dT} = C_{p,g} - C_{p,c} = \Delta C_p \qquad (2.7)$$

where the specific heats may be expressed in the general form $C_p = a + bT + cT^{-2}$, and the coefficients a, b, and c are numerical factors specific for a particular substance. Insertion of the Cp into Equation 2.7 and subsequent integration gives

$$\Delta_e H = \Delta_e H^* + \Delta aT + (\Delta b/2)\, T^2 - \Delta cT^{-1} \qquad (2.8)$$

where $\Delta_e H^*$ is an integration constant which must be determined experimentally. Further

26

substitution of Equation 2.8 into Equation 2.5 and integration of the latter gives

$$\ln P^* = -\frac{\Delta_e H^*}{RT} + \frac{\Delta a}{R}\ln T + \frac{\Delta b}{2R}T + \frac{\Delta c}{2R}T^{-2} + I \qquad (2.9)$$

where I is another constant of integration which is specific for a given material, and the coefficients Δa, Δb, Δc for the specific heat change (ΔC_p) are numerical factors for a particular substance.

Unfortunately, the equilibrium vapor pressure is still not easy to solve from Equation 2.9 because the constants $\Delta_e H$ and I cannot be derived from first principles. Moreover, the compilations of thermochemical data rarely list these constants. Therefore, an expression equivalent to Equation 2.9 but containing only standard thermochemical data which are commonly listed thermodynamic functions, is desired to calculate vapor pressures for different temperatures. Details of how to derive the expression will not be discussed here.[20] The expression of the form with the standard enthalpy and entropy terms is

$$\log P^* \text{ (torr)} = AT^{-1} + B + C\log T + DT + ET^{-2} \qquad (2.10)$$

$$\text{where } A = -\frac{\Delta_e H^\circ(298) - 298(\Delta a + 149\,\Delta b) + 3.35 \times 10^{-3}\,\Delta c}{4.575}$$

$$B = \frac{\Delta_e S^\circ(298) - 6.70\Delta a - 298\,\Delta b + 5.6 \times 10^{-6}\Delta c}{4.575} + 2.8808$$

27

$$C = \frac{\Delta a}{1.987} \qquad D = \frac{0.5 \ \Delta b}{4.575} \qquad E = \frac{0.5 \ \Delta c}{4.575}$$

Therefore, corresponding equilibrium pressure can be calculated for different temperatures because the constants A, B and C can be found by the substitution of the themochemical data.

2.3 Kinetic theory of gases

The atomistic model of the evaporation process is based on the kinetic theory of gases.[21] It is assumed that a large number of atoms or molecules of the gas are in a continuous state of random motion, which is dependent on the temperature of the gas. During their motion the gas particles collide with each other as well as with the walls of the confining vessel. Using ideal gas approximation, there is no attractive or repulsive forces between molecules except at the moment of collision. Instead, they may be considered to behave like independent elastic spheres separated from each other by distances that are large compared with their size. The number of molecule-molecule or molecule-wall collision occurring depends on the concentration or pressure of the gas. In other words, the pressure exerted by a gas on its confining vessel results from the momentum transfer of gas molecules when they strike the walls.

It was found that the gas pressure (P) which the impinging molecules exert upon the wall, is related to the mean-square velocity of the molecules ($\overline{c^2}$) and thus, to their kinetic energy or temperature.[20] The relationship between pressure P, mean-square

28

velocity $\overline{c^2}$ and temperature T is expressed as follows:

$$P = \frac{1}{3}\frac{N}{V}m\,\overline{c^2}$$

(2.11)

where

$$\overline{c^2} = \frac{\Sigma c^2}{N} = \overline{u^2} + \overline{v^2} + \overline{w^2},$$

m is the mass of an atom or a molecule, u, v, w are the three velocity components

perpendicular to each other, and N is the total number of molecules in a volume V

containing n moles of gas.

But since

$$PV = nRT = \frac{N}{N_A}RT = NkT,$$

$$P = \frac{NkT}{V}$$

(2.12)

Combining Equation 2.11 with 2.12,

$$\frac{1}{3}m\,\overline{c^2} = kT$$

(2.13a)

or

$$\frac{1}{2}m\,\overline{c^2} = \frac{3}{2}kT$$

(2.13b)

which shows that the temperature of a gas is proportional to the average kinetic energy of

the molecules.

Another important property of the gas is called the mean-free path, λ_{mfp}, which is

dependent on the pressure. It is defined as the mean distance traveled by molecules

between successive collisions. The importance of long mean free path for the cone

formation was mentioned in Chapter 1. The relationship between the mean free path and

the pressure can be expressed using the formula

$$\lambda_{mfp} = \frac{kT}{\sqrt{2}\,\pi P \sigma^2} \qquad (2.14)$$

where σ is the molecular diameter.

For molybdenum thin film deposition, the molybdenum source usually melts

instead of subliming. The melting point of molybdenum is about 2895K. Therefore, the

temperature of the molybdenum source for evaporation is usually higher than 2895K. To

take an example, if the temperature of molybdenum vapors are 3500K, the mean free path

(λmfp) at 3500K can be calculated using Equation 2.14. For molybdenum BCC, the

lattice constant is 3.1469Å. Therefore, the molecular diameter σ is 2.727Å. The mean

free path as a function of the gas pressure for molybdenum vapor at 3500K is shown in

Figure 2.1.

For electron beam evaporation, usually the system pressures are between 10^{-4}

to 10^{-5} Pa. From Figure 2.1, the mean free paths between these pressures are from

3 to 4 m. The substrate is suspended 22" (0.56m) above the evaporant source, which is

much shorter than the mean free path. The molybdenum gas molecules travel directly to

the substrate without any collision with the residual gas molecules in the vacuum system.
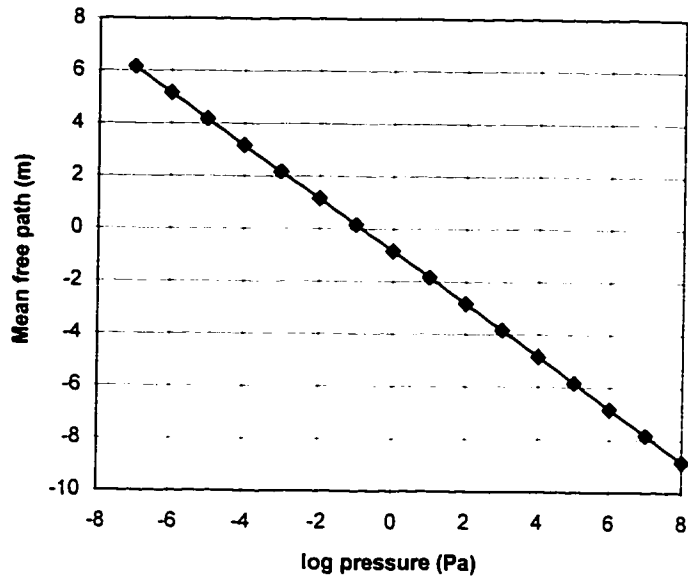
Figure 2.1: Mean free path of molybdenum vapor at 3500K.

The motion of gas molecules can be characterized by considering the entire range of possible values and frequencies of their velocities. The distribution function of molecular velocities was derived by J.C. Maxwell and L. Boltzmann,[21] which is called the Maxwell-Boltzmann formula. According to this formula, the fraction of molecules having velocities between c and c+dc is

$$f(c^2) \, dc = \frac{dN_c}{N} = \frac{4}{\sqrt{\pi}} \left| \frac{M}{2RT} \right|^{3/2} c^2 \exp\left(-\frac{Mc^2}{2RT}\right) dc \qquad (2.15a)$$

Similarly, the fraction of molecules having velocities between u and u + du in one particular direction is

31

$$f(u^2)\,du = \frac{dN_u}{N} = \frac{4}{\sqrt{\pi}} \left| \frac{M}{2RT} \right|^{3/2} u^2 \exp\left(-\frac{Mu^2}{2RT} \right) du \qquad (2.15b)$$

This centerpiece of the kinetic theory of gases states that the fractional number of molecules f(c), having velocities between c and c+dc, is related to their molecular weight (M) and absolute temperature (T). With constant temperature, a lower molecular weight of gases gives rise to a wider spread of velocity distribution, and a higher average velocity. On the other hand, with constant molecular weight, a lower temperature gives rise to a narrower spread of velocity distribution, and a lower average velocity. Moreover, it was found from the formula that molecules can have neither zero nor infinite velocity. Using Equation 2.15b, the molecular velocity distribution for molybdenum at temperature 3500K can be estimated and a bell shaped curve is obtained which is shown in Figure 2.2, where c_m, $\bar{c}$ and $\bar{c^2}$ are the most probable, average, and mean square velocities respectively.

To find out an expression for the evaporation rate of the evaporant atoms, it is important to know the velocity distribution of the atoms during travel from the source to the substrate. The relationship is derived in the next section.

2.4 Evaporation rate

According to the studies that were done by Hertz,[20] Knudsen[20] and later, Langmuir,[20] it was observed that a liquid or a free solid surface has a specific ability to
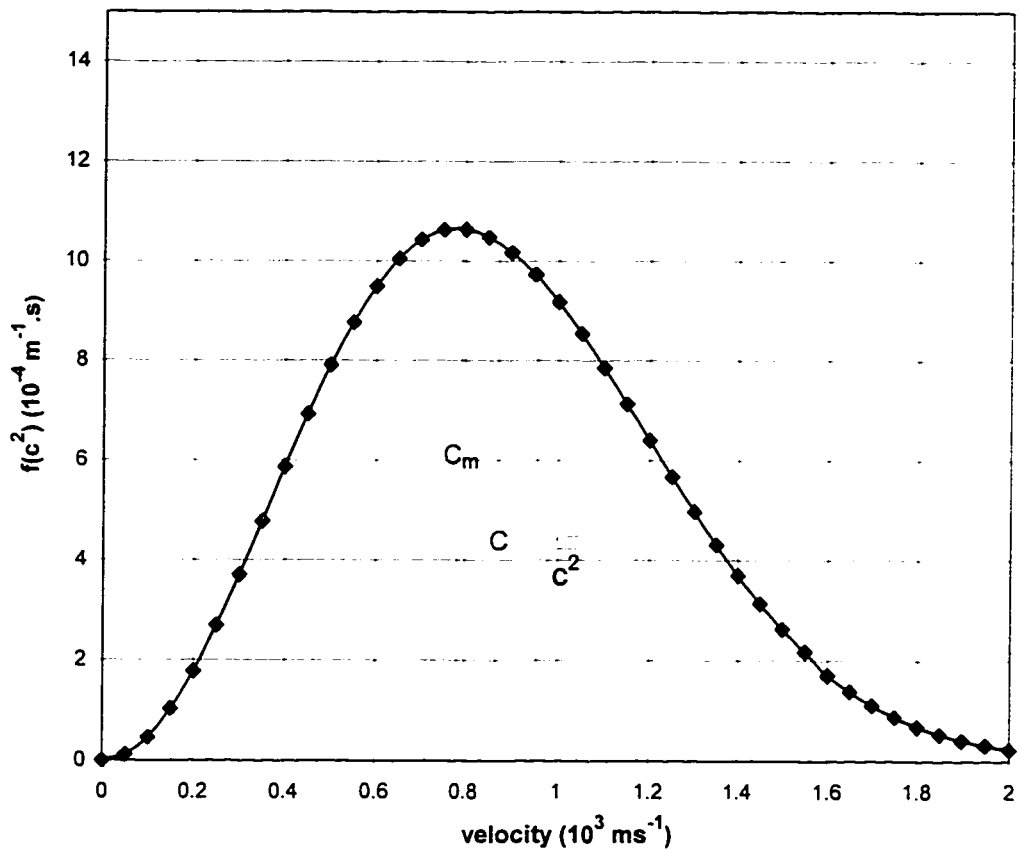
**Figure 2.2: Velocity distribution
for molybdenum vapor at 3500K.**

evaporate and cannot exceed a certain maximum evaporation rate at a given

temperature, even if the supply of heat is unlimited; and also the evaporation rates are

proportional to the difference between the equilibrium pressure P_e at the given

temperature and the hydrostatic pressure P_h (i.e. the system pressure) acting on the

evaporant.

The maximum evaporation rate is attained when the number of vapor molecules

emitted corresponds to that required to exert the equilibrium vapor pressure while none of

them return. In order to find the equation for the maximum evaporation rate, the gas

impingement flux on surfaces should be considered. This is a measure of the frequency with which molecules impinge on, or collide with, a surface.

2.4.1 Impingement rate of gas molecules on a surface

The impingement rate is the number of molecules that strike an element of surface (perpendicular to a coordinate direction) per unit time and per unit area. In a volume V containing N molecules with molecular weight M_g, the number of those having a certain velocity u is given by $dN_u = N$ f(u) du, where f(u) is the fractional number of molecules having velocities between u and u + du in one particular direction. Only a fraction of these molecules can reach the surface within a time interval dt, namely those which are within the striking distance udt. If A_w is the wall area under consideration, the fraction of the total volume which contributes to the impingement rate is (u dt A_w) /V. Therefore the number of molecules impinging with velocity u is

$$\frac{dN_u (u\ dt\ A_w)}{V} = \frac{N_u}{V}\ A_w\ f(u)\ du\ dt \qquad (2.16)$$

Since the molecular velocity ranges between zero and infinity, Equation 2.16 must be integrated for all velocities. According to the Maxwell-Boltzmann formula,

$$f(u) = \frac{dN_u}{N} = \left| \frac{M_g}{2\pi RT} \right|^{1/2} exp\ (\ -\frac{M_g\ u^2}{2RT}\ )\ du \qquad (2.17)$$

34

this operation yields $\int_0^\infty u\, f(u)\, du = (\dfrac{RT}{2\pi M_g})^{1/2}$ (2.18)

Therefore, the impingement rate which is the integration of Equation 2.16 divided by unit time and area, is

$$\Phi = \dfrac{dN_i}{A_w dt} = \dfrac{N}{V}(\dfrac{RT}{2\pi M_g})^{1/2}$$ (2.19a)

where dN_i is the total no. of molecules impinging with velocity range from zero to infinity.

But since $PV = nRT = (N/N_A)\, RT$

$$\dfrac{\Phi}{N_A} = \dfrac{P}{\sqrt{2\pi\, M_g\, R\, T}} \text{ moles } /cm^2\text{-sec}$$ (2.19b)

or $$\Phi = \dfrac{P\, N_A}{\sqrt{2\pi\, M_g\, R\, T}} \text{ molecules } /cm^2\text{-sec}$$ (2.19c)

2.4.2 The Hertz-Knudsen equation

As mentioned before, the theoretical maximum evaporation rates are obtained only if as many evaporant molecules leave the surfaces as would be required to exert the equilibrium pressure P^* on the same surface while none of them must return. In other words, the hydrostatic pressure $P_h = 0$ must be maintained. In that case, the

35

maximum evaporation rate is exactly equal to the gas impingement rate on the surface (Equation 2.19).

However in reality the hydrostatic pressure does not equal zero, so the P_h must be included in the equation. Therefore, pressure P in Equation 2.19 is replaced by the equilibrium pressure P^* minus a return flux corresponding to the hydrostatic pressure P_h of the evaporant in the gas phase. Moreover, it was argued that molecules impinging on the evaporating surface may be reflected back into the gas rather than incorporated into the liquid. In such case, an evaporation coefficient α_e is introduced to account for this situation. Therefore, the most general form for the rate of evaporation equation from both liquid and solid surfaces is

$$\Phi_e = \frac{\alpha_e N_A (P^* - P_h)}{\sqrt{2\pi M_g R T}} \text{ molecules /cm}^2\text{-sec} \qquad (2.20)$$

The evaporation coefficient α_e takes value from 0 to 1. It is strongly dependent on the condition of the surface, such as the cleanliness of the surface.[21] In general, a more contaminated surface contributes a smaller value of the coefficient value. Another useful expression of the evaporation rate is the mass evaporation rate (Γ) which simply converts the units of Equation 2.20 into g /cm^2-sec. This can be done by multiplying Equation 2.20 with the mass of an individual molecule $m = M_g / N_A$. Therefore, if the evaporant coefficient is equal to zero,

36

$$\Gamma = \Phi_e \; \frac{M_g}{N_A}$$

$$\Gamma = 5.834 \times 10^{-2} \, (P^* - P_h \,)\overline{\sqrt{M_g / T}} \quad g \, /cm^2\text{-sec} \qquad (2.21)$$

In thin film deposition, the deposition rate is more important than the evaporation

rate because it is a measurable value during evaporation. An expression of deposition

rate can be derived from the evaporation rate.

2.4.3 Deposition rate of thin film deposition

Besides the evaporation rate, the deposition rate of a thin film is dependent on the

shape of the evaporant source, as well as the orientation and placement of substrates.[21]

Evaporation from a point source is the simplest of situations to model. Refer to

Figure 2.3,[21] evaporant particles are imagined to emerge from an infinitesimally small

region(dA_e) of a sphere of surface area A_e with a uniform mass evaporation rate. The

total evaporated mass M_e is then given by the double integral

$$M_e = \int_0^t \int_{A_e} \Gamma \, dA_e \, dt \qquad (2.22)$$

where Γ is the mass evaporation rate and the expression can be found in Equation 2.21.

Of this amount, mass dM_s falls on the substrate of area dA_s. Since the projected area

dA_s on the surface of the sphere is dA_c, with $dA_c = dA_s \cos\theta$, the proportionality

dM_s: $M_e = dA_c$: $4\pi r^2$ holds. Finally, the mass deposited per unit area from a point

source is

37

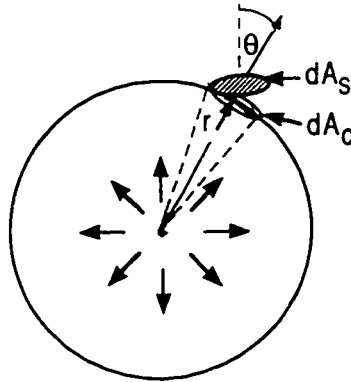$$\frac{dM_s}{dA_s} = \frac{M_e \cos\theta}{4\pi r^2}$$

(2.23)

Figure 2.3: Evaporation from a point source.[21]

On the other hand, mass deposited per unit area from a small area or surface

source was found [21] to be dependent on two angles (emission and incidence) that are

defined in Figure 2.4. The expression is shown in Equation 2.24.

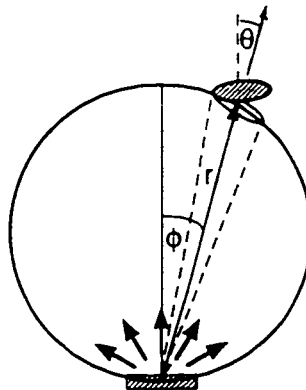$$\frac{dM_s}{dA_s} = \frac{M_e \cos\theta \cos\phi}{\pi r^2}$$

(2.24)

Figure 2.4: Evaporation from a surface source.[21]

38

Boat filaments and wide crucibles containing a pool of molten material to be evaporated approximate surface sources in practice.

Consider evaporation from the point source and the small surface source onto a parallel plane-receiving substrate surface as indicated in Figure 2.5. The film thickness t is given by $dMs/ \rho \, dAs$, where ρ is the density of the deposited film. For the point source,

$$t = \frac{M_e \cos\theta}{4\pi\rho r^2} = \frac{M_e \, h}{4\pi\rho \, r^3} = \frac{M_e \, h}{4\pi\rho \, (h^2 + l^2)^{3/2}} \quad cm \qquad (2.25)$$

since $M_e = \int_0^t \int_{Ae} \Gamma \, dA_e \, dt$, the deposition rate for evaporation from the point source onto a parallel plane-receiving substrate surface is

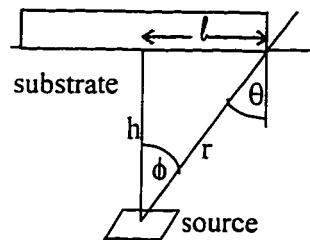$$\dot{d} = \frac{\Gamma \, h \int_{Ae} dA_e}{4\pi\rho \, (h^2 + l^2)^{3/2}} \quad cm/s \qquad (2.26a)$$

Figure 2.5: Geometry of evaporation onto parallel plane substrate.

or, inserting Equation 2.21 for the evaporation rate,

$$\overset{\bullet}{d} = \frac{5.834 \times 10^{-2} \times (P_e - P_h)\ h \int_{A_e} dA_e}{4\pi\,\rho\,(h^2 + l^2)^{3/2}} \sqrt{M_g / T}\ \text{cm /sec} \qquad (2.26b)$$

Similarly, for the surface source,

$$t = \frac{M_e \cos\theta\ \cos\phi}{\pi\rho r^2} = \frac{M_e}{\pi\rho r^2}\frac{h}{r}\frac{h}{r} = \frac{M_e h^2}{\pi\rho (h^2 + l^2)^2}\ \text{cm} \qquad (2.27)$$

therefore, the deposition rate for a surface source is

$$\overset{\bullet}{d} = \frac{\Gamma h^2 \int_{A_e} dA_e}{\pi\rho (h^2 + l^2)^2}\ \text{cm/s} \qquad (2.28a)$$

or

$$\overset{\bullet}{d} = \frac{5.834 \times 10^{-2} \times (P_e - P_h)\ h^2 \int_{A_e} dA_e}{\pi\,\rho\,(h^2 + l^2)^2} \sqrt{M_g / T}\ \text{cm /sec} \qquad (2.28b)$$

For molybdenum evaporation, only a small amount of Mo source is melted which is the electron beam hitting region, and the appropriate equation to use is Equation 2.26.

2.4.4 Relationship between deposition rate (d˙)and source temperature (T)

The relationship between deposition and source temperature can be found from Equation 2.26 or 2.28. For electron beam thin film deposition, the hydrostatic pressure (P_h) is usually very low compared to the equilibrium pressure (P_e). Therefore the term P_h can be ignored from Equation 2.26 or 2.28. Using the Clausius-Clapeyron equation,

40

the equilibrium pressure (P_e) can be expressed as $\ln P_e \cong - \Delta H/RT + I$ where $\Delta H/R$ and I

are constant values. If the distance between the substrate and the source is fixed, and the

thickness measuring point is taken at a fixed region, the terms h and l are also constant.

Moreover, if the beam size does not change, the evaporated surface area $\int_{A_e} dA_e$ will be

constant as well. Finally, for a fixed evaporant source, the molecular weight (M_g) and the

thin film density (ρ) are also constant. Therefore, source temperature (T) is the only

unknown variable in the equation for deposition rate. In other words, there is a direct

relationship between the deposition rate and the source temperature, expressed as:

$$\dot{d} \propto \frac{\mathrm{Exp}\,\text{-}(1/T)}{\sqrt{T}}$$

Since the exponential term exp (-1/T) has a stronger temperature dependence than the

square root term ($\sqrt{T}$), there is an exponential relationship between the deposition rate

and the source temperature:

$$\dot{d} \propto \exp\,(\text{-}1/T)$$

2.5 Film purity

There are three major kinds of impurities that affect the chemical purity of

evaporated films. They are: impurities that are initially present in the source,

contaminants from the heater, crucible, or support materials, and impurities originating

from the residual gases present in the vacuum system.

In electron beam evaporation, assuming the source is of high purity, impurities

41

from the other two categories must be considered. Fortunately, the evaporant source is placed in either a water-cooled crucible or in the depression of a water-cooled copper hearth. The purity of the evaporant is ensured because only a small amount of charge melts or sublimes so that the effective crucible is the unmelted skull material next to the cooled hearth. Therefore, most of the impurities are from the residual gases. During deposition, the atoms and molecules of both the evaporant and residual gases impinge on the substrate independently. The purity of evaporant films is strongly dependent on the ratio of the evaporant to the residual gas impingement rate (molecules/cm^2-sec).

As mentioned in the last section, the deposition rate of the evaporant atoms is $\dot{d}$ (cm/sec). Therefore, the evaporant vapor impingement rate is $\rho\, N_A\, \dot{d}\, / M_e$ molecules/cm^2-sec, where ρ and M_e are the density and the molecular weight of the evaporant respectively. Simultaneously, the impingement rate of the residual gas molecules from the vacuum system rate is given by Equation 2.19c. The impurity concentration C_i is defined as:

$$C_i = 5.82 \times 10^{-2}\; \frac{P}{\sqrt{M_g}\, T}\; \frac{M_e}{\rho\, d} \qquad (2.29)$$

where P is the residual gas vapor pressure in torr.

Therefore, to produce very pure films, it is important to deposit evaporant at very high rates while maintaining very low background pressures of residual gases such as H_2O, CO_2, CO, O_2 and N_2.

Electron beam evaporation is the most widely used vacuum evaporation technique

for preparing highly pure films. In principle, it enables evaporation of virtually all materials at almost any rate; deposition rates from electron-beam sources can reach 1000Å /sec at a chamber pressure of 10^{-8} torr.[21]

2.6 Nucleation and growth of thin films

Thin film formation involves the processes of nucleation and growth.[22] During the earliest stages of film formation, i.e. soon after exposure of the substrate to the incident vapor, a sufficient number of vapor atoms or molecules condense and establish a permanent residence on the substrate. This is the nucleation stage. In this stage, there is a uniform distribution of small but highly mobile clusters or islands formed. Afterwards, the prior nuclei incorporate with the impinging atoms and subcritical clusters and grow in size while the island density rapidly saturates. The growth stage involves merging of the islands by a coalescence phenomenon. Coalescence decreases the island density, resulting in local denuding of the substrate where further nucleation can then occur. Coalescence continues until a connected network with unfilled channels in between develops. With further deposition, the channels fill in and shrink, leaving isolated voids behind. Finally, even the voids fill in completely, and the film is said to be continuous. This collective set of events occurs during the early stages of deposition, i.e. for the first few hundred angstroms of film thickness.[22] A schematic illustration of the sequential steps occurring during nucleation and the early stages of film growth is shown in Figure 2.6.
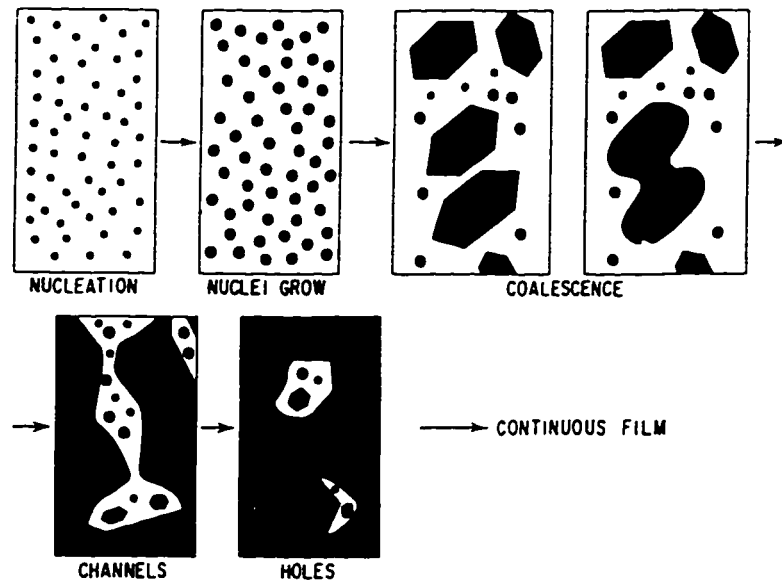
NUCLEATION NUCLEI GROW COALESCENCE

CHANNELS HOLES ──► CONTINUOUS FILM

Figure 2.6: Illustration of sequential steps during nucleation and the early stages of film growth.[22]

Chapter 3: Configuration and Operation of System for Electron Beam Evaporation

This chapter introduces the configuration and operation of the system used for electron beam evaporation. Apparatus and systems used in this thesis included an Airco Temescal STIH-270-2M electron beam system, with a mechanical pump and a cryopump, a Dektak-II profilometer, and a custom designed substrate holder.

3.1 Configuration of the electron beam evaporation system

The electron beam evaporation system consists of the following major components: an electron beam evaporation unit, a bell jar, vacuum pumps, vacuum gages, evaporation sources, and crystal oscillators. Schematic diagrams showing the external and internal features of the electron beam evaporation system are illustrated in Figure 3.1 and Figure 3.2 respectively.

The Airco Temescal Model STIH-270-2M has four copper crucibles. They are designed to evaporate four different materials sequentially or to provide a long uninterrupted run with a single evaporant. In the experiments of this thesis, only a single evaporant was used, a molybdenum source.

3.1.1 The nature of electron beam

The Airco Temescal Model STIH-270-2M supersource operates on principles similar to the cathode ray tube. A tungsten filament heated to incandescence in vacuum
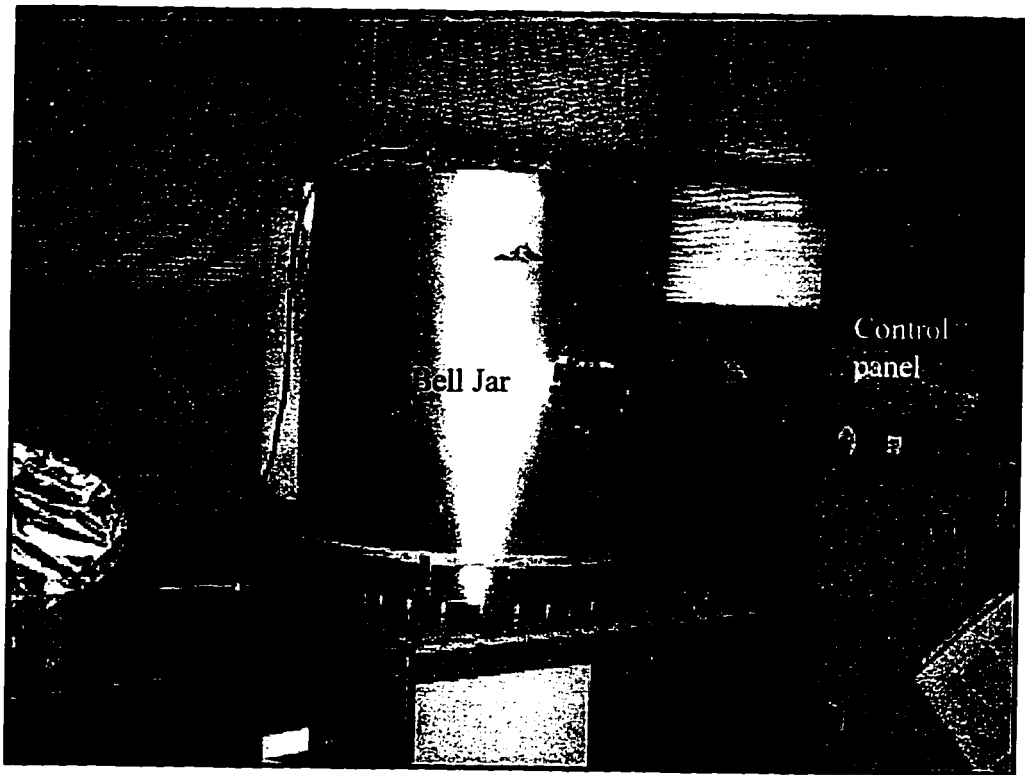
Figure 3.1: External view of the electron beam evaporator.

emits electrons by thermionic emission. The filament cathode assembly potential is biased negatively with respect to a nearby grounded anode, and this serves to accelerate the electrons. Since electrons are sensitive to electrostatic and magnetic fields, their paths can be directed. An electron beam of sufficient energy will vaporize any known substance.[21]

When power is applied to the emitter filament, electrons are emitted randomly. The cavity on the side and at the back of the filament, which is at the same high negative potential as the filament itself, produces an electrostatic field which forms the beam. In addition, a magnetic field created by a permanent magnet, pole pieces, pole piece
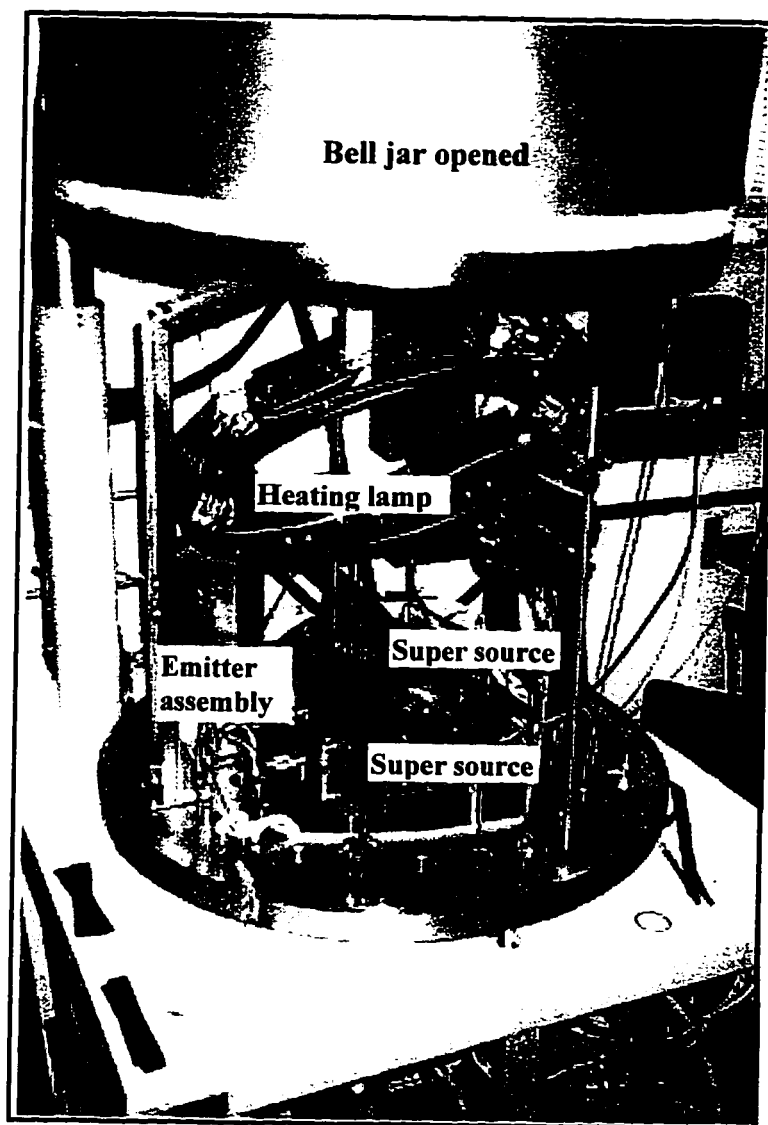
Figure 3.2: Internal view of the electron beam evaporator.

extensions, and the electromagnetic deflection coil, deflect the beam through a 270°

circular arc and focus it on the hearth and evaporant source at ground potential.[23] A

schematic diagram showing the deflection of the electron beam is shown in Figure 3.3.
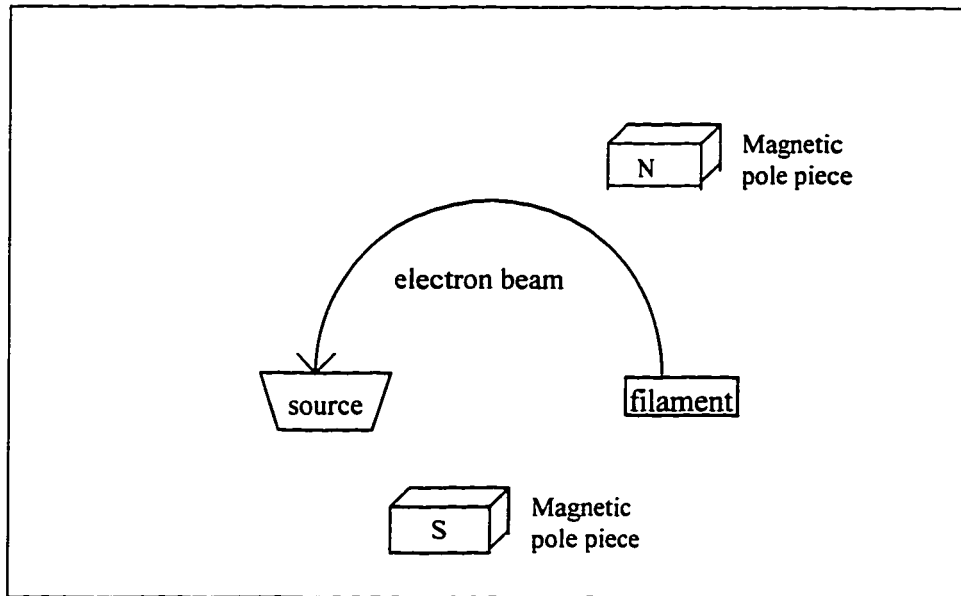
Figure 3.3: A schematic diagram showing the deflected electron beam.

3.1.2 Operation control of the electron beam

The electron beam can be controlled by varying the emission voltage, emission

current, and focus current. The maximum power of the system is 10 KW. The

emission voltage can be adjusted between 4 kV and 10 kV. The energy of the beam

varies directly with the emission current. The focus current is the current which passes

through the electromagnetic deflection coil. Both longitudinal and lateral adjustment of

the beam position are possible by adjusting focus current. By changing the current in

either one of the electromagnetic coils, the beam can be made to traverse a straight line.

The amplitude of the sweep is determined by the currents delivered to the electromagnet.

If the beam sweep is activated for both coils simultaneously, the beam can be made to

sweep over the entire area of the evaporant. The permanent magnet along with the two

large pole pieces maintain the beam on the area of the crucible. The adjustable pole piece

extensions control the beam shape. When attached, they tighten the beam. Sliding them

in toward the center of the source tightens the beam, sliding them out diffuses the beam.[23]

The approximate spot sizes for a tight beam and a diffused beam are shown in Figure 3.4.
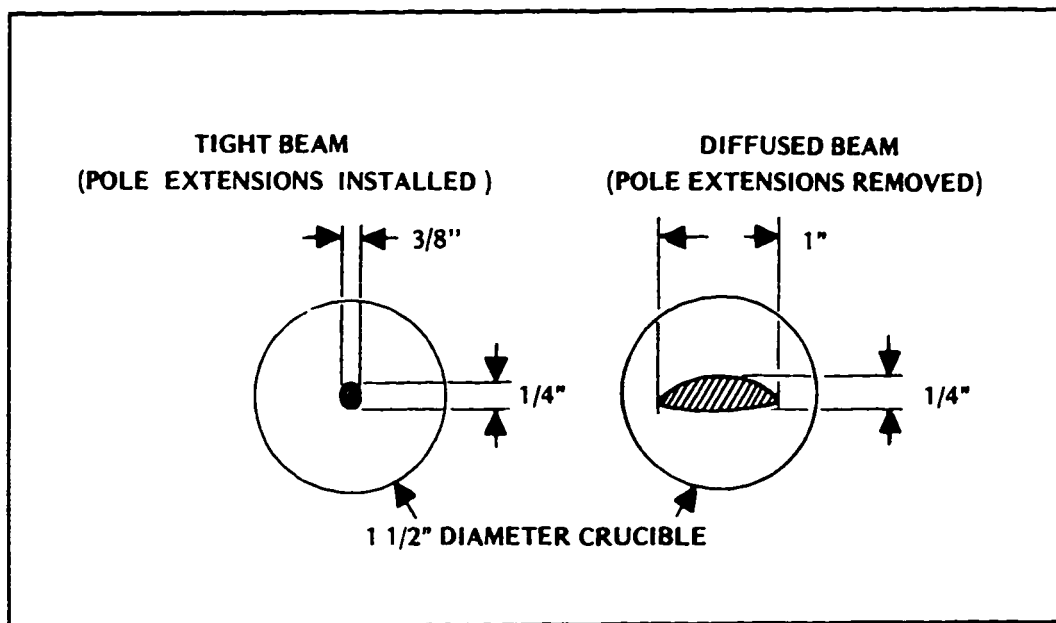

TIGHT BEAM
(POLE EXTENSIONS INSTALLED)

DIFFUSED BEAM
(POLE EXTENSIONS REMOVED)

3/8"

1"

1/4"

1/4"

1 1/2" DIAMETER CRUCIBLE

Figure 3.4: Approximate spot sizes with pole piece extensions on and off.[23]

3.1.3 Heat loss during electron beam evaporation

When the power is delivered by the electron beam to the evaporant source, there is

some power loss during evaporation. In other words, only a portion of the supplied

energy is used to vaporize and accelerate the evaporant atoms. Heat losses incurred

during evaporation of N atoms/cm^2-sec include:

i. The power density P_s that must be supplied to account for the heat of sublimation ΔH_s (eV) is

$$P_s = N \, (\, 1.6 \times 10^{-19} \,) \, \Delta H_s \quad \text{watts/cm}^2 \qquad (3.1\text{a})$$

ii. The radiation heat loss density is

$$P_r = 5.67 \times 10^{-12} \, \varepsilon \, (T_s^4 - T_0^4) \quad \text{watts/cm}^2, \qquad (3.1\text{b})$$

where ε is the source emissivity at the source temperature T_s, and $T_0 \approx 293\text{K}$.

iii. Heat conduction through a charge of thickness l into the hearth dissipates a power density P_c equal to

$$P_c = \kappa \, \left(\frac{T_s - T_0}{l} \right) \quad \text{watts/cm}^2, \qquad (3.1\text{c})$$

where κ is the thermal conductivity of the evaporant source.

iv. The remaining portion of the power will be converted to kinetic energy of the evaporant atoms, which is $(3/2 \, kT_s)$ per atom so that the converted power density P_k is

$$P_k = N \, (3/2) \, (1.38 \times 10^{-23} \,) \, T_s \quad \text{watts/cm}^2 \qquad (3.1\text{d})$$

3.1.4 Quartz crystal oscillators

Quartz crystal oscillators are used to monitor the film thickness that is deposited and to measure the instantaneous deposition rate during deposition. They are mounted within the evaporation chamber close to the substrate. The quartz crystal oscillators are set into mechanical vibration to produce resonant frequencies. This frequency is

dependent on the thickness of the crystals. If there is a small amount of film mass

deposited on the quartz crystal, the thickness of the crystal will be increased. Therefore,

there will be a frequency change. From the frequency change, we know the film

thickness deposited on the crystal if the density of the film is known. The change in

frequency is measured by beating the crystal signal against an undeposited crystal and

their frequency difference is counted. This is the principle that explains the use of crystal

oscillators to measure film thickness, since the film thickness deposited on the substrate

and the crystal is proportional (but not the same) to each other. The difference between

the actual film thickness and the thickness taken by the crystal oscillator is due to the

different position of the crystal oscillator and the substrate holder. A tooling factor is

required to compensate the difference. To measure the deposition rate, the frequency

change will be differentiated with respect to time. A quartz crystal oscillator used for this

thesis is shown in Figure 3.5.

3.1.5 Operation of the electron beam system

Before deposition, a molybdenum source was put in the water-cooled hearth, and

the substrate holder with the wafer samples attached on it was mounted inside the bell jar

of the evaporation system. A final inspection of the cleanliness of the evaporator was

performed before the bell jar was closed. Loose flakes and debris from previous

depositions may cause short circuits if they blow into the emitter assembly. Moreover,

they may outgas and decrease the efficiency of the vacuum pump. A vacuum

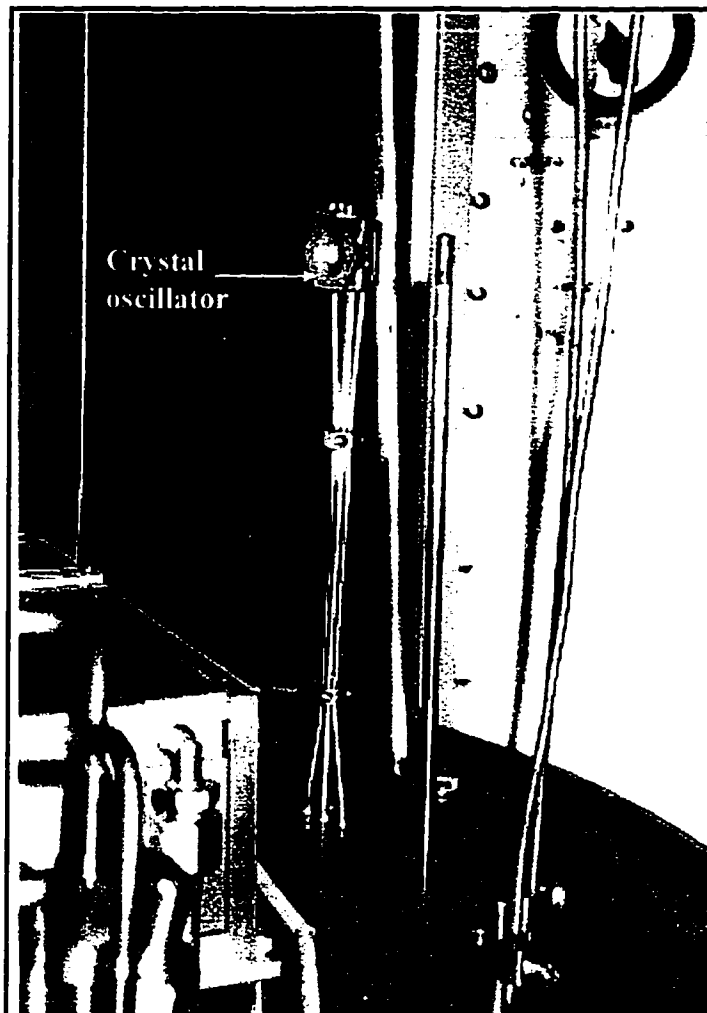cleaner was used to remove these materials.

Figure 3.5: A quartz crystal oscillator.

After the bell jar was closed, the roughing pump was turned on to start the

pumping. The roughing pump was turned off when the pressure was below

50 - 100 mtorr. The cyropump was then switched on to pump out the residual gas until

the pressure reached 10^{-5} to 10^{-6} torr.

The power supply of the electron beam system was then turned on. The high

voltage and filament current were fixed and maintained at 10 kV and 0.25A

respectively. After the focus current was adjusted so that the electron beam was focused

on the Mo evaporant source, beam current was turned on very slowly until the evaporant

glowed orange red. The beam current should be about 0.3A to 0.4 A. When increasing

the beam current slowly, the system pressure was checked to make sure there was no

increase in pressure due to the outgasing from the evaporant source. When the electron

beam and the pressure were stable, the system was ready to start the deposition. The

beam current was turned to 0.35A or more, and the protection shutter, which was right

above the evaporant source, was opened. The deposition time was monitored.

When the deposition was done, the power of the electron beam evaporator was

turned off. The system was then vented to ambient pressure until the evaporator was

cooled down.

3.2 Profilometer

Profilometery is a stylus method of measuring thickness of a deposited film. It

works by measuring the mechanical movement of a stylus as it traces the topography of a

film-substrate step. A diamond needle stylus with a tip radius of about 10 μm serves as

the electromagnetic pickup.[21] Film thickness is directly read out as the height of the

resulting step contour trace. The vertical stylus movement is digitized, and the data can

be processed to magnify areas of interest and yield best profile fits. The measurement

range spans distances from 200Å to 65 μm, and the vertical resolution is about 100 Å.[21]

A Dektak-II profilometer is shown in Figure 3.6. An example of a film thickness profile

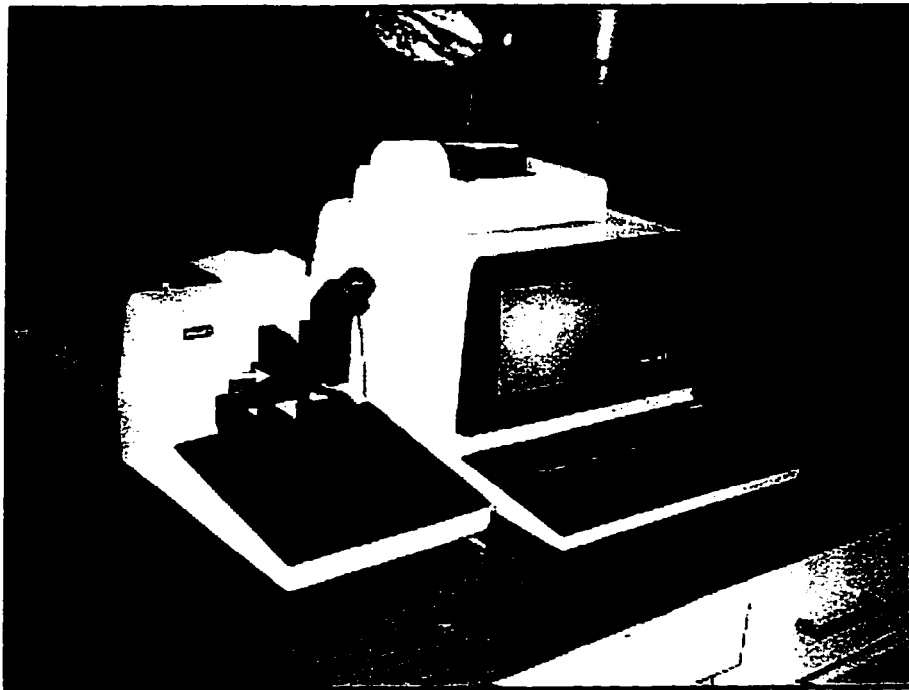output obtained by the Dektak-II measurement is shown in Figure 3.7.
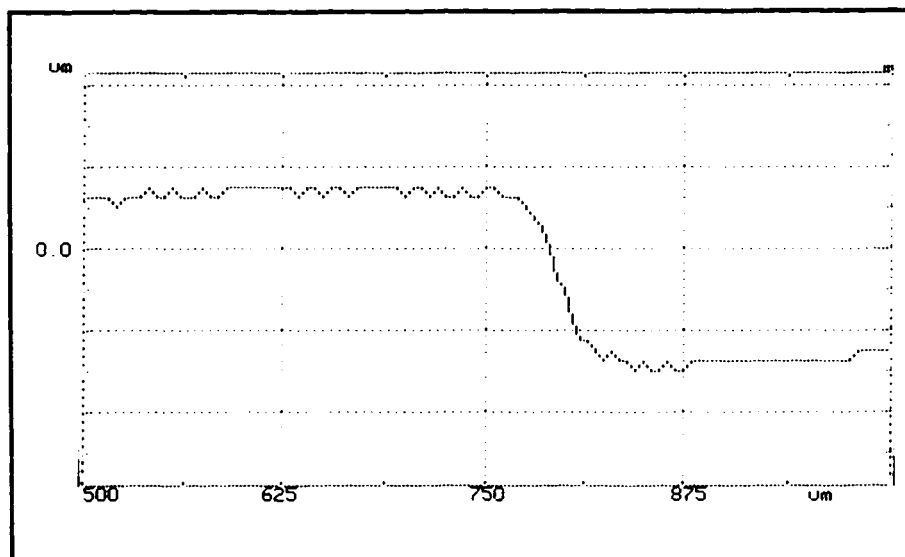
Figure 3.6: A Dektak-II profilometer.

Figure 3.7: A profilometer trace of film thickness profile output.

3.3 A custom-designed substrate holder

Instead of using the planetary rotating substrate holder, a custom-designed substrate holder was used for the experiment in this thesis. The technical drawing of the custom designed substrate holder is shown in Appendix A. To form a cone, molybdenum atoms should be deposited through the holes at normal incidence. The plane-receiving substrate surface should be placed above and parallel to the evaporant source, along the same axis as the center of the source. A planetary rotating substrate holder contributes to a uniform coverage. However, it may lead to sidewall coverage of the cavity because the planetary rotating substrate holder is placed at an angle with the evaporant source. Whether the film coverage is uniform or not is not critical for the cone formation, since the film layer will be lifted off afterwards. There should be no influence on the shapes and heights of the cones, which are dependent mainly on the hole diameters, and the structure of the cavities according to Section 1.3.3.1.

In this thesis, the substrate holder was mounted 22" above the source along the same axis. The shape of the custom-designed substrate holder is shown in Figure 3.8. The set up of the substrate holder inside the bell jar of the E-beam system is shown in Figure 3.9.
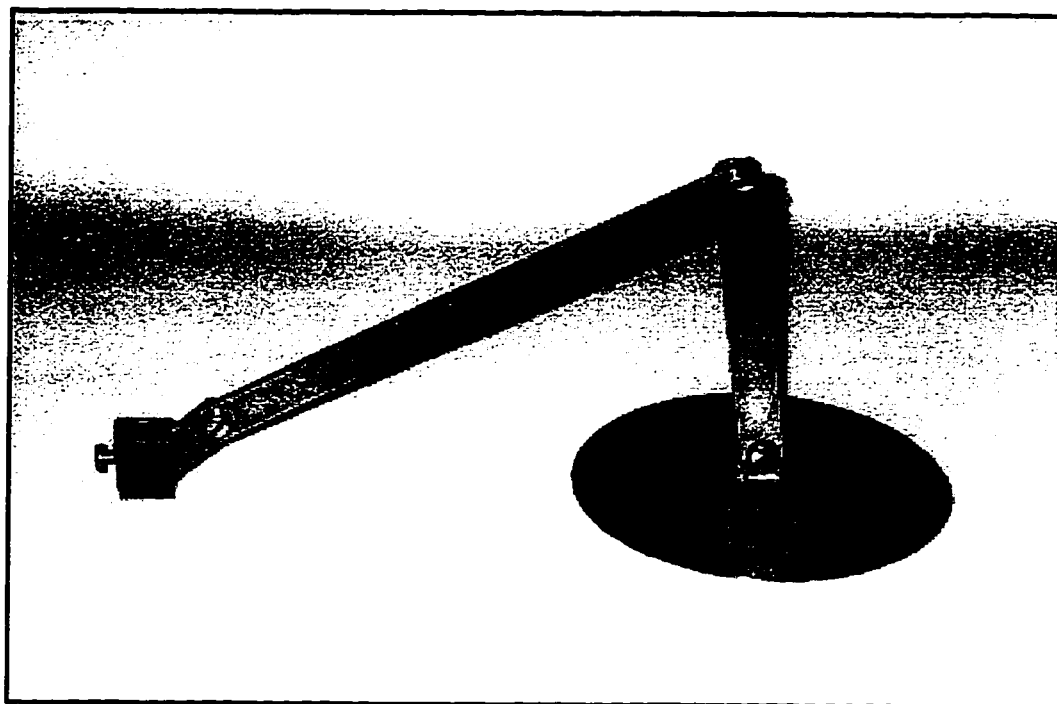
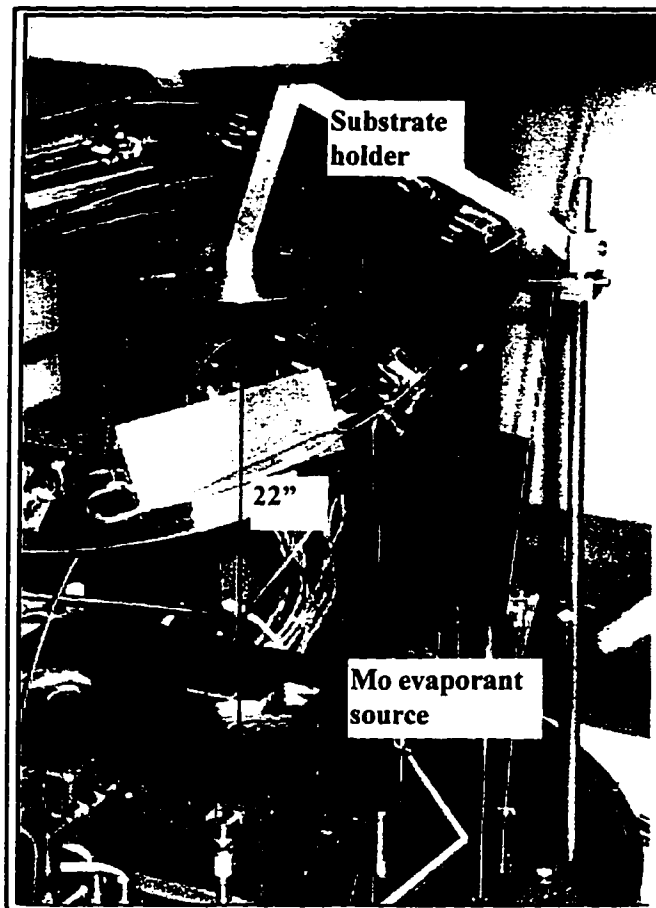Figure 3.8: A custom-designed substrate holder.

Figure 3.9: The set up of the substrate holder inside the bell jar of E-beam system.

Chapter 4: Characterization of Molybdenum Thin Film Deposition

4.1 Introduction

The purpose of this phase was to characterize the molybdenum thin film deposition. The aim was to develop a controllable deposition process, which required determining the relationship between the deposition rate, power supplied to the electron beam and the shape of the evaporant source. Deposition parameters and results such as operating power, system pressure, deposition thickness and time, and the change of shape of the molybdenum source were monitored.

Different forms of molybdenum materials were used to prepare the molybdenum evaporant source. They included molybdenum granules (0.5 x 0.5 mm), big cylindrical pellets (12 x 6 mm), and small cylindrical pellets (6 x 6 mm).

In each deposition, a 4" bare silicon wafer sample with a square glass slide (1"x 1") attached near the center was mounted on the wafer holder for the electron beam deposition. After deposition, the deposited wafer was removed. The glass slide which served as a shadow mask was detached from the wafer and a square-shaped step region was seen. A profilometer was used to measured the thickness of the deposition. Four thickness measurements were taken for each wafer sample, with each measurement taken along each side of the step region. A schematic diagram indicating the measurement locations is shown in Figure 4.1.
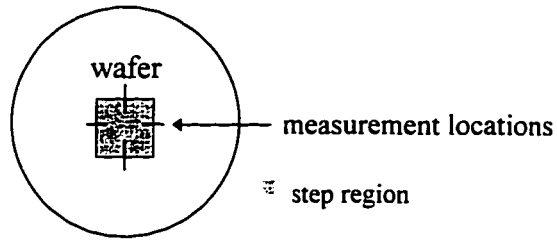
Figure 4.1: A schematic diagram showing the measurement locations.

4.2 Results and Discussion

4.2.1 Relationship between input power and deposition rate

Molybdenum was deposited on six bare silicon wafers using different values of beam current, keeping the beam voltage at 10 kV. Film thickness was measured and the deposition rate (Å/s) was calculated by dividing the film thickness by the deposition time. The data is shown in Table 4.1 and a plot of the deposition rate with respect to the input power is shown in Figure 4.2.

Table 4.1: Deposition rate as a function of input power

Beam current (A)	0.28	0.3	0.35	0.38	0.4	0.42
Input power (KW)	2.8	3	3.5	3.8	4	4.2
Deposition thickness (Å)	118 ± 10	422 ± 15	1923 ± 53	4326 ± 130	3480 ± 72	5700 ± 130
Deposition time (min)	10	10	5	3	1	1
Deposition rate (Å/s)	0.2 ± 0.0	0.7 ± 0.0	6.4 ± 0.2	24 ± 0.7	58 ± 1.2	95 ± 2

Figure 4.2 shows that a minimum power of 3 kW is required for a measurable deposition rate. When the beam power was increased to more than 3.5 kW, there was a tremendous increase in the deposition rate.
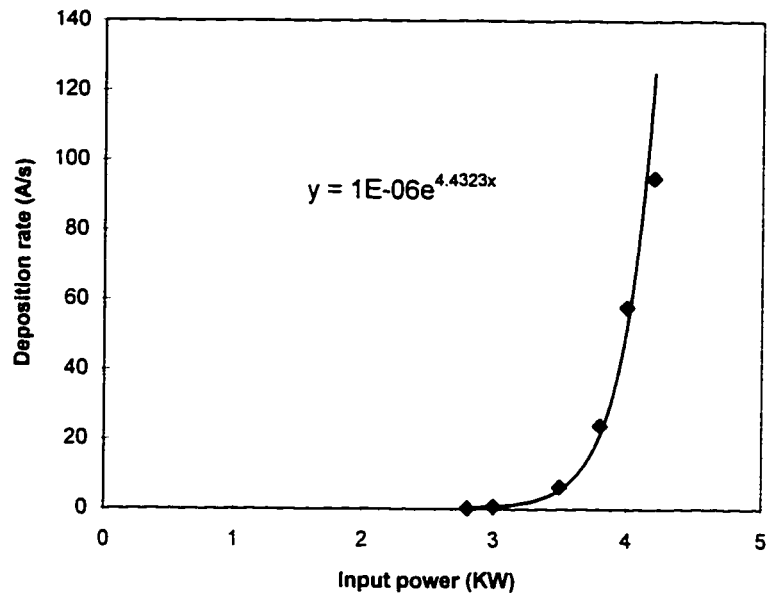
59

Figure 4.2: Deposition rate vs input power.

A curve was fit to the data and the deposition rate was found to be

exponentially dependent on the input power. The exponential relationship may be

explained by recalling the relationship between power density and temperature. From

Section 3.1.3, a portion of the total power must be delivered by the electron beam to the

evaporant charge to compensate for the heat loss incurred from the heat of sublimation,

the radiation heat loss density, and the heat conduction through the evaporant into the

hearth. The remaining portion of the power will be converted to kinetic energy of

evaporant atoms (3/2 kT). Power dissipation should be a constant under similar

deposition conditions; and thus the input power (P) = Heat loss (constant) + 3/2 kT,

i.e., $T \propto P$. On the other hand, from Section 2.4.4, the relationship between deposition

rate $(\dot{d})$ and temperature (T) is $\dot{d} \propto \exp(-1/T)$. Thus $\dot{d} \propto \exp(-1/P)$ or $\dot{d} \propto \exp(P)$.

Therefore, there is an exponential relationship between deposition rate and input power if

the deposition conditions are consistent.

60

Figure 4.2 implies that the deposition rate continues to increase exponentially above 6 kW. However in reality, as the evaporation rate is increased to a certain level, the cloud of evaporant atoms above the source would become denser, and thus there would be a greater chance that the electrons in the beam would collide with atoms of evaporant and give up their energy. This process of ionization represents a loss of efficiency of the electron beam energy, which will lower the deposition rate.

Most materials are not able to absorb all the power available from the power supply, and increasing the power above what can be absorbed causes spitting. The maximum power an evaporant source can usefully absorb is limited to that which it can be dissipated. If the energy density exceeds that which can be dissipated, explosive instabilities occur, causing spitting. For molybdenum evaporation, it was found that the input power can not be higher than 4.5 kW, otherwise spitting occurs.

4.2.2 Fluctuation of deposition rate

A second set of 22 bare silicon wafer samples were used to further characterize the molybdenum thin film deposition. Operating parameters and deposition results for each deposition are shown in Appendix A. Input powers and deposition rates of these 22 depositions are presented in Figure 4.3.

In comparsion to Figure 4.2, it was found that instead of obtaining an exponential relationship between deposition rate and input power, the data was scattered. There were deviations of deposition rates even when the same deposition power was used. All 22 depositions had deposition rates lower than those which were shown in Table 4.1. A
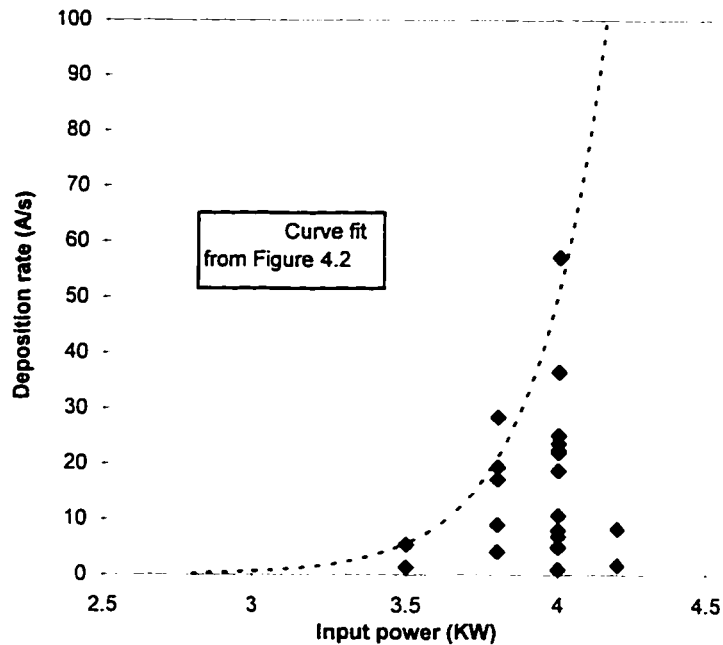
Deposition rate (A/s)

100
90
80
70
60
50
40
30
20
10
0

2.5   3   3.5   4   4.5

Curve fit from Figure 4.2

Input power (KW)

Figure 4.3: Deposition rate vs Input power.

question arose as to why the relationship $d \propto \exp (P)$ was not held in these depositions. This may be explained by carefully investigating the change of shape of the molybdenum source. From observation, the first six depositions shown in Table 4.1 were done using a uniform dome-shaped evaporant source, as shown in Figure 4.4. Moreover, the deposition time was very short for the first six depositions, and the total amount of molybdenum evaporated was very small. Thus, the shape of the source remained almost unchanged. However for the second set of 22 depositions, the deposition rate gradually decreased from 57.2 Å/s to 25.2 Å /s for 4 kW. The decrease appears to be due to the gradual deformation of the dome shape of the source after each deposition. This deformation may partly be due to the longer deposition times for these depositions. After a few depositions, the surface of the source appeared very irregular and uneven. The deposition rate dropped to about 15 Å /s for 4 kW. Eventually, there were some dents

found on the source. The deposition rate dropped to 4 Å /s for 4 kW. The change of the shape of molybdenum source is shown in Figure 4.4.

Mo dome shaped source

Mo evaporant cone

Mo source deformed

Mo evaporant cone

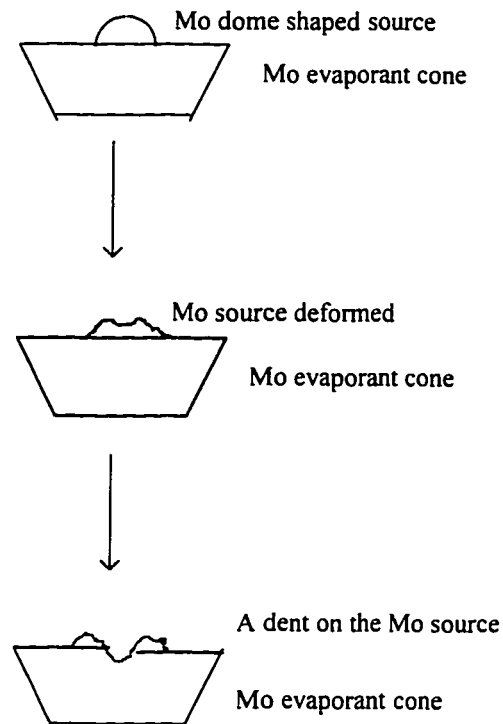A dent on the Mo source

Mo evaporant cone

Figure 4.4: The change of the shape of molybdenum source after deposition.

From the change of deposition rate mentioned in the previous paragraph, it is believed that the shape of the source has a significant influence on the deposition rate. If the evaporant source was high and smooth, with a dome shape, the whole evaporant source glowed to reddish yellow. Moreover, plasma was observed all over the evaporant surface. From the glowing appearance of the source, it is believed that electric charges were distributed evenly on the lump surface. Thermal energy was very efficiently and

evenly distributed all over the surface. On the other hand, if the lump surface was irregular or too flat, the glowing area was confined to a small spot. Also, the electron beam was found to be very unstable during deposition. It is believed that as the surface became irregular, the system was unable to focus the beam and instead, it was scattered over the many edges and voids, causing uneven heating and fluctuations in evaporation rate. Some power was lost due to the electron beam scattering.

To investigate the importance of an evaporant to the deposition rate, a deposition was done without any evaporant source formed on the evaporant cone. There was almost no deposition observed. This means that even though the evaporant cone was made of molybdenum, it was not efficient for molybdenum deposition, since the electric charges were confined in one spot instead of evenly distributed over the surface. Therefore, thermal energy was supplied to only one spot. As deposition continued, only this spot was melted, and a crater was created on the evaporant cone surface, which deepened and collimated the stream of evaporant. The electron beam was trapped and scattered inside the crater, causing non-uniform distribution of electric charges which made the deposition very inefficient.

In conclusion, a good source is required to obtain a controllable deposition. A perfectly dome-shaped source can provide a constant deposition condition, and a higher, and more consistent evaporation rate. Electric charges are distributed evenly along the whole surface, and the thermal heating is very uniformly distributed. Localized heating is avoided, and thus explosive instabilities which cause spitting can be minimized. Therefore, the evaporation rate or deposition rate is constant and uniform. On the other

hand, if the surface of the source is irregular, the electron beam fluctuates and becomes scattered over edges and voids. Eventually, the evaporation condition becomes non-uniform and the deposition rate fluctuates. A schematic diagram showing the distribution of evaporation for different sources is shown in Figure 4.5.
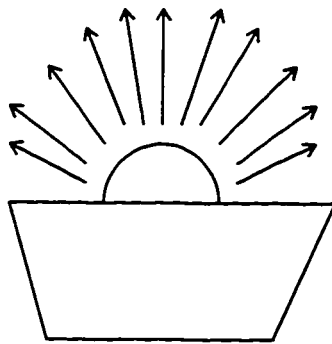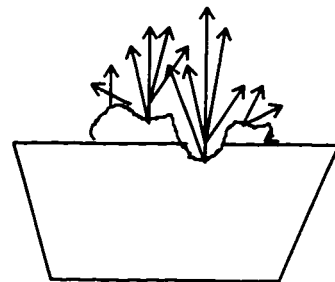
A uniformly distributed evaporation   A non-uniformly distributed evaporation

Figure 4.5: A schematic diagram showing the distribution of evaporation.

The deposition rate also depends on the condition of the electron beam, whether it is well focused, or diffused, or whether the sweep control is on or off. This is because the power density is varied in different conditions. Power density is maximized for a well-focused beam. If the sweep control is on, the beam will sweep over the entire area of the evaporant, and the power density and deposition rate will decrease. From Figure 4.3, the sweep control was turned on and the deposition rates for 4.2 kW were observed to be much lower than those that were obtained previously. One reason was the shape of the molybdenum source, and the other reason was the decrease in power density due to the sweep control.

4.2.3 How to make a dome-shaped evaporant source

To prepare a good evaporant source, the beam current must be turned on very slowly; the pressure of the system must be checked to make sure there is no sudden increase in pressure due to outgasing during melting of the molybdenum materials. Different forms of molybdenum materials were used to prepare the evaporant source. They included molybdenum granules (0.5 x 0.5 mm), big cylindrical pellets (6 x12 mm), and small cylindrical pellets (6 x 6 mm).

Molybdenum granules were not suitable to form a dome-shaped source due to their extremely small size. A large amount of granules must be used and this created many problems. It was very hard to maintain them on the cone surface. Moreover, the large surface area of granules permitted the absorption of water and other contaminants which were released upon heating, causing localized spitting from the evaporant source. Furthermore, it was very inefficient to melt them together to form a densely packed evaporant source. There was much outgasing and spitting during deposition, which may be due to trapped air pockets. A very irregular surface was formed instead of a smooth dome-shaped source.

For the big molybdenum pellets, two pellets were used and it took a long time to melt them due to their large size. There was much outgasing during melting because a higher electron beam current was required. Since the pellets were so big, heat energy supplied to them during melting was not evenly distributed, which caused local heating and spitting. It was extremely difficult to melt the pellets completely. Due to the incomplete melting, the source was not totally in contact with the evaporant cone. This

resulted in localized heat conduction and heat dissipation during deposition. As a consequence, heat energy was not uniformly distributed which gave rise to fluctuations in the deposition rate. Finally, a source with an irregular shape was obtained instead of a dome-shaped source.

The small molybdenum pellets were the best choice for preparing a dome-shaped source. Six small pellets were used. Melting was very efficient due to their smaller size. It was very easy to melt them completely, and the beam current used was around 0.25A. There was not much outgasing during melting. They could be combined easily by moving the electron beam over the melted pellets. As a consequence, a dome-shaped evaporant source was formed due to the surface tension.

4.2.4 Gettering effect of residual gas from molybdenum vapors

Depositions performed at higher deposition rates usually had lower residual gas pressures than those done at lower deposition rates. This was due to the gettering effect of molybdenum evaporant atoms, which could combine with residual gases during evaporation. Therefore, the advantage of increasing the deposition rate of molybdenum not only improved the deposition time, but it also helped to decrease the residual gas pressure, which in turn improved the film purity.

Chapter 5: Cone Formation by Electron Beam Evaporation

5.1 Introduction

The objective of this phase of the work was to form Mo cones by using electron

beam evaporation through a shadow mask. Provided that Mo can be deposited at the

periphery of the holes of the shadow mask and gradually close them, complete cones

should be formed. The characteristics of the molybdenum thin film, such as its

microstructure and its internal stress, were studied as well.

An evaporant source with a dome shape was prepared for this experiment. Instead

of using a bare silicon wafer as the substrate, a shadow mask with dimensions of

0.6" x 0.8" was used. The shadow mask is a silicon substrate with a layer of SiO_2 on top,

in which many cylindrical holes have been etched down to the silicon substrate. The

shadow mask was attached on a second silicon wafer, so that a step region would be

created after deposition. This step region was required for the film thickness

measurement. A top view of the shadow mask with magnification 1000X is shown in

Figure 5.1. A schematic diagram showing the cross-sectional view of the shadow mask

substrate are shown in Figure 5.2a; an SEM micrograph cross-section is shown in

Figure 5.2b.

Input power used for the deposition was 3.8 kW. A thermocouple was

used to measure the substrate temperature during deposition. After deposition, an optical

microscope was used to examine the deposits inside the cavities.

The shadow mask was cleaved to get a vertical cross-section. The specimen was
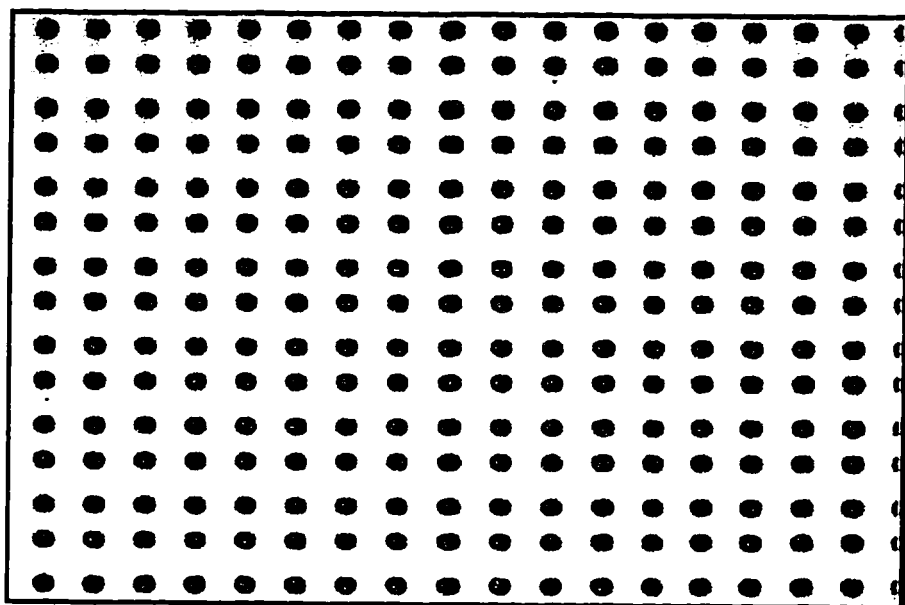
Figure 5.1: An optical photograph showing the top view of the shadow mask before deposition with magnification 1000X.

→ SiO$_2$

→ Silicon
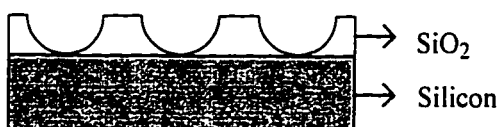
Figure 5.2a: A schematic diagram showing the cross-sectional view of the shadow mask.

then mounted onto a specimen holder, and the area of interest was cross-sectioned by grinding and polishing using a glass wheel. After the specimen was polished, it was cleaned using deionized water. A Hitachi-520 scanning electron microscope was used to examine the cross-section of the shadow mask at different angles to verify whether there was any cone formation inside the hole cavities.

69

Figure 5.2b: A SEM micrograph showing a cross-sectional view
of the shadow mask before deposition. (X45K)

5.2 Results and Discussion

The molybdenum thin film thickness was found to be 1.08 ± 0.01 µm after a deposition time of 8 minutes. The deposition rate was calculated to be 22.5 ± 3 Å/s which is very close to the experiments described in Chapter 4.

Figure 5.3 shows an optical micrograph of the top view of the shadow mask after deposition. It was observed that the deposits protruded from the substrate. Figure 5.4 shows a SEM micrograph of the top view of the shadow mask. It was found that even though the holes were not completely closed, some molybdenum was deposited at the periphery of the holes. Figure 5.5 shows a higher magnification view of the periphery of

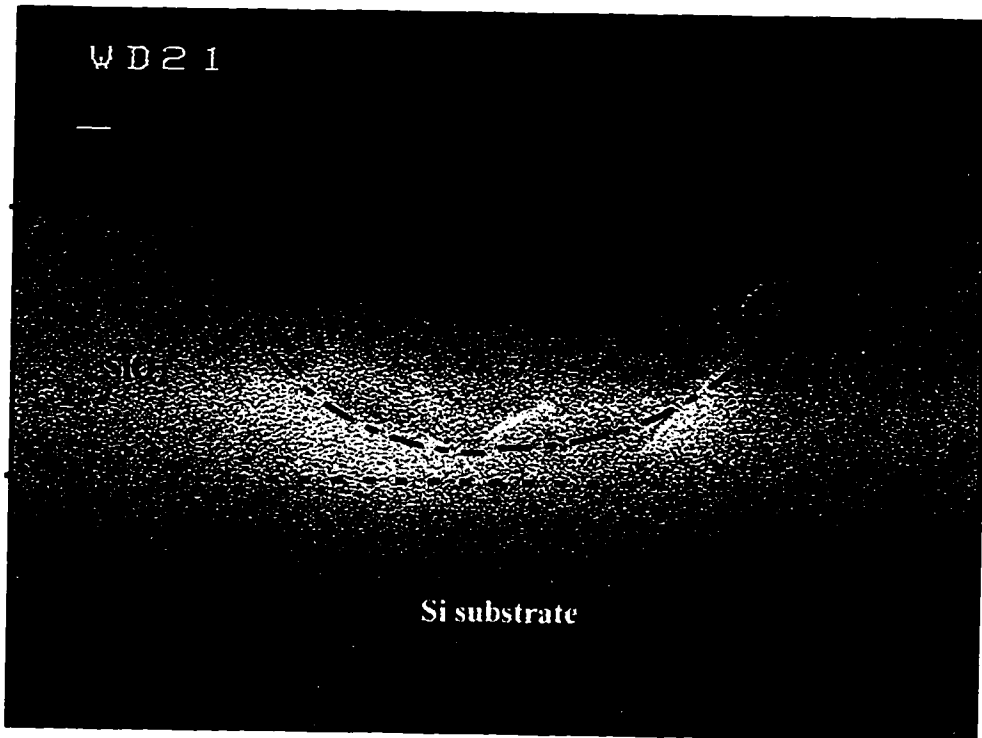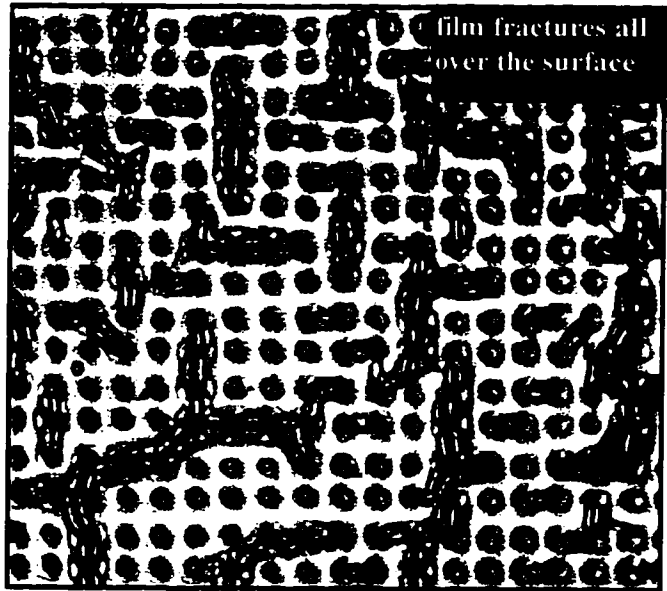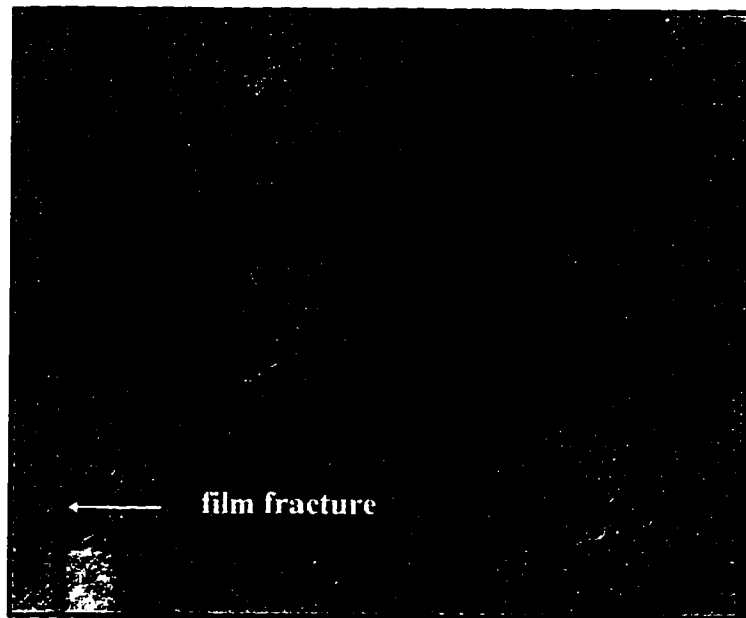Figure 5.3: A optical photograph showing the top view of the shadow mask after deposition. (X1000)

Figure 5.4: A SEM micrograph showing the top view of the shadow mask after deposition. (X10K)

71

a hole. Layers of molybdenum grains are clearly seen. XRF was used to confirm that there was some molybdenum deposited inside the hole.

From the SEM micrographs shown in Figure 5.6, a cross-section of the cavity can be clearly seen. A portion of the cone (i.e. the base of the cone) was observed inside the cavity. There was an initial formation of cones. From the profile of the deposited Mo, it is believed that a complete cone would be formed if enough molybdenum was deposited such that the hole was completely closed.

The thermocouple reading during deposition was 69 to 72 °C. At this temperature, the crystal structure should be a B.C.C. polycrystalline structure.[24] The SEM micrographs indicate that the Mo films were composed of columnar grains.

Finally, some film fractures were found on the shadow mask, seen in Figure 5.3. These were due to intrinsic stresses developed as a result of the difference in the coefficients of thermal expansion between molybdenum (Mo) and silicon dioxide (SiO_2). As the film and substrate cooled down after deposition, the Mo film would tend to contract more than the substrate, placing the Mo film in tensile stress. If the tensile stress was high enough to exceed the strength of the film, the film would fracture. This explains why some film fractures were observed on the shadow mask.

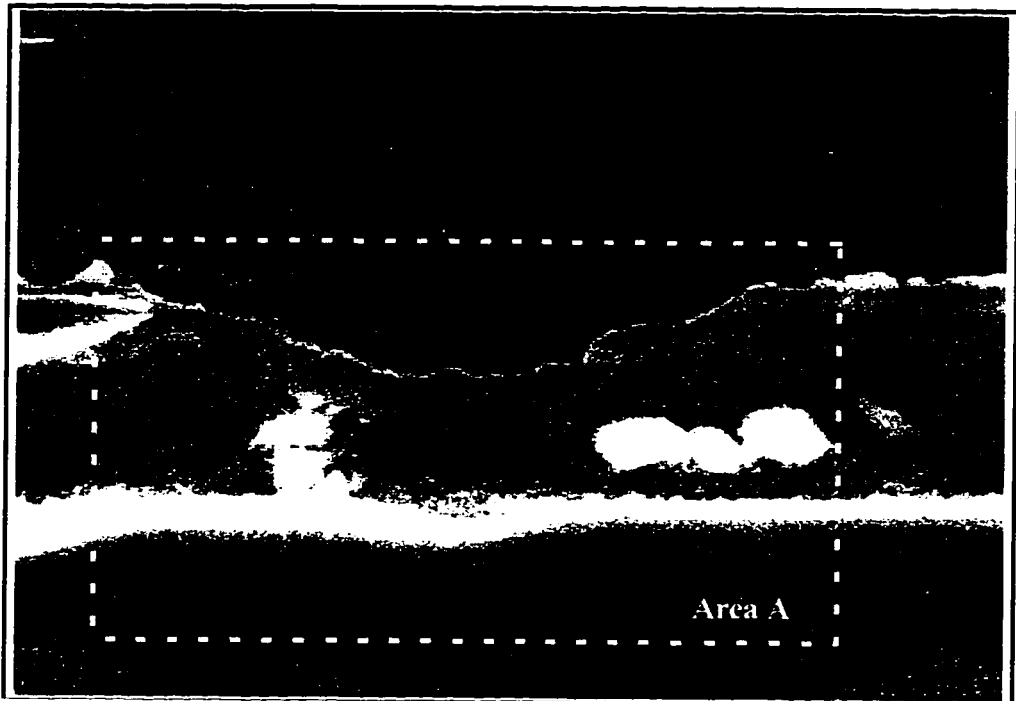Figure 5.5: A higher magnification of the periphery of a hole. (X80K)

Figure 5.6a: A SEM micrograph showing a cross-sectional view
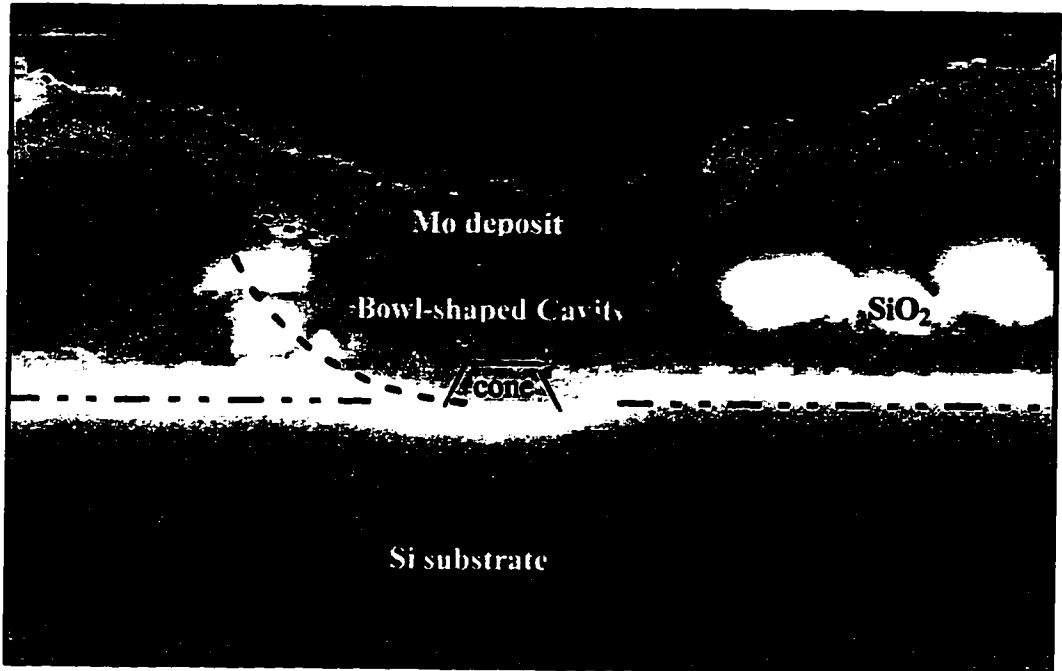of the shadow mask after deposition. (X2000)

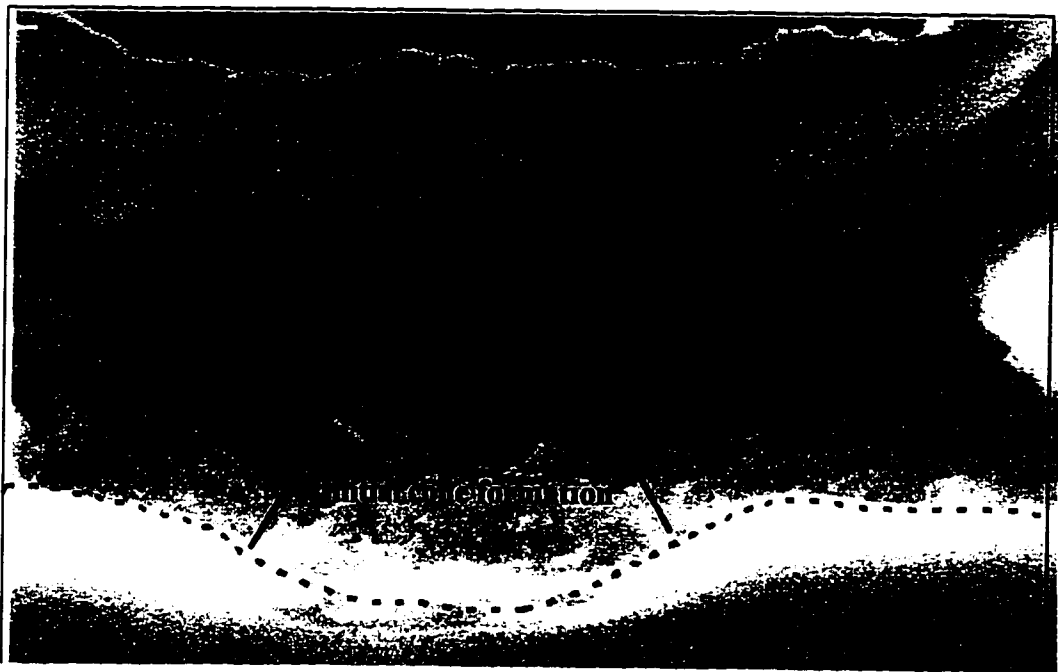Figure 5.6b: A magnification of area A from Figure 5.6a.

Figure 5.6c: A SEM micrograph showing the profile of the
molybdenum cone initial formation. (X 7000)

Chapter 6: Simulation of Thin Film Deposition

6.1 Introduction

This chapter discusses the existing simulation techniques and their suitability for simulating thin film growth. The goal of simulation is to provide a useful depiction of the resultant films, and to assist fundamental understanding of the process at a level not possible through experiments. However, since abstractions and approximations must be made to develop a workable model, it is not guaranteed that simulation results will accurately reflect reality. Therefore, simulation can supplement and complement experimentation, but cannot completely replace it.

The best computing platform for simulation is probably an engineering work-station, since it represents an acceptable compromise between cost and performance.

One common approximation made by many thin film deposition simulation models is to reduce the problem from three to two dimensions. This reduces both the computational and the memory requirements of the simulations, since only $N^{2/3}$ rather than N data elements need to be considered. However, this approximation is only valid when there is a symmetry which reduces the dimension of the problem. This would be the case for deposition over long features of constant cross-section, such as trenches or steps; or features which are cylindrically symmetric, such as round via. In the case of this thesis, cylindrically symmetric cavities allow an accurate 2D simulation.

6.2 Types of models

There are several types of simulation techniques. Types of models include molecular dynamics, atomistic models, string algorithms, continuum models, and ballistic deposition.[25] Feature resolution and simulation dimension for the film growth models are shown in Figure 6.1. The SIMBAD simulation program,[19] which uses a ballistic deposition model, was used in this thesis. A brief description of each type of the models is described below.

6.2.1 Molecular dynamics

Molecular dynamics are either two or three dimensional molecular models. They are mainly used to compute the forces between all combinations of interacting atoms and solve the resulting equations of motion. These models provide a very detailed approach to model inter-atomic processes such as recrystallization, epitaxy, and stress generation. The positions and velocities of each of the atoms must be calculated for each time step and stored in memory. These enormous computational requirements seriously limit the widespread application of molecular dynamics simulation as process development tools.

6.2.2 Atomistic models

Atomistic models are also called atomistic Monte Carlo simulations. They are similar to molecular dynamics models except that they assume a greater degree of independence between atoms and make some assumptions about equilibrium conditions. Nevertheless, a very large number of atoms are still required for calculations. Therefore,
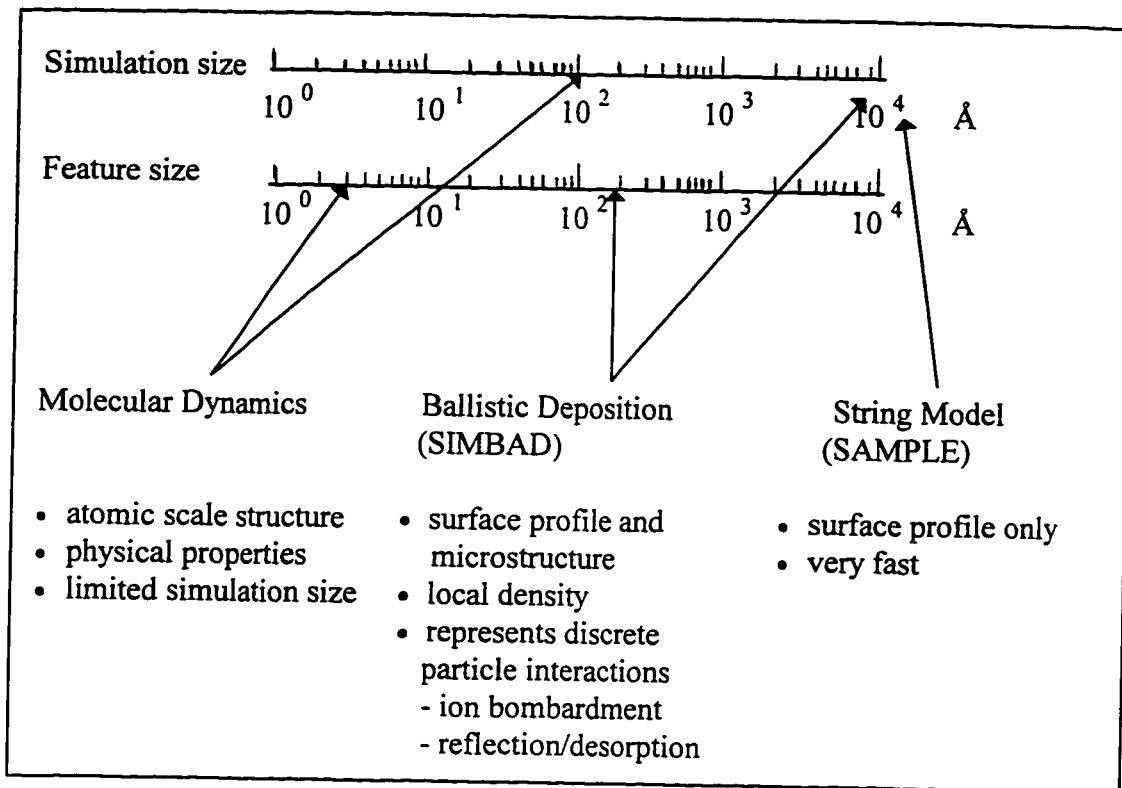
Figure 6.1: Feature resolution and simulation dimension for different film growth models.[26]

even though they can provide detailed microstructural information, the necessary

computing requirements effectively limit their application in process development

simulation.

6.2.3 String algorithms

String algorithm models include SAMPLE or SPEEDIE.[25] String models

represent only the surface of the film at relatively coarse resolution and in only

two dimensions. Therefore, these models are very practical to implement on current

computers. An example of a SAMPLE depiction of a film deposited over a via, with

surface profiles from various stages of growth is shown in Figure 6.2.
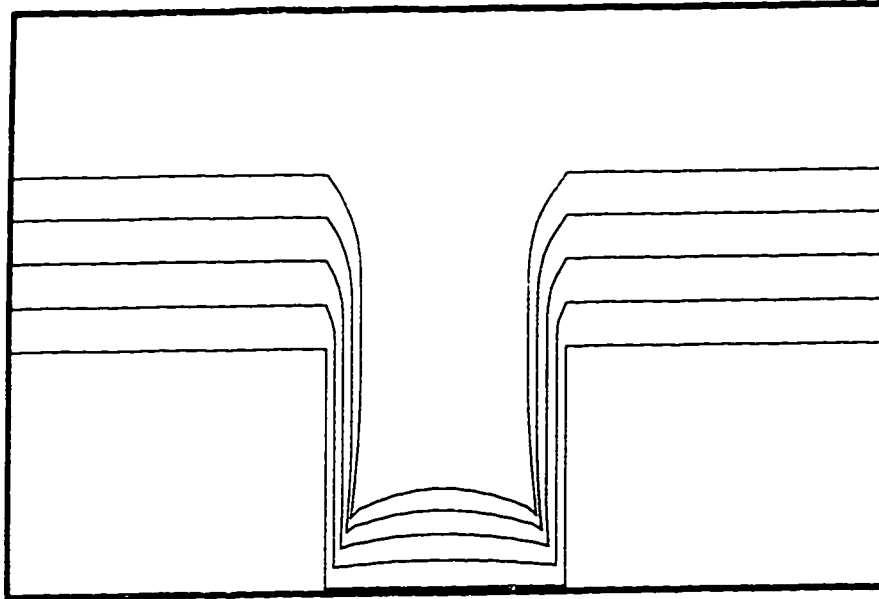
Figure 6.2: SAMPLE depiction of a film deposited over a via.[25]

The film surface is modeled in cross-section as a continuous line composed of line

segments, which are called strings. The calculation considers a series of points each

representing the center of a segment. For deposition, the position of each point evolves

according to a calculation of the flux reaching that segment. Only the surface profile or

step coverage is determined. Due to the simplicity of the string algorithm models, these

simulations can execute very quickly. Recently, the string algorithm models [25,26] have

been extended to a full three dimensional model to increase its applicability. However,

these models take the assumption that the film is homogenous and hence, cannot provide

information about the internal microstructure.

6.2.4 Continuum models

Similar to string algorithms, continuum models[25,26] represent only the film surface but at a higher level of resolution. In general, these models calculate surface evolution based on conservation of material from deposition and surface diffusion. Deposition conditions are controlled by defining equation constants and an incident flux distribution. Continuum models give information about the columnar microstructure in two dimensions. The execution can be very fast and efficient. However, significant approximations are usually required to make mathematical solutions tractable.

6.2.5 Ballistic deposition

Ballistic deposition models[25,26] are similar to the atomistic Monte Carlo models except that to make the execution time and memory requirements reasonable, they deal with much larger sized abstract particles which correspond to chunks of film material. These particles represent a statistical average of many atoms, each with similar trajectories and energies. The sizes of the particles chosen are much smaller than the microstructural features they are supposed to illustrate, but are large enough such that sufficiently few particles are needed to keep the simulation times practical. Ballistic deposition programs simulate thin film growth through the random irreversible deposition of hard two-dimensional discs or three-dimensional spheres launched with linear trajectories towards a surface. The spheres are assumed to travel along straight parallel lines until contact is made either with the surface or with previously deposited spheres. Such models have been widely used[25] to simulate thin film growth by physical

vapor deposition and have helped to clarify the processes involved in microstructure formation.

6.3 SIMBAD - Simulation of thin film growth

The foundation of the SIMBAD (SIMulation by Ballistic Deposition) model[25-28] was based on the original ballistic deposition model, which was developed by Professor M. Brett at the University of Alberta. The primary purpose of the program is to provide a surface profile of the film at any point during its processing (i.e. step coverage) as well as a microstructural depiction of the thin film, such as its columnar structure, presence of voids and surface roughness. SIMBAD is a two dimensional simulator which is capable of providing cross-sectional depiction in reasonable times on a typical engineering workstation. SIMBAD can be used in a variety of different deposition and etching processes, including evaporation, sputtering, bias sputtering, CVD, plasma etching and sputter etching.

6.3.1 Basic mechanism of the SIMBAD thin film growth simulation

SIMBAD can be used in a variety of different depositions and processes. Since the deposition technique used in this thesis was electron beam evaporation, emphasis of the following sections will be on the electron beam evaporation. A more detailed description for other models such as sputtering, chemical vapor deposition, and etching, can be found in Reference 25.

To understand the basic mechanism of the SIMBAD simulation, we need to know

what key factors determine the step coverage and columnar microstructure of thin films. The step coverage and microstructure of a thin film are determined by shadowing in the deposited film, surface diffusion, sticking coefficients and the melting point of the depositing material. For models other than electron beam evaporation, deposition parameters such as ion bombardment and resputtering should also be considered.

In the SIMBAD algorithm, the film is represented by the aggregation of 10^4 to 10^5 identical hard discs. These discs represent statistically averaged physical particles (typically 1000 atoms per disc) such as atoms, molecules, or ions which have similar trajectories and impact points. Shadowing and surface diffusion, which primarily determine film columnar microstructure and step coverage, are incorporated into SIMBAD in a two-stage algorithm.

6.3.1.1 Shadowing effect

Shadowing is accounted for in the first stage of the algorithm. In this stage of the simulation, the discs are independently launched from random locations just above the substrate. Under low pressure deposition, the exact distance above is not important, provided that it is much less than the mean free path for collisions between the depositing flux and the ambient gas. The shadowing effect of the discs by the growing film is strongly dependent on the angular distribution of the atomic depositing flux, which is dependent on the deposition geometry, source material's properties, and gas pressure. Each disc follows a straight line trajectory until it strikes the substrate or a previously deposited film disc (i.e. the growing film).[25,26] This ballistic stage of the algorithm

81

intrinsically incorporates the effects of shadowing, both by the substrate topography and by the neighboring film regions. An example of the influence of shadowing effect on the surface profile and step coverage is shown in Figure 6.3. Shadowing of the incoming flux by the step causes a break in the film continuity on the right side of the step.
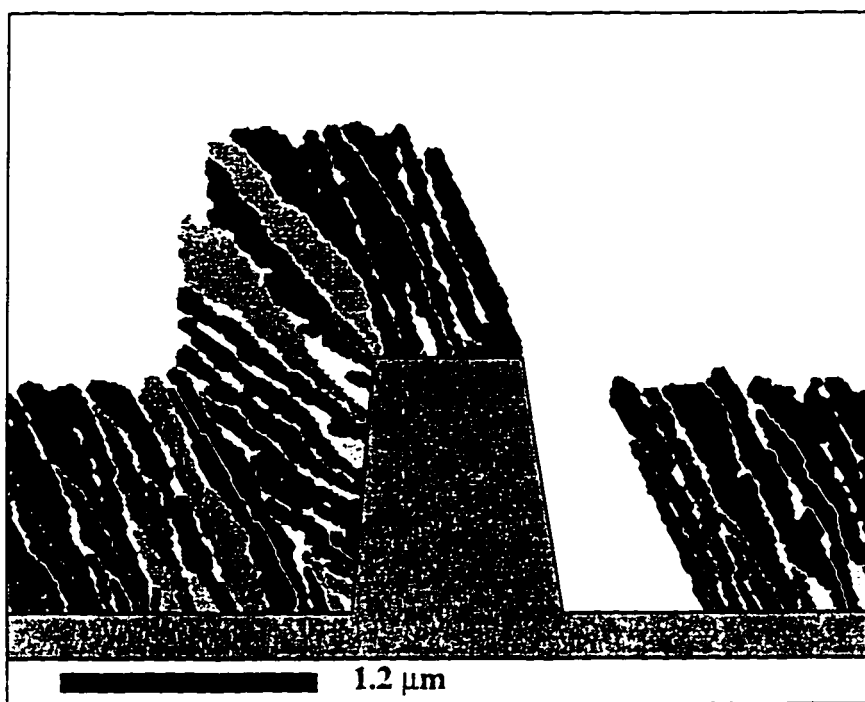
Figure 6.3: An example showing the shadowing effect on the step coverage.[28]

6.3.1.2 Surface diffusion

Surface diffusion is accounted for in the second stage of the algorithm.[25] At the point of contact with the growing film, the disc is allowed to diffuse over the film surface. The range of this diffusion is controlled by the surface diffusion length, which is determined by the deposition material and the film temperature. During diffusion, the

disc moves on the film surface in both directions up to a limited range to reach a position

with maximum contact with other film discs. If several sites of equal coordinate numbers

are located, the one closest to the initial impact point is chosen. The minimization of

surface curvature and energy is considered to be the most important effect of surface

diffusion, which is equivalent to surface tension minimization.[25,26] This relaxation

process tends to reduce both local concentration gradients and local film curvature in

order to reduce the surface energy. Qualitatively, they are the desired effects of short

range surface diffusion corresponding to low and moderate substrate temperature. A

schematic description of the SIMBAD algorithm is shown in Figure 6.4.
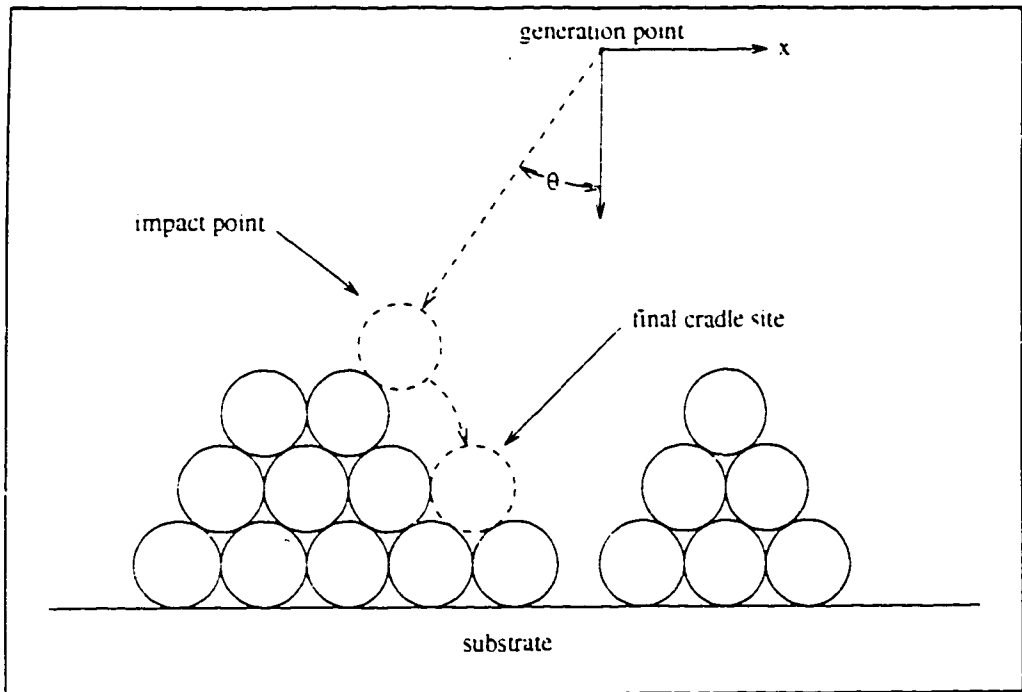
Figure 6.4: A schematic description of the SIMBAD model, where θ is the deposition angle of the disc. It diffuses from its impact point to the site which maximizes coordination with other discs within a maximum searching range.[25]

In general, for a simulation with no diffusion, the columnar structure is very

porous and is composed of tree-like chains of discs. As soon as diffusion is allowed, the

structure becomes much more dense and columnar, beginning to resemble a real film.[26]

The change in columnar structure with increasing diffusion length is shown in

Figure 6.5.
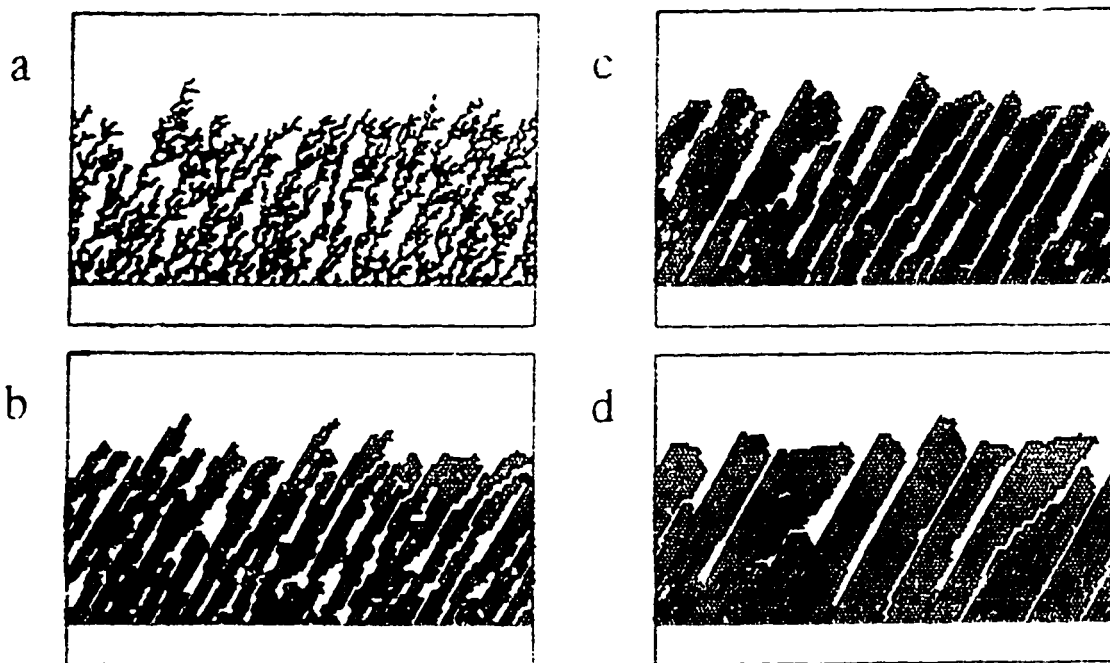
Figure 6.5: Change in column structure with increasing diffusion length. Deposition angle was 50°. Diffusion lengths are a) 0 disc diameters, b) 1 diameter, c) 2 diameters, d) 4 diameters.[26]

6.3.1.2.1 Diffusion length

Diffusion length is a very important parameter that controls the film

microstructure. When atoms are physisorbed (adatom) on the surface, they are in a

metastable state since the bond is the weak van der Waals force. These atoms are very

84

mobile and will seek the most suitable "cradle site," i.e., the site where the surface

curvature would be minimal, by searching a limited number of neighboring sites. The

extent of this search is characterized by the surface diffusion length.[27]

In reality, the adatoms are in constant motion, and will encounter a periodic

surface potential. In order to "jump over the potential barrier," i.e., diffuse to the

neighboring site, two conditions must be met. First, the site must be empty. Fortunately,

we are dealing with the surface diffusion, and this condition is not a problem. Second,

the adatom must have enough energy to surpass the barrier. The more energy the adatom

has, the more potential cradle sites it will explore, and the greater the effect the surface

diffusion will have.

Increasing the average adatom energy and hence the surface diffusion length is

possible by either heating the substrate, or keeping the working gas pressure low, so that

the arriving adatoms can retain a maximum of their original kinetic energy.

The relationship between the diffusion length and the substrate temperature can

be expressed using the following formula.[28]

$$D = D_0 e^{-Q_s/kT} \tag{6.1}$$

where D is the surface diffusivity, D_0 is a constant and Q_s is the activation energy for

surface diffusion. The average surface diffusion length (L) is related to the

diffusivity by

$$L = \sqrt{D\tau} \tag{6.2}$$

where τ is the mean lifetime for mobile surface atoms. This lifetime is limited by the

deposition rate, and by the presence of reactive gas species or defects and contaminants which can bind with the atom and fix its position. Combining these relations gives

$$L = \sqrt{D_o\tau}\ e^{-2.5Tm/T}$$

(6.3)

Unfortunately, since τ is dependent on system, material and process parameters, the prefactor $\sqrt{D_o\tau}$ is difficult to quantify. Calibration must be made for different systems, materials and process parameters.[28]

In SIMBAD simulation, the diffusion length is presented in terms of the diffusion length factor which has a value from 0.025 to 0.1.[28] The influence of the diffusion length on the simulation model was investigated and will be discussed in Chapter 7.

6.3.1.2.2 Sticking coefficient

There are other things that may happen during the process of surface diffusion. An adatom may be buried by the depositing flux prior to finding the most appropriate site. This will shorten its surface diffusion length, and may cause a crystal imperfection. On the other hand, an incident adatom can be emitted from the growing film, and subsequently be deposited at another part of the growing film. If this happens, the material is said to have a low sticking coefficient.[28] If the incoming adatom flux never re-emits from the growing film and instead always adheres to the growing film, the sticking coefficient is said to be unity.

The influence of the sticking coefficient on the simulation model was investigated and will be discussed in Chapter 7.

6.3.3. 2 Principle of Operation of SIMBAD

As mentioned before, in the SIMBAD thin film growth simulation, the shadowing

effect primarily determines film columnar microstructure. However, the self-shadowing

of the arriving flux by the growing film is strongly dependent on the angular distribution

of the atomic flux; and the shadowing effect is incorporated by the substrate topography

and by the neighboring regions. Therefore, to run the SIMBAD simulation, inputs

include not only the surface diffusion length, sticking coefficient, and film thickness, but

also the initial topography profile, and the angular distribution of the incident particles.

The output of the simulation is a film profile composed of the deposited discs. An

example of the output film cross-section showing column structure is shown in

Figure 6.6.

6.3.3.3 SIMBAD thin film growth input parameters

To simulate simple thin film growth, after the initial topography is drawn, it is

first necessary to set the simulation parameter **mode**, which represents the deposition

method such as sputtering, evaporation, CVD, plasma or ion etching. In addition, an

important model parameter is the **resolution.** It determines the size of the discs relative

to the substrate topography. The higher the resolution, the greater the number of discs

that form the film, resulting in a smoother, more realistic film. However, memory and

execution time scale approximately as the square of the resolution.[28] In addition, flux

parameters which determine the angular distribution of the incoming depositing flux are

very important in determining the resultant film growth. Based on the setting of the
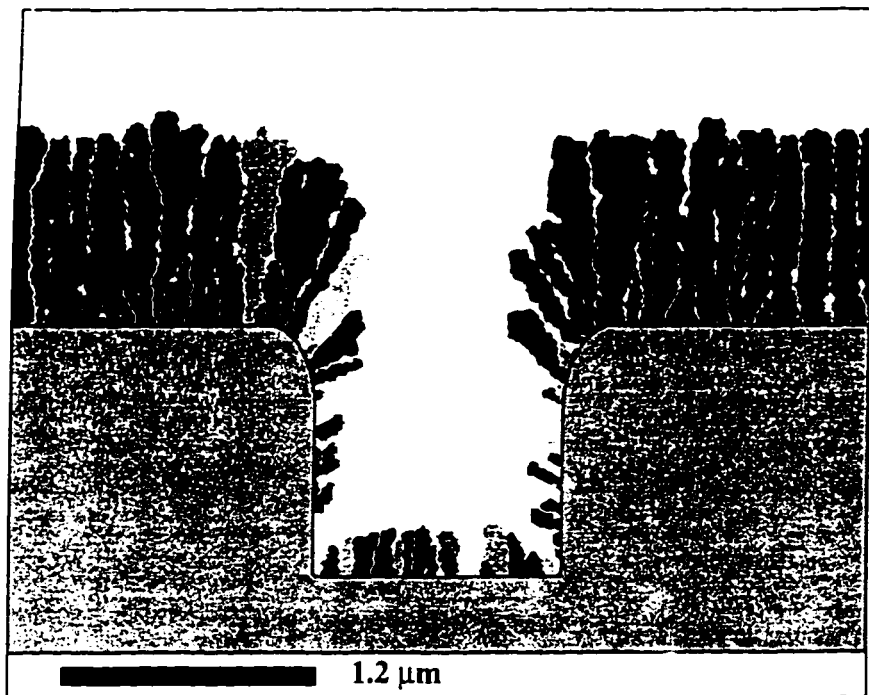
Figure 6.6: A film cross-section showing column structure.[28]

parameters **dep_angle** and **dep_spread**, the angular distribution is determined. The

parameter **dep_angle** sets the angle about which the angular distribution is centered:

while **dep_spread** determines the width of the angular deposition. If the mode is

sputtering, either a compressed cosine is used. and this parameter sets the width of the

compressed cosine: or a user defined angular distribution is read from the file specified by

the **angle_file**. Such angular distribution files are produced by a simulator called

SIMSPUD which models the transport of particles from generation at the target to

deposition at the substrate. Details of how SIMSPUD works can be found in

Reference 28. If the mode is evaporation, a uniform distribution with a width of

dep_spread is used. In electron beam evaporation. since the source is far away from and

directly above the wafer, the angular spread is negligible and the average angle of deposition is equal to zero.

Finally, growth parameters such as **thickness** of the film to be added, diffusion length (**diff_length**) and sticking coefficient (**film_sticking**) of the adsorbed flux, are important input parameters.

A detailed description of each thin film growth input parameter is included in Appendix C; a tutorial demonstrating the procedure of running the SIMBAD simulation is included in Appendix D.

Chapter 7: SIMBAD Simulation Results

7.1 Introduction

A simulation program called SIMBAD was utilized to find out the relationship between the key growth factors and the cone shape and cone height. The input parameters used as variables in the SIMBAD simulations were angular spread, sticking coefficient and surface diffusion length. The cavity structure was varied and used as input for the topography files. The average angular spread and the angle of deposition were assumed to be zero.

7.2 Results and Discussion

7.2.1 Effect of sticking coefficient on the cone formation

The sticking coefficients were varied from 0.5 to 1. The simulation results for different sticking coefficients are shown in Table 7.1 and Figure 7.1 respectively.

Table 7.1: Cone heights for different sticking coefficients

Sticking coefficient	0.5	0.75	0.95	1
Cone height (μm)	0.9 ± 0.01	1.0 ± 0.01	1.2 ± 0.01	1.4 ± 0.01

It was found that increasing the sticking coefficient caused an increase in cone height. The column sizes were similar with different sticking coefficients. Increasing the sticking coefficient also caused a reduction in sidewall deposition, however, sidewall deposition is also dependent on the deposition conditions, such as residual gas pressure.
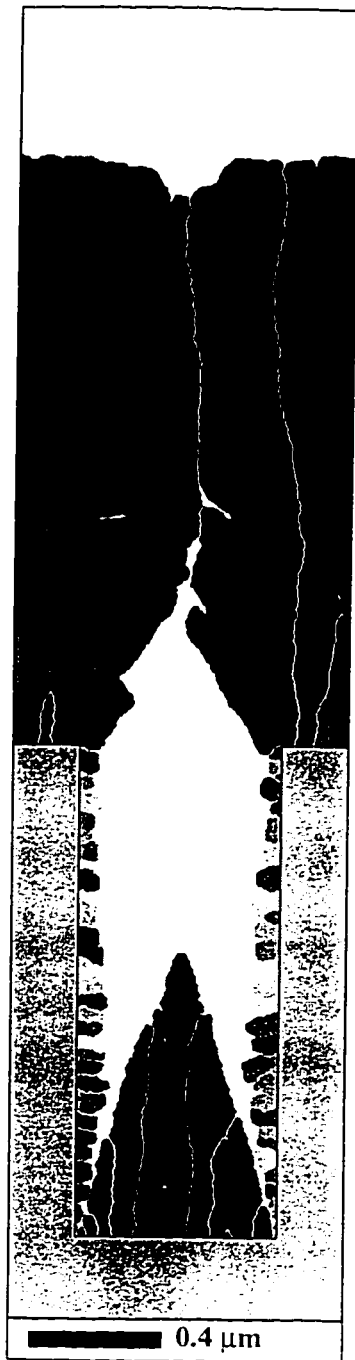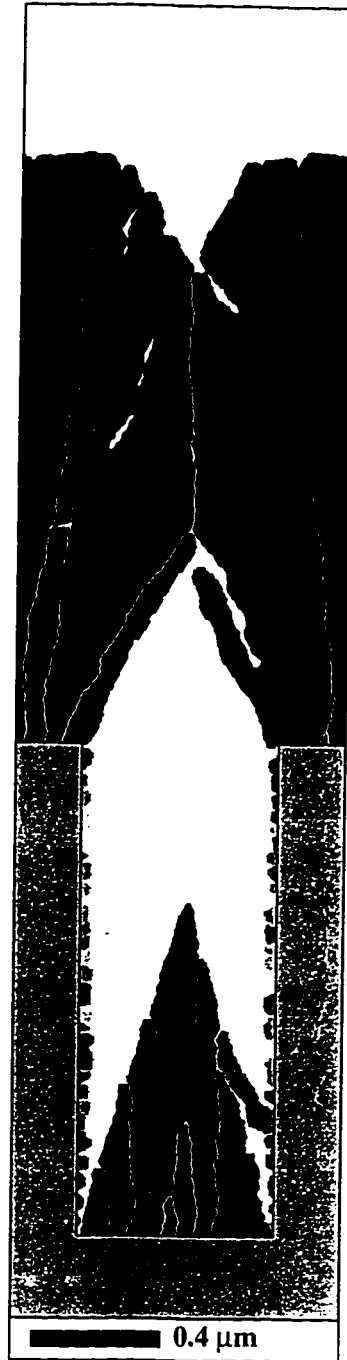
(a)   (b)

Figure 7.1: Simulation results for sticking coefficients of
(a) 0.5, (b) 0.75, (c) 0.95 and (d) 1.0.

(c)   (d)

92

Most refractory materials (such as molybdenum), have sticking coefficients close to unity.[28] A high sticking coefficient is desirable for cone formation.

7.2.2 Effect of diffusion length on the cone formation

The diffusion length factor varied from 0.025 to 0.10. The simulation results are shown in Table 7.2 and Figure 7.2 respectively.
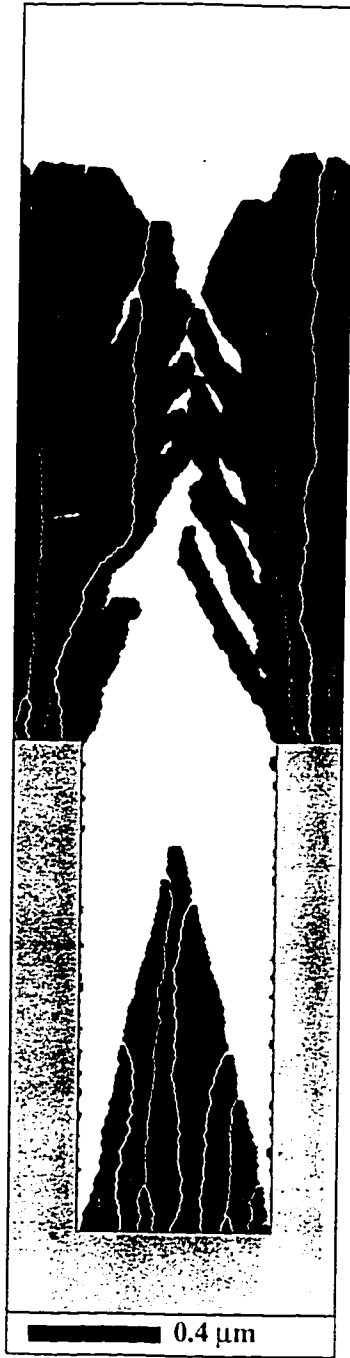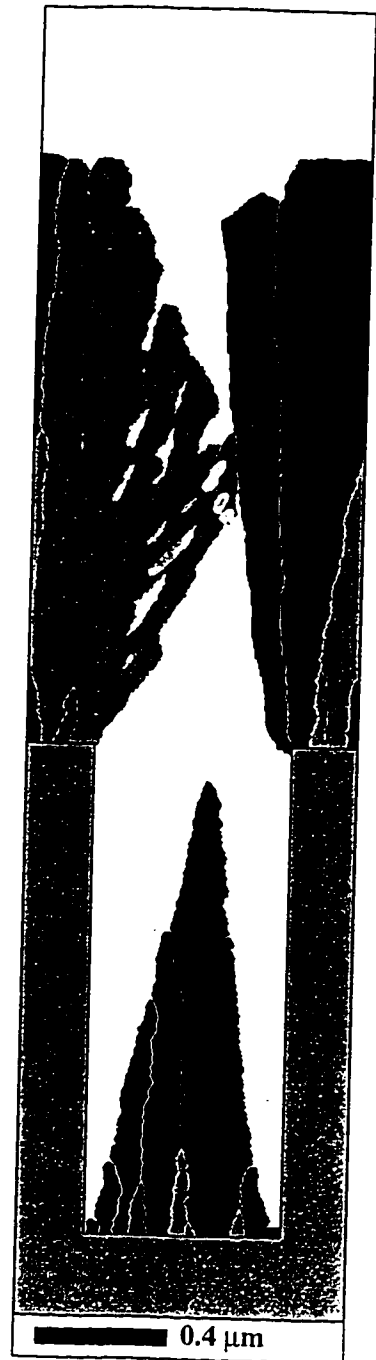
Table 7.2: Cone heights for different diffusion length factors.

Diffusion length factor	0.025	0.05	0.10
cone height (μm)	1.4 ± 0.01	1.7 ± 0.01	2.0 ± 0.01

It was found that increasing the diffusion length factor contributed to a higher cone height and a larger columnar structure. Figure 7.2(c) shows that when the diffusion length factor was 0.1, the cone shape was deformed and had a rounded head instead of having a sharp tip. Therefore, deposition with a long diffusion length was not desirable for the cone formation. This phenomenon may be explained by knowing that the minimization of surface curvature and energy is considered to be the most important effect of surface diffusion. When the discs make contact with the growing film, they have a tendency to find a site which will produce a film with curvature as low as possible. However, the range of this diffusion is controlled by the surface diffusion length factor. A longer diffusion length gives a better chance to find a site with the lowest surface curvature. Figure 7.2(c) shows that a very long diffusion length allows the discs to find a site with minimum surface curvature, forming a rounded head. Longer diffusion lengths

Figure 7.2: Simulation results for diffusion length factor of
(a) 0.025, (b) 0.05 and (c) 0.10.

94

resulted in larger columnar structures because they provided more opportunities for the growing film to minimize the surface energy.

As mentioned in Chapter 6, diffusion length is dependent on T/T_m of the material being deposited. In evaporation, the substrate temperature is usually very low. For example, the substrate temperature for the molybdenum electron evaporation in this thesis was only 72 °C, while the melting temperature of molybdenum is 2610 °C. This would indicate a low value of T/T_m factor, and thus a low value of diffusion length for molybdenum, which is desirable for the cone formation. Thus Figure 7.2(a) is the most realistic simulation for Mo cone formation.

7.2.3 Effect of angular spread on the cone formation.

The angular spread was varied from 0 to 10°. An example of the simulation results with 5° angular spread is shown in Figure 7.3. It was found that even when the angular spread was as small as 1°, there were some deposits on the sidewall. Thus, the angular spread of deposition should be about equal to zero for cone formation. This indicates that electron beam evaporation is a good choice, since the travel path of the evaporant is highly directional, the angular spread is low.

7.2.4 Effect of cavity structure

7.2.4.1 Cavity height

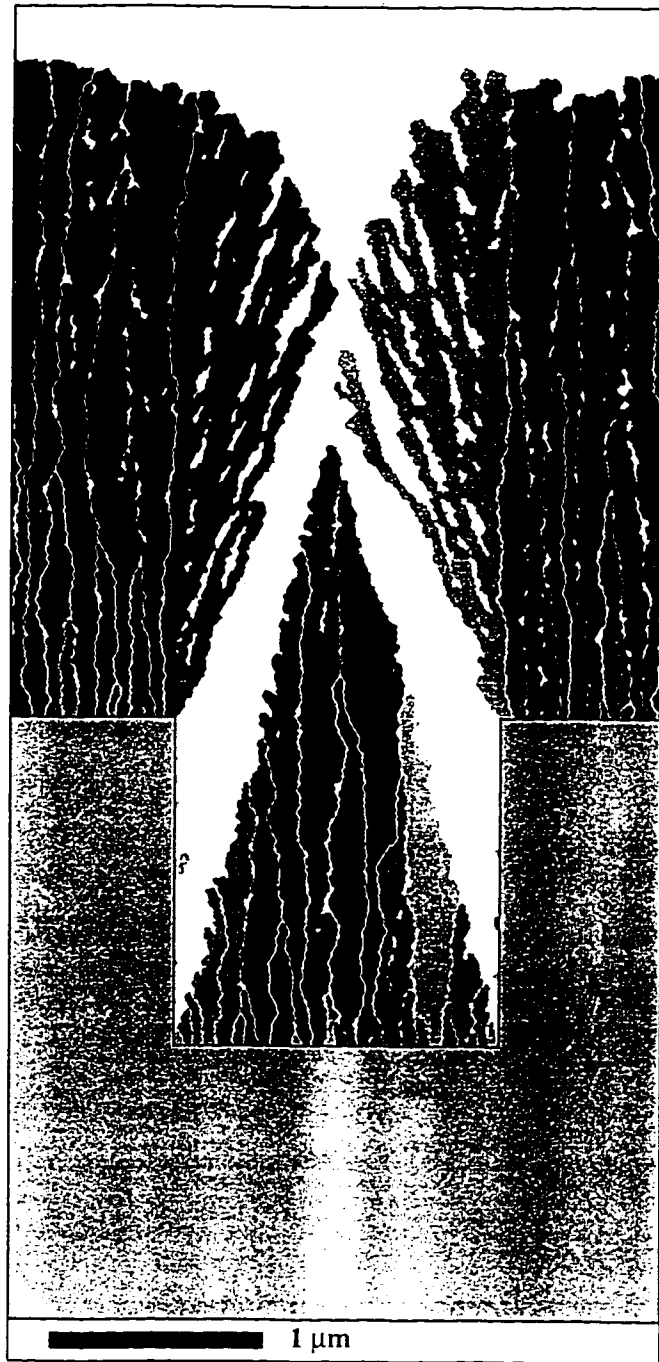To determine the effect of cavity structure on cone formation, the cavity heights

Figure 7.3: An example showing the effect of 5° angular spread on the cone formation.

were varied from 1.0 to 1.5 μm. The other input parameters were kept constant, using a sticking coefficient of 1, a diffusion length factor of 0.025, and a hole diameter of 0.6 μm. The heights and shapes of the cones for different cavity heights are shown in Table 7.3 and Figure 7.4 respectively.

Table 7.3: Cone heights for different cavity heights with same input parameters.

Cavity height (μm)	1	1.25	1.5
Cone height (μm)	1.4 ± 0.01	1.5 ± 0.01	1.4 ± 0.01
Protrusion amount (μm)	0.4	0.25	-0.1

It was found that the cone shape and cone height were almost independent of the cavity height; only the amount of protrusion was dependent on the cavity height. A lower cavity height results in more cone protrusion. The shape and columnar structure for these three simulations were almost identical. The cone shape and cone height are directly related to how the discs deposit into the cavity. As long as the discs drop into the cavity at normal incidence, there is no influence of the cavity height on the dropping discs. Therefore, the cone height and cone shape are independent of the cavity height.

7.2.4.2 Hole diameters

The hole diameter was varied from 0.4 to 0.8 μm in the next set of simulations. The other input parameters were kept constant at a sticking coefficient of 1, a diffusion length factor of 0.025, and a cavity height of 1.5 μm. The cone shape and the cone height for different hole diameters are shown in Table 7.4 and Figure 7.5 respectively.
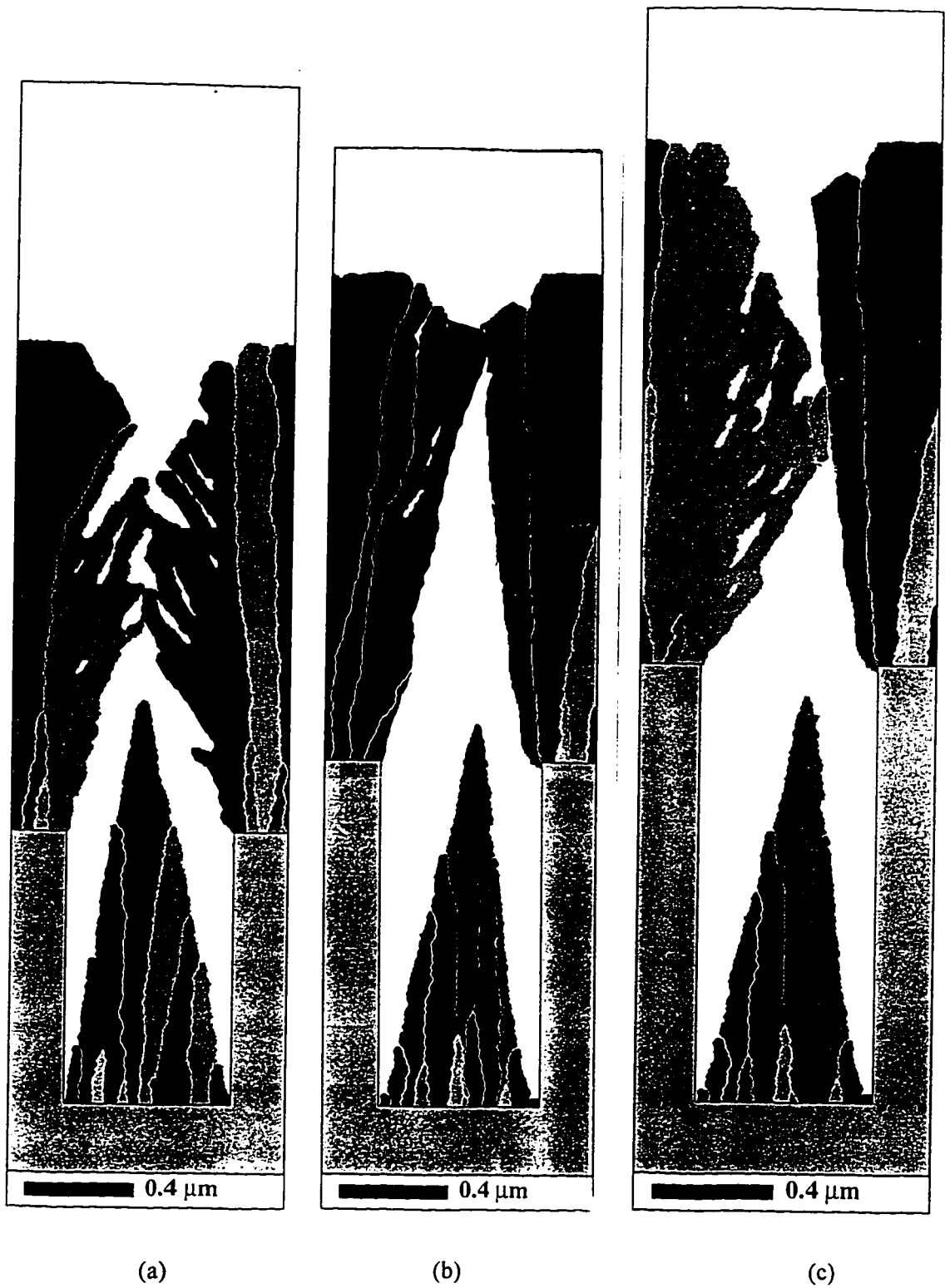
97

Figure 7.4: Simulation results for cavity heights of
(a) 1 μm, (b) 1.25μm and (c) 1.5 μm.

Table 7.4 Cone heights for different hole diameters

Hole diameter (μm)	0.4	0.6	0.8
Cone height (μm)	1.0 ± 0.01	1.5 ± 0.01	1.8 ± 0.01
Hole diameter : cone height	0.42	0.41	0.43

It was found that a larger hole diameter produced a higher cone, which proved the hypothesis that the larger the hole diameter, the longer the time required to close the hole, and thus the higher the cone will be. Moreover, it was found that the ratios of the hole diameter to the cone height for the three simulations were almost the same, about 0.42. This proved that the ratio of lateral growth to vertical growth is constant. Also, inspection of Figure 7.5 shows there was no influence of the hole diameter on the columnar structure.

7.2.4.3 Shapes and angles of undercut

Five different shapes and angles of undercut were used as input files for the substrate topography. A schematic diagram for these five substrate topography files is shown in Figure 7.6. The height and the base of the cavities are fixed to 1.5 μm and 0.6 μm respectively. The other input parameters were fixed at a sticking coefficient of 1, and a diffusion length factor of 0.025. Two simulations were made for each of the topographies. The results are tabulated in Table 7.5 and Figure 7.7 respectively.

Different angles and shapes of undercut gave different cone shapes and cone heights. It was found that the undercuts of simulation #1, 2, and 3 gave straight cones with repeatable results while # 4 and 5 were not reproducible. Simulations #1 and 2 gave

Figure 7.5: Simulation results for hole diameters of
(a) 0.4 μm, (b) 0.6 μm and (c) 0.8 μm

higher cones than #3.

| Simulation # 1 | Simulation # 2 | Simulation # 3 |

| Simulation # 4 | Simulation # 5 |
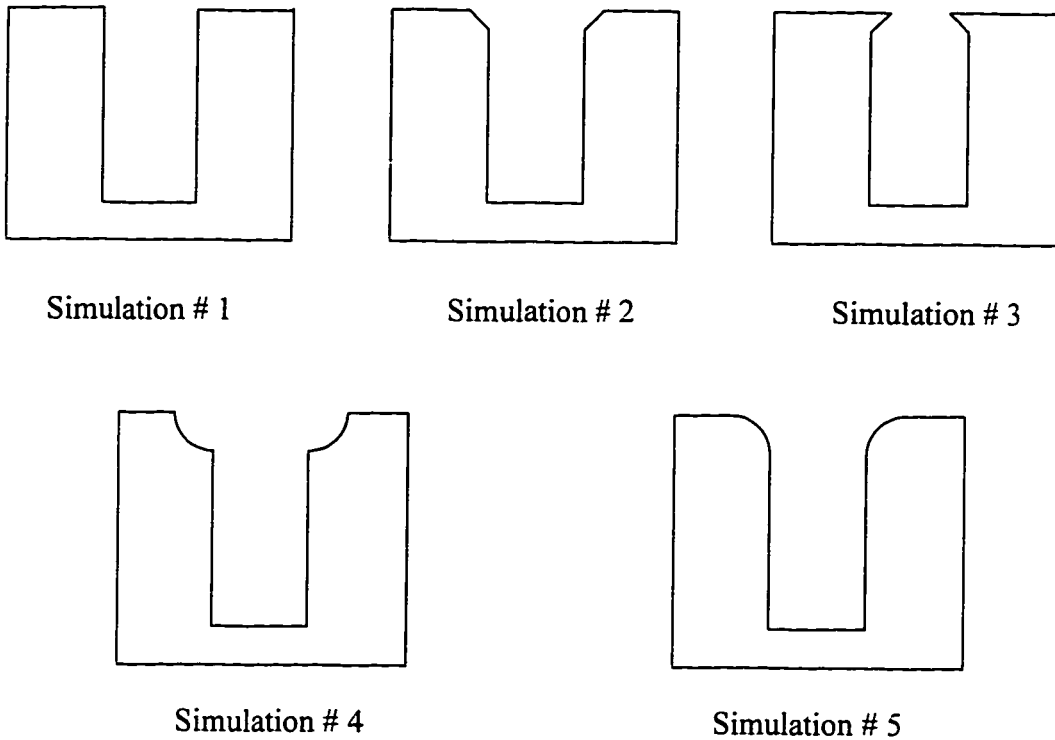
Figure 7.6: Five different shapes and angles of undercut.

Table 7.5: Cone heights for different shapes and angles of undercut.

Simulation #	1	2	3	4	5
Cone height (μm)	1.4 ± 0.01	1.6 ± 0.01	0.6 ± 0.01	0.9 ± 0.01	0.8 ± 0.01
	1.5 ± 0.01	1.6 ± 0.01	0.8 ± 0.01	1.1 ± 0.01	1.7 ± 0.01
Average	1.45 ± 0.01	1.6 ± 0.01	0.7 ± 0.01	1.0 ± 0.01	1.3 ± 0.01
cone shape	straight	straight	straight	tilt / straight	tilt / straight

It was also found that undercut with sharp edges such as # 1, 2 and 3 gave more repeatable results, whereas undercut with curved shapes gave non-reproducible results. This may be caused by different undercuts giving rise to different amounts of surface

101
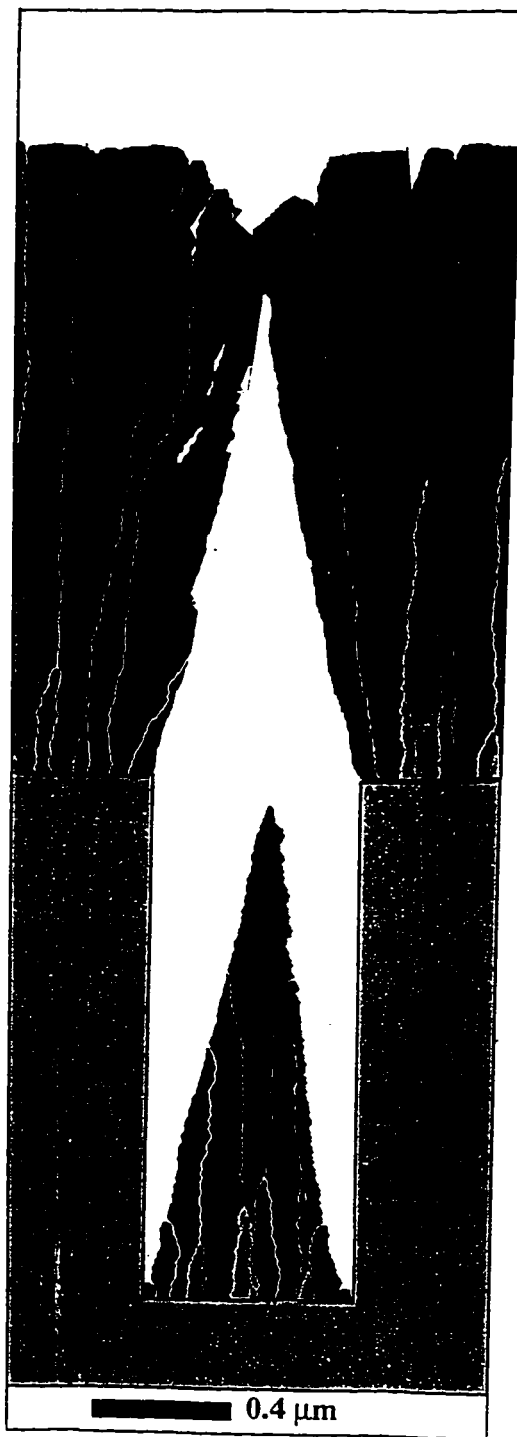
(a)   (b)

Figure 7.7: Simulation results for shapes and angles of undercut
of simulation (a) #1, (b) #2, (c) #3, (d) #4, (e) #5.

0.4 μm

(c)

(d)

(e)

104

diffusion and shadowing effects. These two factors determine the position and number of atoms growing on the periphery of the hole during deposition, which in turn affects the successive growth.

For example, when comparing simulation # 1, 2 and 3, simulation #3 gave the shortest cone, because it had a smaller opening, which closed faster than the others. On the other hand, simulation # 1 gave the highest cone, because it had a w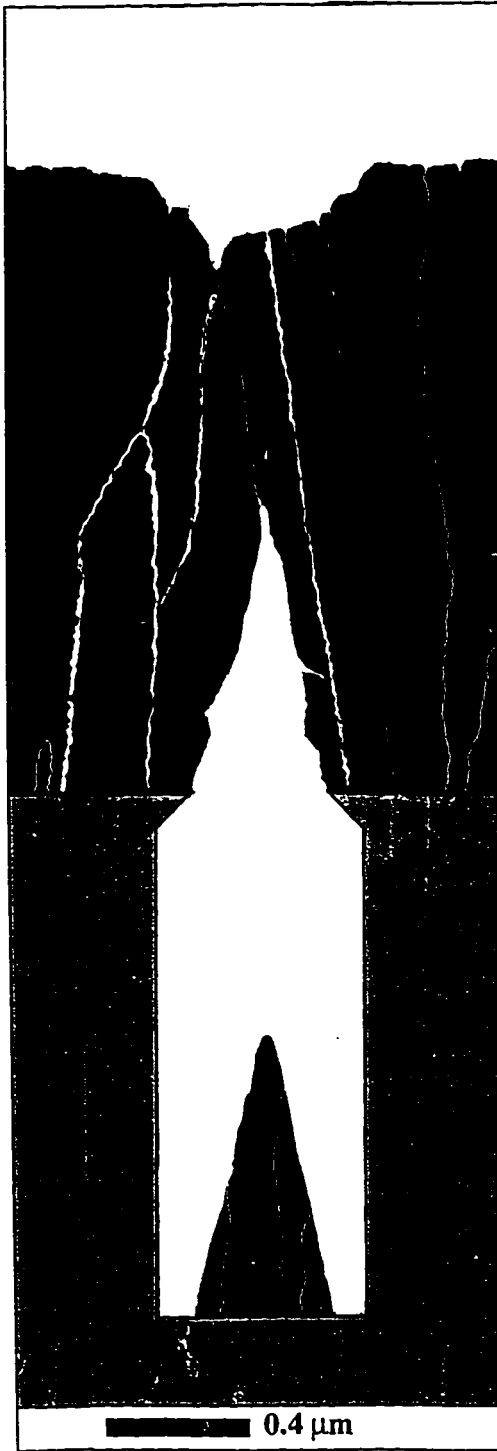ider opening. When the discs deposited on the surface of the periphery of the hole, they had very limited diffusion. Therefore, they did not have much mobility once they struck the periphery. Since the distribution of the evaporant and the undercuts are uniform over the whole periphery, lateral growth in all directions around the periphery should be uniform, and thus straight cones were formed.

On the other hand, simulations # 4 and 5 both have curve-shaped undercuts. Although the diffusion length factor was the same, the curved shape undercut may activate surface diffusion. A curved shape increases the tendency for the discs to reach the maximum limit of the diffusion length range. Thus, instead of staying at the site where they initially strike, the discs move over the film surface more easily to find the best site. Different discs may diffuse with different ranges of surface diffusion. Even though the undercuts are uniform along the whole periphery, the successive lateral growth may vary in different directions, depending on how far the discs moved to rearrange their position. Finally, instead of producing straight cones, tilted cones may form.

7.3 Summary

It was found that the important factors that affect the cone shape and cone height included the sticking coefficient, the diffusion length, and the cavity structure. Increasing the sticking coefficient caused an increase in cone height, and a reduction in sidewall deposition. The column sizes were similar with different sticking coefficients. Increasing the diffusion length factor contributed to a higher cone height and a larger columnar structure. When the diffusion length factor was 0.1, the cone shape was deformed and had a rounded head instead of having a sharp tip. It was also found that a larger hole diameter produced a higher cone. Finally, undercuts with sharp edges gave more repeatable results, and formed straight cones. On the other hand, undercuts with curved shapes gave unpredictable results, and titled cones could be formed.

Chapter 8: Conclusions and Recommendations for Future Work

8.1 Conclusions

This thesis describes the simulation and initial development of a process for thin film deposition of Spindt-type molybdenum field emitter cones using electron beam evaporation. Characterization of molybdenum thin film electron beam evaporation was done. It was found that for a dome-shaped molybdenum evaporant source, the deposition rate exponentially increases with the power. A constant and uniform evaporation rate was obtained. On the other hand, an irregular-shaped evaporant source resulted in poor deposition rates. Therefore, it is advised that the shape of the source should be checked before and after each deposition. It was found that the small molybdenum pellets (6 x 6 mm) were the most suitable to prepare a dome shaped source.

Initial efforts to form molybdenum cones by using electron beam evaporation through a shadow mask were partially successful. SEM and optical micrographs indicate that Mo was deposited inside the cavities, forming the base of a cone. Although complete cones were not formed due to the difficulty of maintaining long deposition times, it is believed that complete cones can be formed if enough molybdenum is deposited.

The SIMBAD simulation program was used to prove the hypothesis that the cone dimensions can be varied by varying the structure of the cavity and the growth factors. A higher sticking coefficient gave a higher cone, but also more sidewall deposition which is not desirable. A sticking coefficient of about 1 should be used. Longer diffusion lengths gave higher cones with larger columnar structure. A long diffusion length is not desirable

because the cone shape may be deformed. Thus a low sticking coefficient and low diffusion length is desirable.

It was found that the cone shape and cone height are independent of the cavity height; only the amount of protrusion depends on cavity height. It was also found that a larger hole diameter gave a higher cone height. Finally, it was found that undercuts with sharp edges gave more repeatable results, and formed straight cones. On the other hand, undercuts with curved shapes gave unpredictable results, and tilted cones could be formed.

Finally, the major problems encountered during the experimental stage of this thesis were from the difficulty of maintaining the electron beam evaporator system. Problems that were encountered from the system and the possible solutions can be found in the Appendix E.

8.2 Recommendations for further work

In this thesis, deposition thickness was measured by using a glass slide to create a step region. This is not an accurate method to measure the thickness, since an air gap may be trapped between the substrate and the glass slide. A more accurate measurement can be done by lithographically etching away a portion of the deposited thin film to create a step region.

More investigation into the role of substrate temperature on stress of the Mo film should be done, including determination of the optimum substrate temperature for molybdenum deposition.

From the profile of the initial cone formation, it is still too early to tell if a straight cone can be formed by using such a simple set up of the electron beam evaporation. Further investigation should be done to see if a straight cone can be formed, provided that a complete cone can be successfully made. The shadow mask used in this thesis was small enough so that the angle of incidence of molybdenum through all the holes is almost at normal incidence. On the other hand, if the area of deposition is large, it is likely that the angle of incidence of molybdenum along the edges is no longer at normal incidence. Tilt cones and sidewall coverage may result at the edges if the deposition angle is other than 0°. To find out the answer, the shadow mask can be put in different regions other than along the same axis as the center of the evaporant source. In that case, we can clarify whether straight cones or tilt cones would be formed if the deposition angle is other than 0°. SIMBAD simulation can be used to help find out the answer by setting the deposition angle at different values.

Finally, for the SIMBAD simulations, it was mentioned that the growth factors sticking coefficient and surface diffusion are dependent on the materials, process parameters and the system used. To get more accurate simulation results, calibrations on the sticking coefficient and the surface diffusion length should be done by a comparison of surface profiles and columnar grain sizes between real and simulated films.

Appendix A: Technical drawing of the custom-designed substrate holder.
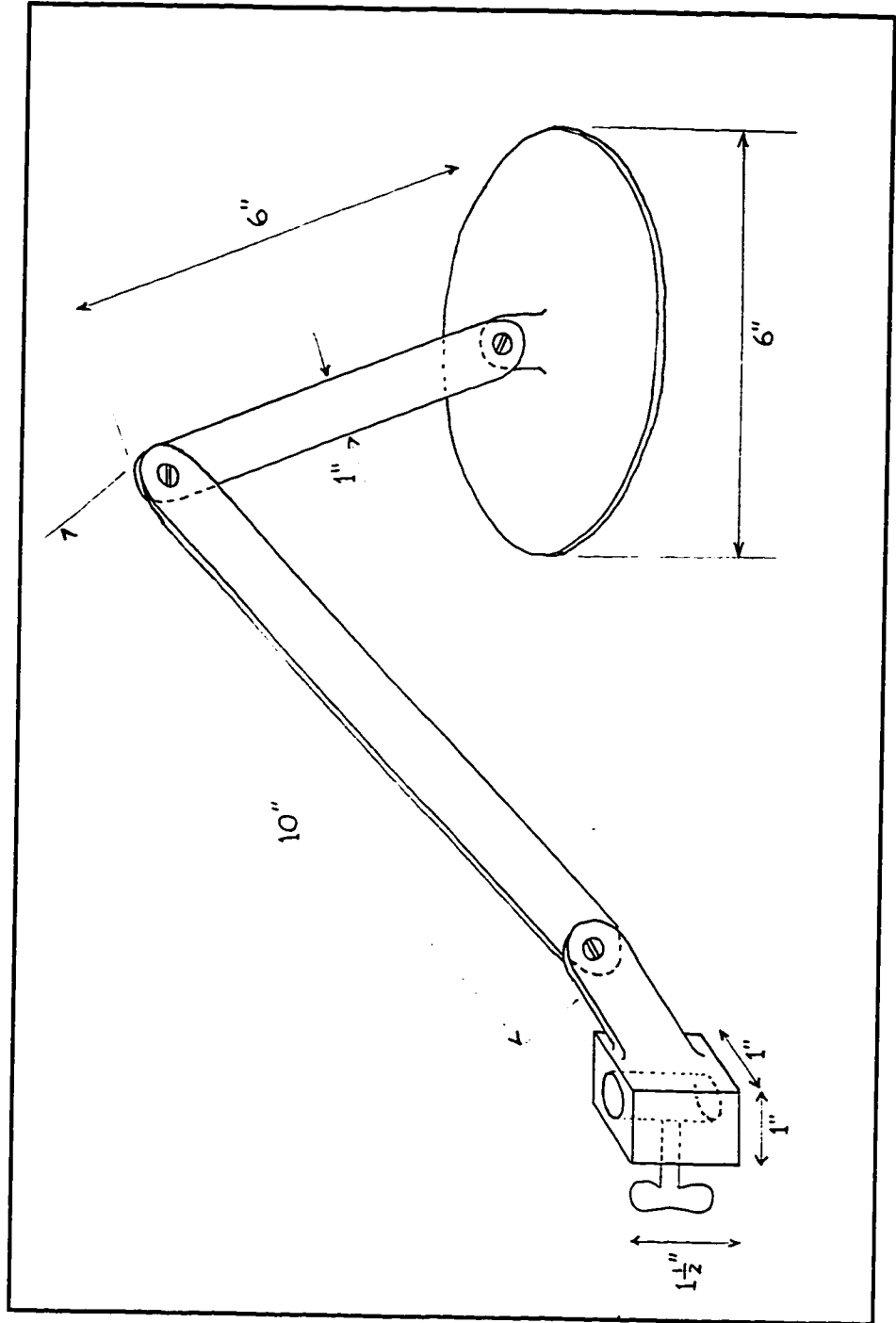
Appendix B: Operation parameters and deposition results for each deposition

Dep. no.	Start pressure (E-6 torr)	Operate pressure (E-6 torr)	Operate power (kw)	Deposition Thickness (A)	Deposit-ion time (min)	Deposition rate(A/s)	Remark
1	1.2	0.56	4	9500 ± 98	4.3	36.6 ± 0.4	Beautiful and high Mo lump source on the cone.
2	3.1	1.2	4	8921 ± 217	2.6	57.2 ± 1.4	Beautiful and high Mo lump source on the cone.
3	3.3	0.65	3.8	8873 ± 70	5.2	28.4 ± 0.2	Beautiful and high Mo lump source on the cone.
4	5.2	3.3	3.8	4662 ± 131	4	19.4 ± 0.6	Beautiful and high Mo lump source on the cone.
5	3.6	2	4	4526 ± 109	3	25.2 ± 0.6	Beautiful and high Mo lump source on the cone.
6	12	8	4	1928 ± 76	3	10.7 ± 0.4	Some Mo inserts added. They didn't wet well. Irregular surface. Much outgasing.
7	24	14	4	4506 ± 19	4	18.8 ± 0.1	No new Mo added after inserts were added from the previous deposition.
8	22	40	4	227 ± 10	4	0.95 ± 0.0	A dent was formed at the center of source. Surface was very uneven.
9	40	51	3.8	1623 ± 60	3	9.0 ± 0.3	More Mo inserts are added to the dent hole
10	53	41	4	4339 ± 21	14.3	5.1 ± 0.0	A dent at the centre,3 different areas were hit to prevent hitting on the dent
11	11	320	4	2843 ± 84	2	23.7 ± 0.7	A big Mo pellet (6X12mm) was melted. Melting is inefficient. Too much outgasing.
12	26	22	3.5	2500 ± 13	30	1.4 ± 0.0	No new Mo after the 2 big Mo pellets were melted from previous deposition.
13	25	24	4	1440 ± 23	3	8.0 ± 0.1	2 another big Mo pellets were melted. Irregular surface. Much outgasing.
14	14	14	3.5	1309 ± 12	4	5.5 ± 0.1	No new Mo after the 2 big Mo pellets were melted from previous deposition.
15	30	40	3.8	7452 ± 56	30	4.1 ± 0.0	4 quarterly cut (1/4) Mo pellets melted. However it was not enough for 30 mins deposition. Too much outgasing.
16	7	15	4	4424 ± 101	15	4.9 ± 0.1	4 more 1/4 Mo melted, but still not enough for 15 mins deposition. Irregular surface
17	5.5	30	4	6256 ± 131	15	7.0 ± 0.1	4 more 1/4 Mo pellets were added. Irregular surface.
18	3.3	5.6	3.8	6750 ± 92	5	22.5 ± 0.3	6 small (6x6mm) Mo pellets were melted. Melting was very efficient. Very beautiful and high lump source was formed at the center. Pressure kept dropping when current went up to 0.25A, and then it stayed there very stable.
19	12	30	3.8	3106 ± 98	3	17.3 ± 0.6	No new Mo added after the 6 small Mo pellets melted from the previous deposition. The lump source was still very beautiful.
20	4	4	3.8	10578 ± 125	8	22.0 ± 0.3	4 small pellets were melted. A nice and high lump was formed.
21	20	43	4.2	4952 ± 52	10	8.3 ± 0.1	No new Mo were added after the 4 small pellets. Unable to move the beam to center. Sweep control was on during deposition to even out the heat. The hit region was flattened by the sweeping.
22	13	50	4.2	2102 ± 35	20	1.8 ± 0.0	No new Mo was added. The hit region was flat.

Appendix C: Description of SIMBAD film growth parameters [28]

user_dist ('T' or 'F') If this parameter is set to true, a user-defined angular distribution is read from the file specified by **angle_file**. If it is set to false, then a compressed cosine angular distribution is used based on the parameters **dep_angle** and **dep_spread**.
Default: F

dep_angle (real) This parameter sets the angle about which the default or user specified angular distributions are centered. Zero angle corresponds to straight down.
Default: 0.0°

dep_spread (real) If no user-defined angular distribution is used, then this parameter is used to determine the angular deposition. If the mode is (S)puttering, a compressed cosine is used and this parameter sets the width of the compressed cosine. If the mode is (E)vaporation, a uniform distribution with a width of **dep_spread** is used.
Default:45.0°

ion_angle (real) (NAI3D) This parameter sets the angle about which the ion flux angular distribution is centered. Zero angle corresponds to straight down.
Default: 0.0°

ion_spread (real) (NAI3D) The angular distribution of the ion flux is given by a uniform distribution of width specified by the **ion_spread**.
Default: 1.0 degree

redeposition ('T' or 'F') (NAI3D) If set to true, this allows for the redeposition of resputtered material elsewhere on the film. It should generally be set to true.
Default: T

angle_file (string) The name of the file from which to obtain a user-defined angular distribution for the incoming sputter flux.
Default: ""

alt_angle_file (string) (NAI3D) The name of the file from which to obtain a user-defined distribution for the incoming sputter flux for alternative particles in alloy sputtering. If the parameter is an empty string then alt_root_name.ang is used.
Default: ""

mean_free_path (real) (NAI3D) Mean free path between gas phase collisions. If set to zero, gas phase collisions are disallowed. Specify distances in microns.
Default: 0.0 microns

Growth Parameters:

thickness (real) Sets the thickness of the film to be added. If negative, etching is assumed. If set to zero, the thickness to the top/bottom is used. The value should be input in microns.
Default: 0.0 microns

diff_length (real) A fundamental parameter related to the diffusion length of the adatoms. It depends, although not simply, on T/T_m of the material being deposited. Which of the two SIMBAD modes used (low or high temperature) will depend on this parameter. Fundamental limitations of the SIMBAD diffusion algorithm limit the minimum diffusion length to the equivalent of about 2 SIM-BAD disc diameters or three simulation units (the exact length of which will depend on the simulation **resolution**). Attempts to enter values below this will result in this minimum value being used. The **diff_length** value actually interpreted by SIMBAD will always be printed out in the run status log. The units of **diff_length** should be in microns. If a negative value is entered, however, the magnitude shall be interpreted as the diffusion length in simulation units.
Default: 3 units

sub_diff_length (real) Sets the diffusion length of an adatom on the substrate. The value should be input in microns. If a negative value is input, however, its magnitude shall be multiplied by the **diff_length** parameter to determine the actual **sub_diff_length** value.
Default: value of **diff_length**

gb_surface_E (real) (NAI3D) Interfacial energy density of a grain boundary relative to the free surface energy (0..1). A higher value leads to greater grain boundary grooving.
Default: 0.25

film_sticking (real) (NAI3D) .
alt_film_sticking (real) (NAI3D) ,

Appendix D: Tutorial of the SIMBAD simulation

In order to run SIMBAD, it is necessary to create parameter files, geometry description files (the substrate topography) and user-defined distribution files (e.g. the sputter target erosion profile.

(1) The XSIMBAD application window XSimbad is opened which is looked like the one that shown in Figure D.1. There are two menu possibilities. The **File** menu contains options for viewing and printing the resultant film output files. The **Simulate** menu contains options for doing film, density and sputtering simulations.

(2) In the beginning of simulation, the **Simulate** menu is chosen. This will pop up a **Select Simulation Name** window into which a root name of the simulation is input. Then the <return> key or **New** button is clicked to bring up to the **film Simulation** window. The **Film Simulate window** is shown in Figure D.2.

(3) In the **Film Simulation** window, the substrate topography file (i.e. root_name.init file) is created by entering the width and height (in microns) of the simulation region into the two text window labeled **Size**. The **Edit** Substrate button is then clicked. A substrate drawing window will then be seen which is shown in Figure D.3.

(4) Different shape of the topography can then be drawn in the drawing window, depending on the height of the substrate, diameter of the gate, shape and angle of undercut of the cavity. The root_name.init file will be created by clicking the **Save** button.

(5) After the root_name.init file is created. The **quit** button is clicked to return to the **Film Simulation** window.

(6) In the **Film Simulation** window, **Edit Parameters** button is clicked to bring up to

the **Edit Simulation Parameters** window which is look like the one that shown in

Figure D.4. There is a big parameter list in which many parameters are contained.

Parameters that need to be edited is inserted into the root_run file by double clicking

on the parameter name and then clicking on the >> button. In this thesis, they include

the *edited default parameter: deposition **Mode** which is defaulted as Evaporation

(E), **Ang_spread** and **Dep_angle** which are defaulted as 0° for evaporation,

Thickness of the thin film to be deposited which is defaulted as

(1.8 µm); and the variables of the key growing parameter which include:

diffusion_length, fiilm_sticking coefficient. Different values can be input for the

variables for each simulation. The root_name.run file can then be generated by

clicking on the **Save** button. This will be returned to **the Film Simulation** window.

(7) In the **Film Simulation window**, the **begin** button will be clicked to start the

simulation. Simulation window during the simulation progress is shown in

Figure D.5

(8) To view the resultant film output, the **File** menu bar in the XSImbad window (which

was shown in Figure D.1) is clicked. Afterwards, the **view graph** option is selected.

the resultant film will be displayed when a root_name.film file name is selected.

(9) In a manner very similar to that for viewing a graph, plots of certain files can be

printed on a PostScript printer using the **Print Graph** option of the **File** menu.

* Remark: There is no need to run the SIMSPUD simulation to find the angular

distribution of the sputter flux. It is because the simulation mode used in this thesis is

evaporation. For evaporation, as the source was far away from and directly above the

wafer, The distribution is uniform so that the angular spread (ang_spread) and the average

angle of deposition (Dep_ang) is equal to zero. Since there is no user_defined angular

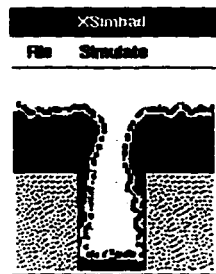distribution file required, The user_dist parameter should be defaulted to False (F).
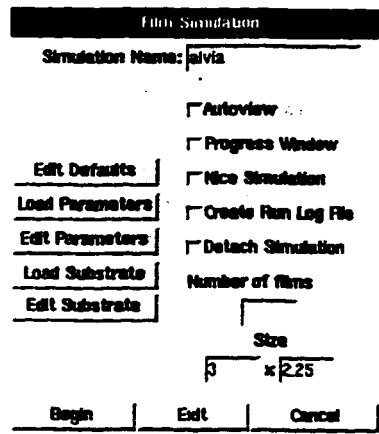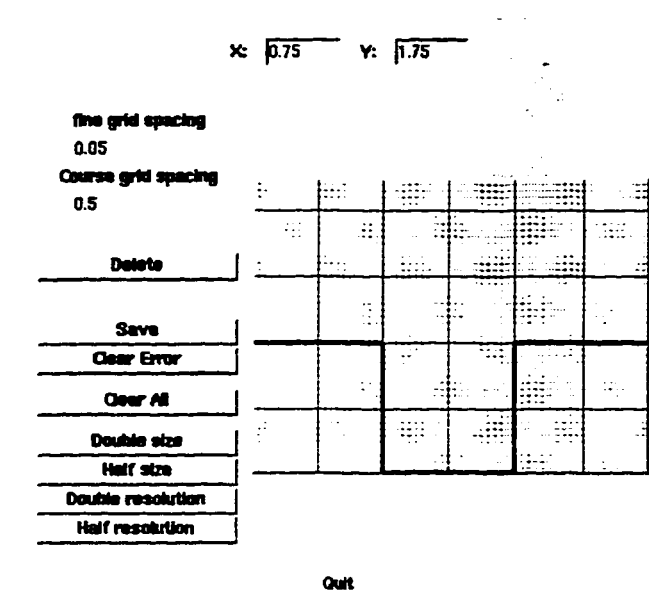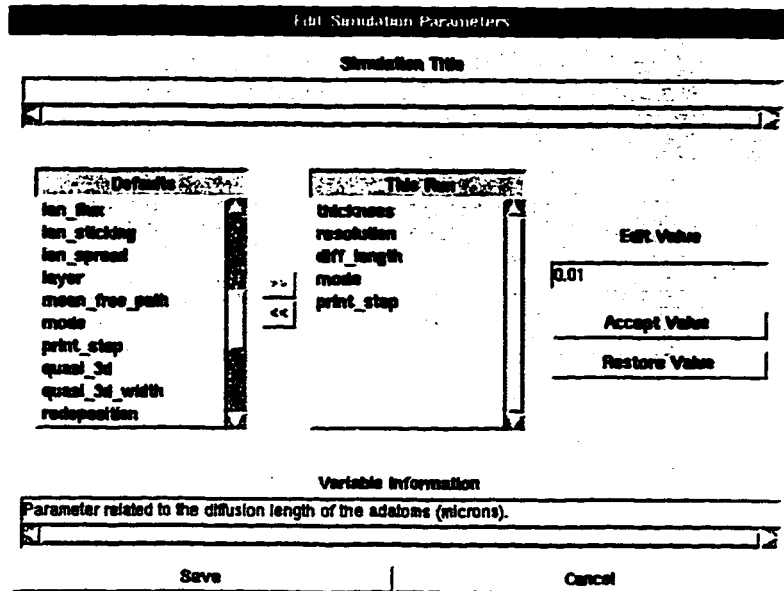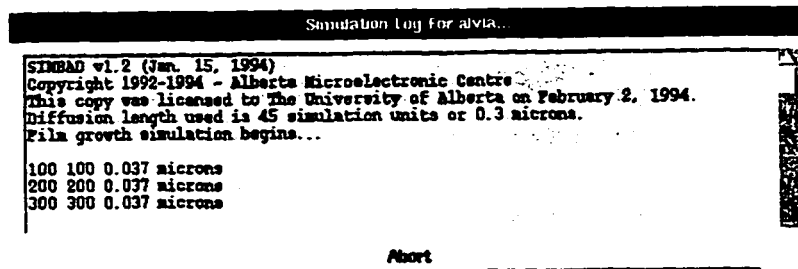

Figure D.1

Figure D.2

Figure D.3

Figure D.4

Figure D.5

117

Appendix E: Major Problems encountered from the electron beam evaporator.

The biggest problems that were encountered from this experiment are due to the instability of the E-beam system. It was very time consuming to fix these problems. Especially this machine is an old model, there is hardly anyone that still knows how to fix the system. Problems that were encountered are described as below:

1. Problem: Arcing was found between the transformer and a wire running along side. Arc was only generated once the HV supply of the electron gun was activated.

   Solution: The problem was fixed by replacing the wire with a new one.

2. Problem: There was no deposition rate reading shown on the rate monitor.

   Solution: The Crystal sensor was broken. A new sensor was replaced.

3. Problem: There was no filament current for Gun B.

   Attempts: a) The emitter assembly was taken out to check if there was any short circuit.

   b) The whole emitter assembly was taken out for cleaning using a piece of 320 grit paper.

   c) The supersource assembly was tested using voltmeter, there was no short/open circuit found.

   d) The emitter assembly A was switched with assembly B (we have 2 guns in our E-beam evaporator) to verify if the problem came from the emitter assembly or not. It was found that there was still no filament current for gun B, whereas gun A was still working fine. It was confirmed that the filament current problem was not caused by the emitter assembly.

   Cause: Eventually, it was found that communication relay was dirty which caused intermittent problem. Occasionally, there was communication problem that the signal was unable to reach the power supply.

Solution: A new communication relay was replaced.

4. Problem: The electron beam position was shifted <u>laterally</u> to the right edge of the crucible pocket for gun A.

Attempts: a) The focus current was adjusted by turning the beam sweep control. However, the focus current shut off itself automatically.

b) The pole pieces were checked but there was no damage.

c) The oxidized ceramic beads were replaced but it still did not work.

Cause: The margin setting of the focus current was shifted. It wrongly interpreted that the edge as the center.

Solution: The high voltage setting was adjusted to modify the deflection coil current (i.e. focus current)

5. Problem: The high voltage dropped and then shut off itself automatically after two to five minutes during deposition.

Cause: When the electron beam was just formed, the deflection beam was not stable and not uniform yet. When the protection shutter was opened, it might hit the scattered E-beam and short the power.

Solution: The shutter was kept closed for at least 30 mins before opening, to make sure the E-beam became stable and deflected in a right path.

6. Problem: The high voltage dropped and then shut off itself after deposition for 20 seconds.

Cause: The ceramic spacing insulator in the emitter assembly was cracked. Therefore, some gases trapped inside and when the voltage was turned on, the gas expanded which would short the power.

Solution: The broken ceramic spacing insulator was replaced.

7. Problem: The electron beam was drifted.

Cause: The emitter assembly was a little bit tilted from the housing assembly.

Solution: The emitter assembly was reinstalled and put back in position.

8. Problem: The high voltage dropped suddenly during deposition.

   Cause: Unknown cause. It may be due to intermittent problem from the power supply

   Attempt: By lowering the beam current, the high voltage was able to recovered and back up to the operating voltage temporarily. Then the beam current can be increased again. However, same problem happened again every two to three minutes.

9. Problem: The electron beam slowly drifted to the right and was unable to focus back to the center.

   Attempt: The temporarily solution was to put a magnetic pole piece at the left to pull the beam back towards the left side. However, after another deposition, it shifted to the right again. Another attempt was to change the voltage to order to remodify the focus current. It was found that the beam moved even further to the right when the voltage was decreased. In order to move the beam to the left, the high voltage must be increased. However, it turned out that even the voltage was increased to maximum, it was still not high enough to enable the beam to move back to the center.

10. Problem: Roughing pump was malfunction

    Cause: Due to backstreaming of oil.

    Solution: Another roughing pump was replaced.

       Remark: The new roughing pump created a lot of problem. The replaced one was very ineffective because it was much smaller than the previous one. It took around half an hour to go to the crossover pressure which was 50 mtorr. The one that we used before only took one minute.

       Actually, several problems were created due to this inefficient pump. e.g. (1) Deposition rate decreased due to the hydrostatic pressure effect. (2) During regeneration of the cryopump, the roughing pump was not powerful enough to pump out the trapped gas from the cryopump, which decrease the efficiency of the cryopump. (3) To obtain a nicely lump source, Mo pellets must be added to the Mo cone source very frequently. A lot of outgas would

be produced during melting due to the adsorption of water and other contaminants which released upon heating. However, the cryopump was not efficient enough to pump them out promptly. Residual gas pressure increased a lot after melting. Due to the inefficiency of the vacuum pumping, there were still much outgas trapped inside the melted evaporant source which caused spitting from the evaporant and localized exploding from the gun during deposition. The supplied power had to be controlled and limited to prevent the spitting, which in turned influence the deposition rate.

11. Problem: The cryopump reached its full capacity. It needed to be regenerated. Some Frost was observed to form upon the cyropump surface. Moreover, the gas pressure stayed at the cross-over pressure (It is defined as the pressure in the vacuum chamber at which the "cross-over" from rough-pumping to high-vacuum-pumping that chamber with the cyropump takes place.) and was incapable of maintaining a high vacuum even the cold head and the compressor units were operating satisfactorily. It is an indication that the gases being condensed and adsorbed upon cold surfaces are too thick that the cryopump must be regenerated.

Solution: The cyropump must be regenerated. Regeneration of the cyropump is a solution to put it back to the normal operation. It is a process by which all previously pumped gases are removed from the cryopump and the cryopump is left in a condition ready to again accept its full-rated capacity. The cold internal parts of the cryopump must be warmed to room temperature and the liberated gases removed. This can be done by closing the high vacuum valve, and shutting off the cold head and compressor unit. Depending upon the quantity of frozen gases contained within the cryopump, it can take two to four hours to bring the cryopump to room temperature. After the condensed and adsorbed gases have been warmed up, the high vacuum valve from the cryopump and the roughing valve from the roughing pump will be opened in parallel to allow the expanded gas to suck out from the system. This usually takes around four hours. Finally, the cryopump can be turned on for overnight until it is cooled down. It is then ready to operate again.

12. Problem: The bell jar was unable to be closed completely. A gap of around ½" is found.

Cause: The position sensor was loosen out.

Solution: A screw was thread out. The sensor was tighten up by replacing a screw.

References

[1] K. Derbyshire, "Beyond AMLCDs: Field emission displays?," *Solid State Technology*, 55 (Nov.1994).

[2] C.A. Spindt, C.E. Holland, I. Brodie, I. B. Moonley and E.R. Westerberg, "Field-emitter arrays applied to vacuum fluorescent display," *IEEE Trans. on Electron Devices*, 36 (1), 225 (1989).

[3] K. Koga, K. Morimoto and Y. Hori, "New structure Si field emitter arrays with low operation voltage," *IEDM*, 24 (1994).

[4] D. Peters, I. Paulus and D. Stephani, "Oxidized amorphous silicon as gate insulator for silicon tips," *Journal of Vacuum Science and Technology*, 12 (2), 653 (1994).

[5] G. Laburine and R. Meyer, "Novel type of emission flat panel display: the matrixed cold cathode microtip fluorescent display," *Displays*, 38 (Jan. 1987).

[6] C.B. Richardson and F. Davanloo, "Amorphous diamond material produced by laser plasma deposition," United State Patent, 509873 (1992).

[7] B.C. Djubua and N.N Chubun, "Emission properties of Spindt-type cold cathodes with different emission cone material," *IEEE Trans. on Electron Devices*, 38 (10), 2314 (1994).

[8] C.A. Spindt, I. Brodie, L. Hump and E.R. Westerberg, "Physical properties of thin-film field emission cathodes with molybdenum cones," *Journal of Applied Physics*, 47 (12), 5248 (1976).

[9] S. Itoh, T. Watanabe, K. Ohtsu, M. Yokoyama and M. Taniguchi, "Investigation of Cathodoluminescent Display Device with Field Emission Cathodes," *Japanese Journal of Applied Physics*, 32 (9A), 3956 (1993).

[10] Spindt, et al., "Field emission cathode structures and devices utilizing such structures," United State Patent, 3,755,704, (1973).

[11] J.A. Greer and F.P. Guy, "Stress in molybdenum films used for FEA display technology," *Materials Research Society Symposium Proceedings*, 345, 323 (1994).

[12] C.A. Spindt and C.E. Holland, "The Spindt field emission cathode," *SRI International*, 2RI (1986).

[13] C.A. Spindt, C.E. Holland, A. Rosengreen and I. Brodie, "Field-emitter arrays for vacuum microelectronics," *IEEE Trans. on Electron Devices*, 38 (10), 2355 (1991).

[14] J.M. Macauley, I. Brodie, C.A. Spindt and C.E. Holland, "Cesiated thin field emission microcathode arrays," *Applied Physics Letters*, 61 (8), 997 (1992).

[15] W.D. Goodhue, P.M. Nitishin, C.T. Harris, C.O. Bozler, D.D. Rathanum, G.D. Hohnson and M.A. Hollis, "Bright field analysis of field emission cones using high resolution properties in current stability," *Journal of Vacuum Science and Technology B*, 12 (2), 693(1994).

[16] L.H. Robert, W. A. Mackie and P.P. Davis, "Use of boundary element methods in field emission computations," *Journal of Vacuum Science and Technology B* , 12 (2), 754 (1993).

[17] Material Characterization, vol. 10, 9th edition, American Society for Metals Handbook, Metals Park, OH, 1986, p.587.

[18] Utsumi Takao," Keynote address vacuum microelectronics: What's new and exciting," *IEEE Trans. on Electron Devices*, 38 (2), 2276 (1991).

[19] S.K. Dew and T.J. Smy, SIMBAD V1.4 User's Manual, Alberta Microelectronics Center, Edmonton, Canada, 1996.

[20] L.I. Maissel and R. Glang, Handbook of Thin Film Technology, McGraw-Hill, New York, 1970, Ch.1 - Ch. 3.

[21] M. Ohing, The Material Science of Thin Film, Academic Press, New York, 1991, Ch. 2 - Ch. 6.

[22] R.F. Bunshah, Handbook of Deposition Technologies for films and coatings, Noyes, New Jersey, 1993, Ch. 13.

[23] Airco Temescal, Instruction Manual for Four-Hearth Electron Beam SuperSource, Airco Inc, California, 1980.

[24] J.R. Bosnell and U.C. Voisey, "The effect of deposition parameters on the structure and resistivity of molybdenum films", *Thin Solid Films*, 6 (2), 107 (1970).

[25] R.N. Tait, "Thin film microstructure effects in VLSI metallization,", PhD. thesis, University of Alberta, Edmonton, Canada, 1992.

[26] M. Lam, "Studies of hot aluminum sputter deposition for microelectronics processing," M. Sc. thesis, University of Alberta, Edmonton, Canada, 1994.

[27] T. Janacek, "A study of collimated sputtering for VLSI metallization", M. Eng. thesis, Carleton University, Ottawa, Canada, 1994.